Elucidating the emergence of heterogeneous motion in living matter from the micro- to the nanoscale

---

Von der Universität Bayreuth
zur Erlangung des Grades eines
Doktors der Naturwissenschaften (Dr. rer. nat.)
genehmigte Abhandlung

---

von
Adal Zacharias Sabri
aus Greiz

1. Gutachter: Prof. Dr. Matthias Weiss
2. Gutachter: Prof. Dr. Jürgen Köhler

Tag der Einreichung: 05. November 2020
Tag des Kolloquiums: 18. März 2021

Elucidating the emergence of heterogeneous motion in living matter from the micro- to the nanoscale

---

Von der Universität Bayreuth
zur Erlangung des Grades eines
Doktors der Naturwissenschaften (Dr. rer. nat.)
genehmigte Abhandlung

---

von
Adal Zacharias Sabri
aus Greiz

1. Gutachter: Prof. Dr. Matthias Weiss
2. Gutachter: Prof. Dr. Jürgen Köhler

Tag der Einreichung: 05. November 2020
Tag des Kolloquiums: 18. März 2021

Zusammenfassung

In dieser Arbeit wurde das Aufkommen von Heterogenitäten während der anomalen Diffusion zweier biologischer Systeme auf unterschiedlichen Längenskalen mit Hilfe von *Single-Particle-Tracking* und statistischer Bewegungsanalyse untersucht.
Im ersten Teil dieser Arbeit wurde die Subdiffusion von im Zytoplasma menschlicher Krebszellen befindlicher Quantenpunkten, welche mithilfe der *Bead-Loading*-Technik internalisiert wurden, unter diversen Konditionen beobachtet. Zu diesem Zweck wurde zunächst die Bewegung der Nanopartikel in unbehandelten Zellen untersucht. Um mehr über mögliche Wechselwirkunspartner in der Zelle zu erfahren, wurde die Integrität großer Strukturen in der Zelle, wie Bestandteile des Zellskeletts oder das endoplasmatische Retikulum, gestört und auch in diesen Proben die Bewegung der Quantenpunkte untersucht. Zur Quantifizierung der Bewegungsmuster dienten etablierte Größen, wie die mittlere quadratische Verschiebung und, daraus resultierend, die Diffusionsanomalien und generalisierte Transportkoeffizienten, sowie die Autokorrelationsfunktion der Geschwindigkeiten. Um den Ursprung der aufkommenden Heterogenitäten in der diffusiven Bewegung der Quantenpunkte in der Zelle detaillierter ergründen zu können, wurden weitere, neue Maße etabliert. Experimentelle Resultate aller untersuchter Konditionen zeigten eine starke, vom Zustand der Mikrotubuli abhängige Subdiffusion mit antipersistenten Inkrementen und erheblichen Heterogenitäten in den Einzeltrajektorien. Dieses bestimmte Bewegungsmuster wurde auf transiente Wechselwirkungen der Nanopartikel mit dem endoplasmatischen Retikulum (ER) zurückgeführt, welches an sich noch Fluktuationen durch die Dynamik des Zytoskeletts erfährt. Es wurde die Hypothese aufgestellt, dass die Partikel stochastisch zwischen unterschiedlichen Mobilitätszuständen wechseln. Aufgrunddessen wurde ein Modell, welches fraktale Brownsche Bewegung und den stochastischen Wechsel zwischen Zuständen niedriger und erhöhter Mobilität beinhaltet, erstellt und die daraus gewonnenen Simulationsdaten wurden mit dem Experiment verglichen. Es wurde gezeigt, dass das entwickelte Modell die experimentellen Beobachtungen vollständig beschreiben kann, ohne dass auf eine Verteilung von Diffusivitäten zurück gegriffen werden muss. Die Übereinstimmung der experimentellen mit den simulierten Daten ließ die Schlussfolgerung zu, dass die Bewegung von Nanopartikeln im Zytoplasma maßgeblich von der Integrität des ERs und des Mikrotubuli-Netzwerkes beeinflusst wird und nicht nur durch Diffusion in gedrängter Umgebung bestimmt ist.
In einem zweiten Projekt wurden die Auswirkungen von Störungen der Genregulation auf die Zytoskeletthülle von Blutstromparasiten untersucht. Unter Zuhilfenahme der *small-interfering-RNA*-Methode wurden zwei Unterpopulationen mit gestörter Genregulation generiert und deren Bewegung analysiert. Es wurde beobachtet, dass die Depletion gewisser Proteine die Bewegung und Beweglichkeit der Parasiten stark beeinflusst. Dies ließ Rückschlüsse auf etwaige Veränderungen des Zellskeletts oder des Flagellums zu.

Abstract

The emergence of spatiotemporal heterogeneity during anomalous diffusive motion of two distinct biological systems is studied with the aid of single particle tracking (SPT) and statistical motion analysis on different length scales ranging from nanometers to a few 100 micrometers.

In the first part of this thesis, the subdiffusion of quantum dots nanoparticles loaded into the cytoplasm of living mammalian cells was observed under varying conditions. In particular, the particles' motion was quantified in untreated cells and cells where the integrity of ubiquitous organelles, like the cytoskeleton or the endoplasmic reticulum (ER), was perturbed. For analysis, established estimators, like the mean squared displacement, resulting anomaly exponents and generalized transport coefficients, the velocity autocorrelation function, and newly proposed estimators were used. The latter include the statistics of normalized increments, the local convex hull and the autocorrelation function of fluctuations in squared increments. It was found that all experimental conditions show strong, microtubule-dependent subdiffusion with antipersistent increments and a substantial heterogeneity, albeit to a varying degree. These heterogeneities were hypothesized to come from transient interactions of tracers with the cytoskeleton-shaken endoplasmic reticulum network. An intermittent fractional Brownian motion model with stochastic switching between different mobility states was derived, that was found to be in excellent agreement with the experimental data without the need of diffusing diffusivities, thus providing strong evidence for the validity of the hypothesis.

In the second part, perturbations of the posttranslational protein regulation of tubulin, presumably regarding the structure of the cytoskeletal cortex, and their influence on the active, self-propelled motion of individual kinetoplastids of the genus *Tryponosoma Brucei* was studied. To this end, two distinct mutant subpopulations were generated using small interfering RNA methods and their respective motion behavior was quantified with SPT methods and a motility assay. Non-induced individuals of either condition did not show significant deviations from the parental strain. However, upon depletion of certain proteins, significant changes in the motion were observed, which were traced back to possible variations in cell stiffness and/or presumably structural abnormalities.

Contents

Introduction

'Our nature consists in motion;
complete rest is death.'

(Blaise Pascal)

The essence of motion on a multitude of time and length scales, from the transport of small pollen granules suspended in a simple solvent fueled by thermal fluctuations [1], through eye movements [2] and active animal migration [3], up to stellar dynamics [4, 5], is a ubiquitous topic of research in many fields of physics and the life sciences. In living organisms, motion plays a particularly important role, since it is one of the main features of life, next to reproduction, metabolism, growth and stimulus response. In other words: If nothing moves, nothing progresses; and in the life sciences, the absence of motion is on par with death. With this in mind, exploring the underlying concepts of motion in living matter seems to be a promising way to gain more insight into the inherent nature of life.

One of the most prominent types of motion is, without any doubt, the random walk of suspended particles firstly described by Robert Brown in 1828 [1]. This erratic movement, later dubbed 'Brownian motion' in his honor, is one of the pillars of biological and soft condensed matter physics [6]. At the start of the 20^{th} century, Einstein and Smoluchowski did pioneering work on the fundamentals of random displacements of single particles, when they employed ideas formally linked to central limit theorem and suggested a Gaussian probability distribution for steps sizes with a mean squared displacement (MSD) that increases linearly in time [7, 8]. When comparing this process to Fick's second law [9], striking similarities can be noticed, which enable the description of Brownian motion as 'normal diffusion'. This constitutes the basis of numerous applications ranging from polymeric solutions to biological systems [6].

Beginning with the most fundamental level in a biological context, single cells have to be regarded as living entities, since they meet all individual criteria of life. On a sub-micron scale, cells are kept alive by a plethora of biochemical processes including energy transduction, synthesis of macromolecules, or simple material uptake, conversion and disassembly, all of which require some sort of intracellular transport mechanism. This transport mechanism can either be active, i.e. carried out by molecular motors [10], or – on a more fundamental level – passively fueled by stochastic motion, i.e. diffusion. However, in recent years, modern microscopy techniques have uncovered significant deviations from the laws of Brownian motion, when observing stochastic transport inside the cell [11–15].

The emergence of transport behavior which cannot be explained with normal diffusion may seem exotic. However, a linear temporal scaling of the MSD is generally the exception

rather than the norm in a plethora of processes, recapped as 'anomalous diffusion', when observing more complex environments in theory [12, 16–21] and experiment [6, 13, 22–27]. Anomalous diffusion can be separated into two distinct classes: Subdiffusive motion, where tracers' MSD grows less than linearly in time, and the superdiffusive regime, which is usually more prominent when observing active processes. Causes of the emergence of heterogeneous anomalous transport behavior can be numerous. Most subdiffusive random walk processes have some kind of inherent heterogeneity, which can be induced by environmental effects like caging [22], crowding [11, 15, 28, 29], or unspecific binding [30]. Heterogeneity in the trajectories of active walkers undergoing superdiffusive motion on the other hand might also occur due to changes in motility, induced by specific modifications of their properties [31, 32].

Capturing the motion of tracers on a (sub)cellular level requires advanced experimental techniques. The most direct of these methods is the observation of individual tracers and subsequent extraction of their respective time series trajectory in a process called single particle tracking (SPT). In particular, this technique provides the entire trajectory, which allows one to evaluate different observables for the quantification of the systems dynamic. The distinct features extracted from the acquired data in turn provide the opportunity to draw conclusions on the underlying mechanism of motion as well as possible hints towards causes of perturbation and heterogeneity.

The causes of the occurrence of specific anomalous motion behaviors and the resulting implications on the state of the environment and properties of the observed tracer will be elucidated on with the help of two biological model systems in this thesis. To this end, single particle tracking methods are used to quantify motion behavior of:

(i) semiconductor nanoparticles – so-called quantum dots – in the cytoplasm of living mammalian cells at varying conditions to elucidate the emergence of anomalous diffusion and spatiotemporal heterogeneity in an active environment driven by fluctuations, and

(ii) parasitic kinetoplastid mutants with varying protein regulation properties to find cues to the importance of perturbations of their (cytoskeletal) structure on heterogeneities in the resulting dynamics of individuals.

The first model system focuses on the subdiffusion of non-self propelling, passive particles in an actively driven, highly disordered and fluctuating environment, thus probing external influences on the motion behavior of inert tracers. As of yet, the anomalous nature of diffusion in the cytoplasm is generally agreed on [6, 11, 13, 20, 33, 34], however no compelling model has been derived yet, to reliable describe the phenomenon in its entirety. In fact, it is neither clear which mechanism regulates the anomaly of cytoplasmic diffusion itself, nor how one should picture the emergence of heterogeneity in motion in an active environment. Here, a quantitative SPT analysis was employed to gain insight in potential sources

of heterogeneity of cytoplasmic subdiffusion and possible intracellular interaction partners to inert particles loaded to cells. Furthermore, the role of ubiquitous cellular organelles, such as the cytoskeleton and the endoplasmic reticulum, on the diffusion of tracers was studied in detail and an intermittent (fractional) Brownian motion model was derived that is capable of describing the experimentally observed features. Moreover, simulations based on the derived theoretical model were done, which reproduce the experimental observations.

In contrast to the subdiffusion in the cytoplasm, which takes place in the sub-micron regime, single particle tracking of parasitic kinetoplastids has to be done on a length scale of some $10 - 100\,\mu m$. These model organism are active walkers, i.e. self-propelled, and show a predominate superdiffusive behavior with persistent motion intercepted by occasional tumble phases. In this work, the small interfering RNA (siRNA) technique was used to interfere with protein regulation and presumably modify the cytoskeletal structure of parasite's subpopulations. The motion patterns of perturbed individuals were quantified using a motility analysis based on single trajectories. Eventually, conclusions on induced heterogeneities of dynamics were drawn, which presumably highlight the necessity of certain proteins for the correct formation of the parasites cytoskeletal structure and in turn influence their motility.

Both projects were done with the aid of SPT and subsequent statistical motion analysis techniques, highlighting the capability of the experimental and evaluation approach to quantify various and divers types of motion on multiple time and length scales and thus capturing the essence of one criteria of life.

Beginning with the **fundamentals**, chapter 1 introduces the theoretical framework of Brownian motion and normal diffusion. Expanding on these concepts, anomalous diffusion is introduced and different models for sub- and superdiffusion are presented. Furthermore, the fundamentals of the biological specimen used in the course of this thesis – namely, eukaryotic cells and the kinetoplastid *Trypanosoma brucei* – are presented. Concluding the theoretical background, a brief outline on microscopy is given and the fundamentals of fluorescence are explained.

In chapter 2, the **methods and materials** employed in the **experiments** implemented during the course of this thesis are presented. Hence, the biological specimen and their (cell) culture, quantum dot tracers and other fluorescent marker protocols, as well as the microscope settings and setups used in experiments are explained in detail. Thus, an overview of all experimental steps of data acquisition is given.

The methods employed for the **evaluation of the acquired data** are presented in chapter 3. Single particle tracking was used to extract trajectories from space-intensity-time series of tracers on the nano-to-micro meter scale. After the trajectories are extracted from the 2D image time series, the motion behavior of the tracers has to be evaluated.

Beginning with a more basic approach, the time-averaged mean squared displacement (TA-MSD, $\langle \mathrm{MSD}(\tau) \rangle_t$) is calculated, from which the anomaly exponents α and the generalized diffusion coefficients K_α can be derived via a simple power-law fit $\langle \mathrm{MSD}(\tau) \rangle_t \propto K_\alpha \tau^\alpha$. Since time series were acquired with precise temporal resolution, velocities can be assigned to each step and therefore the velocity autocorrelation function (VACF) is a meaningful quantity to look at. To gain more insight into the underlying mechanism of diffusion and potential heterogeneities introduced by either environmental factors or intrinsic tracer properties, more elaborate evaluation methods had to be employed. Naming the most relevant, the statistics of normalized increments $p(\chi)$, the local convex hull (LCH), and the autocorrelation of squared increments $G(\tau)$ are introduced and explained with example trajectories gathered from simulations.

In chapter 4, the **results** of the evaluation process of quantum dots motion observed in human cervical cancer cells under various conditions are presented. First, the diffusion in the cytoplasm of untreated cells is compared to the diffusion in artificial, highly viscous fluids as a control. It was found that quantum dots move in a subdiffusive manner in the cytoplasm which is in good agreement with previous studies [6, 13, 22–27]. However, traces of heterogeneity were found in individual trajectories acquired from untreated cells, when looking at the statistics $p(\chi)$, the LCH, and the autocorrelation of squared increments. Next, the integrity of larger organelles was perturbed to test their influence on the diffusion of presumably inert nanoparticles in the cytoplasm. Drastic changes to the untreated cells were observed, when breaking down microtubules or fragmenting the endoplasmic reticulum, whereas disrupting the actin filaments did not show significant changes in diffusive behavior. On the basis of the results, an intermittent fractional Brownian motion model was derived, which is capable of describing the experimental data well. It is presented, discussed and compared to the experimental findings in chapter 5.

Results from the motility analysis of *T. brucei* are presented in chapter 6. Again, methods established in chapter 3 were used to find distinct variations in the motion pattern of untreated parasites and subpopulations where protein regulation was perturbed. In fact, the overall motility of individuals changed significantly, when inhibiting specific protein modifications. Subsequently, the findings are discussed in chapter 7 and possible implications on the cytoskeletal structure of the parasites are presented.

In summary, single particle tracking methods and subsequent statistical motion analysis was used to find heterogeneities in two distinct biological model systems on different length scales and with varying underlying mechanisms. This shows that motion is not only a key factor of life, but that a general heterogeneous nature seems to be present in various transport processes in biophysics ranging from passive diffusion to active motion.

PART I

Fundamentals

1. Theoretical background

This chapter will give an overview on Brownian motion, diffusion and the origin of anomalous diffusion. Furthermore, the fundamentals of the biological specimen probed during the course of this thesis – namely, eukaryotic cells and the kinetoplastid T. brucei – are presented. In a last section, the employed microscopy techniques are discussed in theory and the concepts of fluorescence are explained.

1.1. Brownian motion & diffusion

In 1828 Robert Brown reported on the movement of suspended granules extracted from larger pollen grains in a fluid medium for the first time [1]. The evident motion of this micron-sized tracer particles usually shows irregular and erratic behavior. Albert Einstein claimed in his 1905 papers that this motion arises from collisions with fast moving molecules within the solution due to the molecular-kinetic theory of heat [7, 35].

In 1908 Paul Langevin derived another concept on Brownian motion using Newton's second law in combination with stochastic forces [36]. The equation of motion of an arbitrary particle with mass m, damping constant $\gamma = \xi/m$ (where ξ is the drag coefficient), and external potential U can be written as:

$$m\frac{\mathrm{d}^2}{\mathrm{dt}^2}\mathbf{x} + \gamma\frac{\mathrm{d}}{\mathrm{dt}}\mathbf{x} = -\nabla U + F'(\mathbf{x},t)\,, \tag{1.1}$$

where $F'(\mathbf{x},t)$ is a strictly δ-correlated thermal noise with Gaussian probability distribution and correlation function:

$$\langle F'_i(\mathbf{x},t)F'_j(\mathbf{x}',t')\rangle = 2\gamma k_\mathrm{B}T\delta_{i,j}(\mathbf{x}-\mathbf{x}')\delta_{i,j}(t-t')\,. \tag{1.2}$$

In an overdamped regime with small Reynolds numbers, inertia can be neglected for experimentally relevant time scales ($|m\frac{\mathrm{d}^2}{\mathrm{dt}^2}\mathbf{x}| << |\gamma\frac{\mathrm{d}}{\mathrm{dt}}\mathbf{x}|$)[1]. Therefore, the overdamped equation can be written as:

$$F_\mathrm{ext} - \gamma\frac{\mathrm{d}}{\mathrm{dt}}\mathbf{x} + F'(\mathbf{x},t) = 0\,,\ \text{with } F_\mathrm{ext} = -\nabla U. \tag{1.3}$$

Integrating Eq.1.3 over all possible implementations of $F'(\mathbf{x},t)$ sequences while assuming the external potential to be $U = 0$ and using the probabilistic description where $p(\mathbf{x},t)$ is the probability density function (PDF), one obtains the overdamped *Fokker–Planck* equation (also called *Smoluchowski* equation):

[1] Typically Reynolds numbers in cellular environment are $\mathrm{Re} = \frac{\rho r v}{\eta} \approx 1\cdot 10^{-6} << 1$, with $v = 1\,\mu\mathrm{m/s}$ & $r = 1\,\mu\mathrm{m}$ in water-like solution.

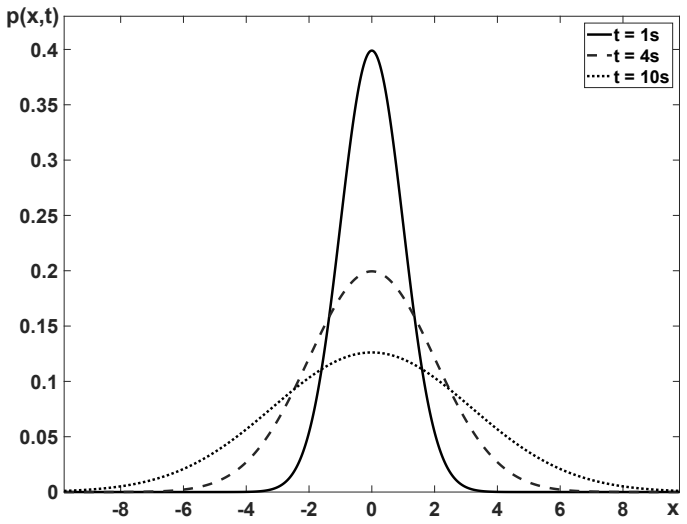

Figure 1.1: Normalized temporal evolution of $p(x,t)$ with mean value $\mu = 0$, and $D = 0.5\,\mathrm{s}^{-1}$ as described by Eq.1.5. Distance x in arbitrary units. Full line: $t = 1\,\mathrm{s}$, dashed line: $t = 4\,\mathrm{s}$, dotted line: $t = 10\,\mathrm{s}$.

$$\frac{\partial}{\partial t}p(\mathbf{x},t) = D\frac{\partial^2}{\partial t^2}p(\mathbf{x},t). \tag{1.4}$$

This relation is equivalent to Fick's second law of diffusion [9]. Hence, the solution to the former given equation Eq.1.4 in one dimension, assuming N particles starting from the origin at time $t = 0$ is given by:

$$p(x,t) = \frac{N}{\sqrt{4\pi D t}}e^{-\frac{x^2}{4Dt}}. \tag{1.5}$$

Here, $p(x,t)$ denotes the probability of finding a certain particle with diffusion coefficient D at time t and distance x from its point of origin. The temporal evolution of $p(x,t)$ is shown in Fig.1.1.

With this propagator (Eq.1.5), the n^{th} moments of the probability distribution can be calculated to be $\int_{-\infty}^{\infty} x^n p(x,t)\mathrm{dx}$. With only even moments being non-zero and the second moment determining all subsequent moments, the variance or mean squared displacement (**MSD**) can be written to be:

$$\int_{-\infty}^{\infty} x^2 p(x,t)\mathrm{dx} = \langle x(t)^2\rangle_E = \langle \mathrm{MSD}(\tau)\rangle_E\,, \tag{1.6}$$

where $x(t)$ denotes particle positions at a given time equivalent to the position denoted in the *Langevin* equation Eq.1.3. The so-called ensemble-averaged mean squared displacement $\langle \mathrm{MSD}(\tau) \rangle_E$ of M realizations of a single particles path and time-averaged MSD $\langle \mathrm{MSD}(\tau) \rangle_t$ of N points in time with distance τ are equal for ergodic systems [37], therefore

$$\langle \mathrm{MSD}(\tau) \rangle_E = \frac{1}{M} \sum_{i=1}^{M} (x_i(\tau) - x_i(0)) = \frac{1}{N} \sum_{i=1}^{N} (x(t_i + \tau) - x(t_i)) = \langle \mathrm{MSD}(\tau) \rangle_t \,. \quad (1.7)$$

At thermal equilibrium (with temperature T), the fluctuation-dissipation theorem will be applicable [38], and using the Einstein relation, the diffusion coefficient can be written as:

$$D = \frac{k_\mathrm{B} T}{\gamma} \,, \text{ with } \gamma = 6\pi\eta R \text{ for spherical particles.} \quad (1.8)$$

With the use of the equipartition theorem [38], a set temperature T, the Boltzmann constant k_B, and using equations Eq.1.6 and Eq.1.7 in n dimensions we find:

$$\langle \mathrm{MSD}(\tau) \rangle_t = 2n \cdot \frac{k_\mathrm{B} T}{\gamma} \tau. \quad (1.9)$$

Inserting Eq.1.8 into Eq.1.9 yields the equation for the time-averaged MSD in n dimensions:

$$\langle \mathrm{MSD}(\tau) \rangle_t = 2 \cdot n \cdot D \cdot \tau \quad (1.10)$$

It is noteworthy that Eq.1.10 shows a linear relation between the MSD and the lag time. This behavior is called normal diffusion and is by all means just a special case of diffusion. In the next section, the concepts and origins of anomalous diffusion will be explained.

1.2. Anomalous diffusion

Einstein derived the diffusion equation assuming three fundamental conditions [12]:

(i) independence of individual particles,

(ii) statistical independence of individual displacements, due to the existence of a sufficiently small time scale, and

(iii) a symmetric distribution of particle displacements with $\mu = \langle x \rangle = 0$ and finite 2^{nd} moments of waiting time and step size probability density functions (**PDFs**).

This description of Brownian motion could as well be viewed as a *random walk*. The similarities of this model to diffusion were described more precisely by Smoluchowski in

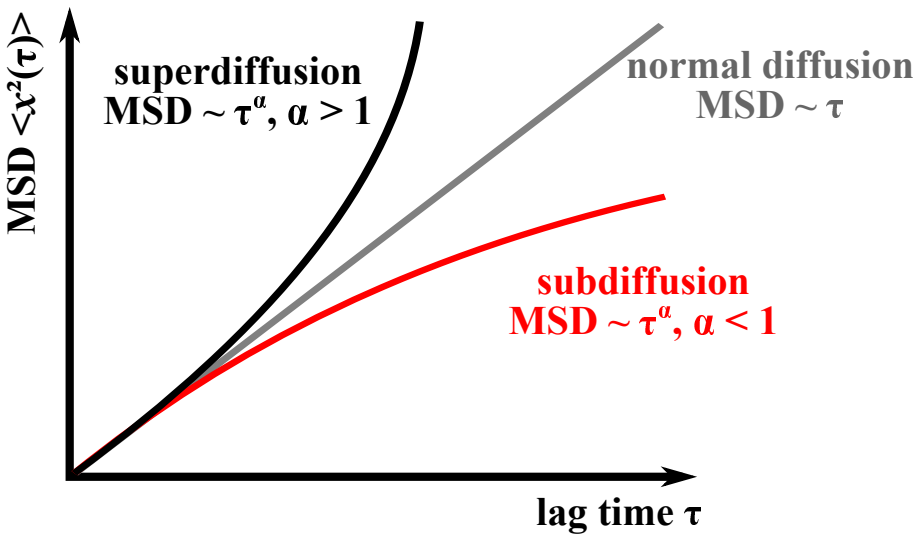

Figure 1.2: Illustration of the temporal development of the mean squared displacement (MSD). Grey: normal diffusion ($\alpha = 1$). Red: subdiffusion ($0 < \alpha < 1$). Black: superdiffusion ($\alpha > 1$).

1906 for the first time [8]. As seen in Eq.1.10, the MSD of such a process grows linearly in time and the diffusion coefficient usually has the dimension of $^{\text{length}^2}/_{\text{time}}$.

Diffusion processes which do not obey this linear relation are typically called anomalous diffusion. They occur if at least one of the aforementioned fundamental assumptions is violated. The origins of this anomalous behavior will be discussed later in this section.

In the case of anomalous diffusion the MSD shows non-linear scaling according to a power-law:

$$\text{MSD}(\tau) = K_\alpha \cdot \tau^\alpha, \text{ with } \alpha \neq 1 \tag{1.11}$$

Here, α denotes the anomaly exponent and K_α is the generalized transport coefficient with units $[K_\alpha] = 1\,^{\text{m}^2}/_{\text{s}^\alpha}$.

Typically three different regimes are classified [12, 15, 16]. The term *subdiffusive behavior* is used for conditions $0 < \alpha < 1$, whereas $\alpha > 1$ describes *superdiffusion*. Ballistic transport, where $\alpha = 2$, determines the upper limit of superdiffusive behavior in most cases. An illustration of different anomalous diffusion behaviors is shown in Fig.1.2 and corresponding sample trajectories can be found in Fig.1.3. The nature and origin of types of anomalous diffusion are explained in the next paragraphs.

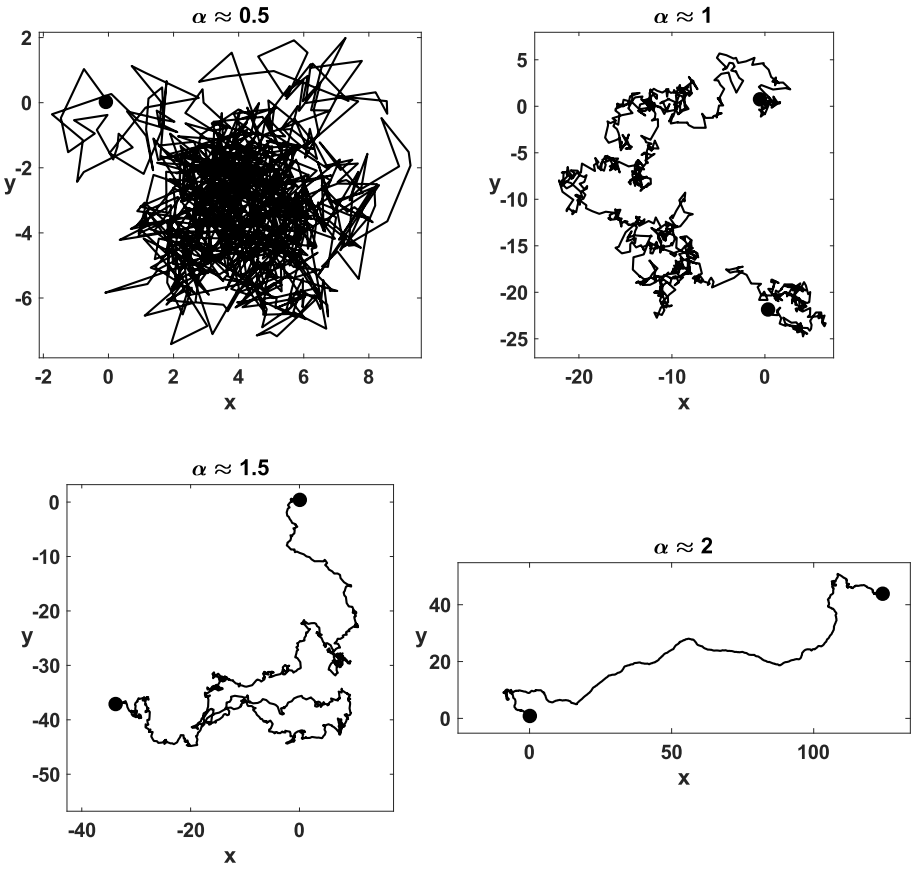

Figure 1.3: Representative trajectories of different types of diffusion. Particle movements were simulated using the wavelet-based synthesis for fractional Brownian motion (fBM) [39, 40] with $N = 10000$ steps. Full black circles show start- and end positions of tracks. Note the increase of length scale with increasing α.

1.2.1. Subdiffusion

Anomalous diffusion with $\alpha < 1$ was observed on many occasions in experiment [6, 11, 22, 27, 33, 34, 41] and studied extensively in theory [12, 16, 17, 20]. This subdiffusive behavior emerges due to three fundamental reasons:

(i) Waiting times in between jumps are drawn from a power-law distribution instead of a Gaussian distribution thus leading to diverging moments,

(ii) the walker is placed in a specifically non-trivial geometrical environment, i.e. a fractal maze of stochastic obstacles, or

(iii) the process is not memory-less, i.e non-Markovian anymore due to the influence of external properties, e.g. a viscoelastic environment.

The origins of these violations can be numerous and hardly non-trivial. Here we focus on the most prominent effects and descriptions.

A **continuous time random walk (CTRW)** as described by Montroll et al. [42] is a direct generalization of the random walk process. It is governed by its random waiting (trapping) times τ which are drawn from a PDF $\psi(\tau)$ in between jumps. The step size can also be a random variable δx chosen from a PDF $\lambda(\delta x)$. It is noteworthy that neither of these distributions show any correlation in time, nor to each other. Assuming a sufficiently narrow distribution $\lambda(\delta x)$ with finite second moment $\langle \delta x^2 \rangle$ and an asymptotic power-law waiting time PDF with a constant scaling factor τ_0, such that

$$\psi(\tau) \simeq \frac{\tau_0^2}{\tau^{1+\alpha}} \tag{1.12}$$

leads straight to an effect on divergence of typical waiting times $\langle \tau \rangle$ and eventually to $\tau \to \infty$ for $0 < \alpha < 1$.

The CTRW is often illustrated by an energy landscape of potential wells with locally varying depth. These 'traps' immobilize travelling particles for a certain dwell time τ depending on their binding energy E_B, with the quantities being connected by the Boltzmann factor [43]:

$$\tau \propto e^{-\frac{E_\mathrm{B}}{k_\mathrm{B}T}}. \tag{1.13}$$

Subdiffusion on an infinitely long time scale can only occur, if a hierarchy of traps with varying potential depth down to minus infinity is created. Due to this, the tracer cannot occupy all of the potential wells, since some traps have diverging dwell times [12]. If this is not the case, the particle will undergo a transition to undisturbed normal diffusion after all traps of comparable binding energy have been explored.

Furthermore, CTRW processes are prone to aging and show weak ergodicity breaking. As shown by Barkai and Bel [44], time- and ensemble-averaged MSDs have different behaviors. Time-averaging revealed normal diffusion, whereas the ensemble-averaged MSDs showed subdiffusive behavior. A more in-depth theoretical analysis can be found in [12] and an example of the CTRW model in biological samples, namely single-molecule diffusion in a plasma membrane, has been studied by Weigel at al. [23].

As stated before, subdiffusion can emerge due to a non-trivial geometry of the underlying space. This model can be described as **diffusion on a percolation cluster** or **hindered diffusion** and was studied extensively by Ben-Avraham, Havlin and Sompolinsky in the 1980 [45, 46]. In the model, the available space is filled with randomly distributed obstacles which create a *crowded environment*. In theory, each point of a lattice has an occupation probability p and stays empty with probability $1-p$. Due to this, some lattice sites cannot be explored by the tracer particle and with increasing p and obstacle concentration a more and more complex environment is formed. Hence, a cluster may adopt more maze-like geometry and the tracers motion becomes subdiffusive. For a certain critical occupation

probability p_c, an infinite cluster is formed and the intrinsic correlation length of the system diverges [12]. These critical probabilities are $p_c \simeq 0.59$ in two dimensions on a square lattice [47, 48] and $p_c \simeq 0.31$ on a three-dimensional simple cubic lattice [47], respectively. With this, the fractal dimensions of the percolation cluster can be calculated to be $d_f = {}^{91}/_{48} \approx 1.896$ in two [49] and $d_f \approx 2.52$ in three dimensions [50]. If a random walker is placed in such a fractal environment and is allowed to move between nearest neighbours occupied sites, he will perform anomalous diffusion with an anomaly depending on the fractal dimension with $\alpha = {}^{4}/_{3 \cdot d_f}$, when using the Alexander Orbach conjecture [12, 51, 52]. In the percolation model, the anomaly exponent as introduced in Eq.1.11 is determined by the shape and size of the obstacles, but primary by their concentration. A rather small concentration c generally leads to normal diffusion, with $\alpha(c)$ depending on the size of the particle [53]. This observation fits with the assumption that the size of a fractal object depends on the size of the 'ruler' with which it is measured as described by Mandelbrot [54]. Therefore, moderate concentrations only lead to subdiffusion in limited regions with fractal structure. At a critical concentration, again an infinite cluster is formed, which is self-similar on all length scales. Hence, transition to normal diffusion is inhibited. For even higher concentrations, more and more initially subdiffusive tracers get captured, due to the dense packing. It is noteworthy that in contrast to CTRW, the percolation model yields ergodic trajectories, i.e. time- and ensemble-averaged MSD show the same scaling behavior.

Anomalous diffusion with $0 < \alpha < 1$ can also be observed in various kinds of viscoelastic media ranging from dense polymer networks [26] to the cytoplasm of living cells [55]. These media have characteristic responses to shear stress and a complex shear modulus that scales as $G(\omega) \sim \omega^{\alpha}$ which gives a plausible interpretation for antipersistent memory effects [24, 56–60]. They dissipate some of the deformation energy like viscous fluids, but also store another part like an elastic solid [61]. This behavior rises from multi-atomar structures that extend in the viscous medium. When a particle moves in such a medium due to thermal fluctuations, some of the surrounding molecules are shifted irreversibly, but others relax towards their initial condition after the deformation force is removed, due to them being intertwined to other molecules. The latter exerts a repulsive force to the particle and can be described by a non-Markovian memory kernel, i.e. future steps depend on past increments in some way. This effect leads to overall subdiffusive motion of the single particle and is described by the term **fractional Brownian motion (fBM)**. An example of a fBM trajectory with $\alpha \approx 0.5$ is shown in Fig.1.3 upper left panel. The particles movements were simulated using the wavelet-based synthesis for fractional Brownian motion algorithm, `wfbm` in `MATLAB` using a Hurst coefficient of $H = 0.25$ [39, 40]. The full black circle shows the starting position. Note that the end position cannot be shown here with another full black circle due to the density of the trajectory.

Next to sterical obstructions in a viscoelastic environment, recent studies by Etoc et al. [30] have revealed, that the subdiffusive nature of nano-particle transport in a crowded environment inside the cell is presumably not only due to excluded-volume effects and restrictions by inaccessible sub-volumes, but evoked by **non-specific interactions** with intracellular components [62]. However, the exact binding partners remain elusive until this point in time.

1.2.2. Superdiffusion and persistent motion

A Markovian random walk with heavy-tailed step length probability distribution, which ultimately leads to superdiffusion, is called a **Lévy flight** [54]. The generally power-law distributed step-sizes lead to a stable distribution of distances to the origin of the walk after a sufficiently large number of steps. Trajectories of this kind of motion typically show accumulation in limited space occasionally connected by long 'jumps'. A lot of processes in mathematics, physics and nature can be modeled using Lévy flights, e.g. marine predators searching for food [63], eye movements and gaze shifts [2] , or optimization theory [64].

Superdiffusion may also occur when Brownian motion is fuelled by a *persistent* fractional Gaussian noise $F'(t) = \xi(t)$, that has a standard normal distribution, but is positively power-law correlated (for any $t > 0$ and $1 < \alpha < 2$) according to:

$$\langle \xi(t_1)\xi(t_2)\rangle = \alpha(\alpha-1)K_\alpha \cdot |t_1 - t_2|^{\alpha-2}. \tag{1.14}$$

An example trajectory is shown in Fig.1.3 lower panels.

When describing **persistent random motion** as performed by certain cells, some colloids or other particles and organisms [65], the *Ornstein–Uhlenbeck* process [66] has been the archetypal model of choice. The O–U process is a stationary Gauss–Markov process defined by the Langevin equation for the velocity vector:

$$\frac{\mathrm{d}}{\mathrm{dt}}\mathbf{v} + \frac{1}{\tau_\mathrm{P}}\mathbf{v} - \frac{\sqrt{2D}}{\tau_\mathrm{P}}F'(t) = 0\,, \tag{1.15}$$

where D is the diffusion coefficient, τ_P is a characteristic timescale, called persistence time, and $F'(t)$ is a thermal, white noise component as stated earlier. In a similar manner as described before, the mean squared displacement can be derived starting from Eq.1.15. The MSD of an n-dimensional O–U process is also known as *Fürth* formula [67] and has been often stated to fit experimentally observed behavior well [65]:

$$\langle \mathbf{x}^2(t)\rangle = 2nD\tau_\mathrm{P}\left(\exp\left\{-\frac{t}{\tau_\mathrm{P}}\right\} + \frac{t}{\tau_\mathrm{P}} - 1\right). \tag{1.16}$$

Note here the similarity to Eq.1.10 and the divergence for $\lim_{\tau_\mathrm{P}\to\infty}\langle \mathbf{x}^2(t)\rangle = \infty$.

1.3. Fundamentals of eukaryotic cells

The **HeLa** cell line – primeraly used during the work on this thesis – was derived from human cervical cancer cells taken from Henrietta Lacks on February 8, 1951 and is one of the oldest and most commonly used human cell line in scientific research [68]. The upcoming abstracts of the eukaryotic cell and its compartments are adapted from [69].

Eukaryotic cells are the building blocks of all more complex multicellular organisms, including animals, plants & fungi. They are more elaborated than prokaryotes (bacteria or archaea) and generally bigger, with average cell sizes ranging from $10 - 50\,\mu m$, and some exceeding $200\,\mu m$ in diameter. By definition, all eukaryotic cells have a nucleus enclosed by a membrane, but typically feature a broad variety of intracelluar compartments and membrane-bound organelles. A schematic overview of a cell with its most prominent compartments can be seen in Fig.1.4. Next, the main organelles and their functionality will be discussed briefly.

The most prominent part of a cell is usually the **nucleus**. It is enclosed by the nuclear envelope with pores allowing for active transport between nucleus and cytoplasm. Its is used to store the genome of the cell, as well as for transcription and DNA replication. The nucleus itself contains one or more other large structures called the **nucleoli**, which are made of proteins and are best known as sites of ribosome biogenesis and response to

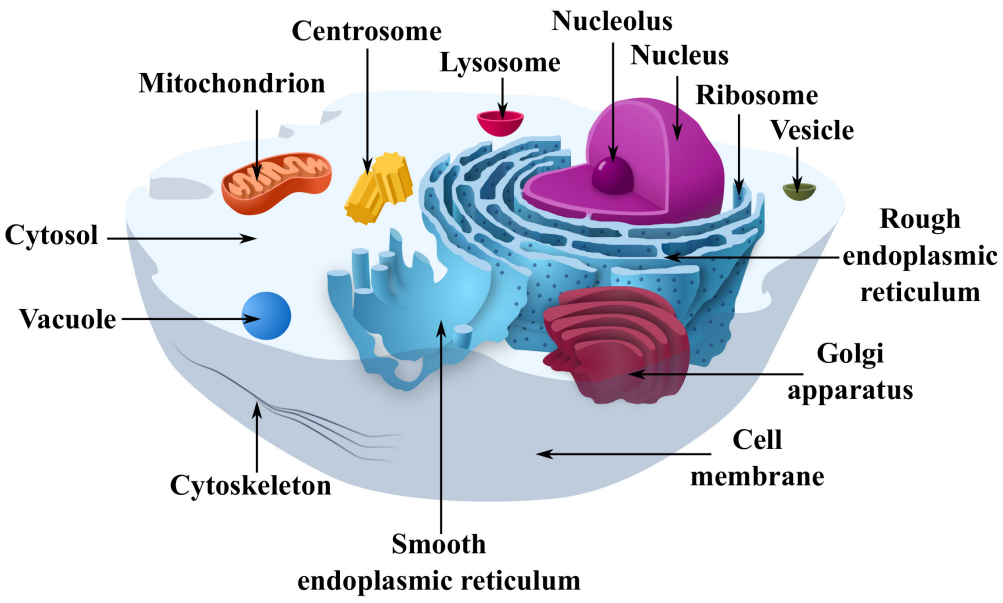

Figure 1.4: Schematic 3D cross sectional representation of a typical eukaryotic (animal) cell with its most prominent components. Diagram adapted from [70].

cell stress levels [71]. Next to the nucleus is the **endoplasmic reticulum (ER)**, which forms an interconnected network of flattened, membrane-enclosed cisternae and tubular structures. It is the site where most cell membrane components, as well as other materials such as lipids and cholesterol are synthesized. Note here that the difference between rough and smooth ER does not seem to be as distinct as formerly assumed as more recent studies revealed [72]. Smaller organelles called **ribosomes** are located in large numbers on the rough ER. These complex macromelecular machines are crucial in living cells, since they link amino acids together in the order specified by messenger RNA (mRNA). Thus, they are the site of translation (biological protein synthesis).

The **Golgi apparatus**, like the ER, is part of the endomembrane system. The Golgi apparatus is involved in the synthesis and packing of molecules into membrane-bound **vesicles** destined to be secreted from the cell. The whole cell is enclosed by the **cell membrane**, which is a lipid-bilayer membrane separating the inside from the extracellular matrix. **Vacuoles** are only present in some animal cells, but in all fungi and plant cells. They are essentially closed water- & enzyme-filled compartments formed by fusion of multiple membrane vesicles. **Lysosomes** are specific kinds of vesicles, which contain hydrolytic enzymes. They are used for decomposition of many kinds of biomolecules, e.g. during phagocytosis.

The **cytoskeleton** of eukaryotic cells is a widespread protein filament network with complex and highly dynamic linkages. It is mainly composed of microfilaments and microtubules (MT), both are capable of rapid assembly and disassembly depending on the circumstances. Microtubules are formed by the polymerization of a dimer of alpha and beta tubulin into a protofilament that self-assembles to a hollow tube. These tubes can grow up to 50 µm, have a diameter of $\varnothing \approx 25\,\text{nm}$ [73], and are the main backbone of the cell. Micro- or actin filaments usually have a diameter of $\varnothing \approx 7\,\text{nm}$ [74] and hence are the slender and more flexible part of the cytoskeleton. Nevertheless, they are relatively strong [75] and crucial for e.g. cytokinesis [76], cell motility [77], endocytosis [78] and mechanical stability [75, 79]. The **centrosome** is closely linked to the cytoskeleton, since it serves as the main hub of microtubules, i.e. the microtubule organisation center (MTOC) in animal cells. It is composed of two centrioles perpendicular to each other, surrounded by the pericentriolar material (PCM). This amorphous mass of protein mainly contains γ-tubulin, ninein and pericentrin and is responsible for MT anchoring and nucleation [80]. It is essential to the process separating chromosomes into two individual new nuclei during the cell-division cycle, called mitosis. The cell cycle will be discussed in Sec.1.3.2.

The "powerhouse of the cell" term for **mitochondria** was popularized in the late 1950 by Siekevitz [81], but the $(0.75 - 3)\mu\text{m}^2$ sized [82], double-membrane-bound organelles are "more than just a powerhouse" [83]. In fact, they are involved in cellular differentiation, cell death and growth, and signaling just to mention a few [83]. But most importantly,

mitochandria are generators of chemical energy for the cell. They harness the energy from oxidation of food molecules, such as sugars, to produce adenosine triphosphate (ATP), which is the basic chemical fuel for most of the cell's activities. Mitochondria are – besides the nucleus – special in the way, that they contain their own genome that shows surprising similarities to bacterial genome. This peculiarity prompts some researchers to belief they were derived from some kind of bacteria that were engulfed by ancestors of present-day eukaryotic cells, thus, eventually creating a symbiotic relationship. More information on the origins of mitochondria can be found in [84, 85].

All the aforementioned organelles are embedded in the **cytosol** of the cell. This largest of organelles is a gel-like substance with various cytoplasmic inclusions comprised of roughly 80% water [86]. Due to it being host to a large variety of small and large molecules [87, 88], the cytosol behaves more like an aqueous gel than a liquid solution. The cytosol is the site of many chemical reactions fundamental to the cell's existence. Proteins are manufactured within it, as well as early breakdown of nutrient molecules just to mention two examples. The entirety of cytosol and all organelles except the nucleus is called the **cytoplasm**.

1.3.1. Macromolecular crowding and heterogeneity

The just mentioned cytoplasm of mammalian cells is home to a plethora of macromolecules, organelles of different nature, and molecular compounds of varying complexity [87, 88]. Since not one single species of molecules governs the majority of occupied space in the environment, but rather the entirety of a lot of different molecules defines the properties in these surroundings, the environments are called crowded. Individual concentrations of molecules might be fairly low in the cytoplasm, but the overall concentration of molecules can be in the range of $200 - 500\,\mathrm{mg/ml}$ [28]. Therefore, it seems plausible that crowding may effect motion properties of embedded tracers. A possible change in diffusive behavior could be explained due to the visco-elastic environment the molecules build, since they are densly packed (see fBM in Sec.1.2); or due to the fact that an embedded tracer has to navigate a maze of obstacles (hindered diffusion). As of yet, no general agreement on a physical model explaining all facettes of cytoplasmic subdiffusion exists. Nevertheless, anomalous diffusion has already been linked to cytoplasmic crowding to some extend [15, 33]. However, the anomalies found in experiments conducted in the cytoplasm are often even more pronounced than similar artificial crowded environments would suggest. Hence, pure macromolecular crowding does not seem to fully explain the emergence of strong subdiffusion in the cell. Furthermore spatial and temporal heterogeneity has been reported more frequently in recent years [27, 29, 30, 89, 90]. These heterogeneities could be induced by caging effects [22], non-specific binding [30], underlying heterogeneous processes [19] driving the diffusion, or spatiotemporal variations of transport coefficients [12, 21].

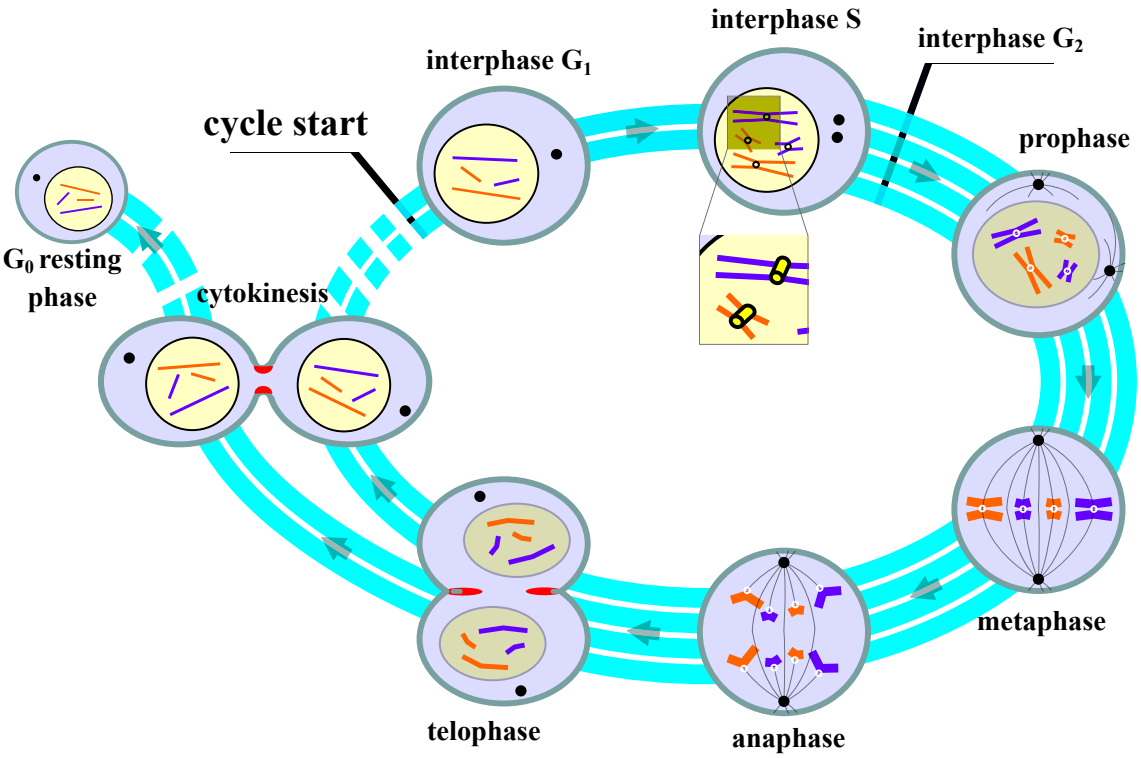

Figure 1.5: The division of a cell into two daughter cells. During interphase, the cell increases in size, the DNA of the chromosomes is replicated, and the centrosome is duplicated. The mitotic phase (M phase) consists of nuclear division, or mitosis, and cytoplasmic division, or cytokinesis. The M phase itself is divided into prophase, prometaphase (not shown here), metaphase, anaphase & telophase. Diagram adapted from [91].

1.3.2. The cell cycle

The cell cycle describes a series of events in the cell that eventually lead to the duplication of one mother cell into two daughter cells. It involves DNA replication and cytoplasmic division. Two main stages are assigned to the cycle in eukaryotic cells, the first one being **interphase** and the second one is the **mitotic phase**. Both of these phases are divided into several subphases which are described in the following paragraphs. A diagram of the entirety of the cell cycle is shown in Fig.1.5.

Interphase The first part of interphase is called **Gap 1 (G_1)**, in which the cell grows in size. In this phase, the nuclear envelope is still intact, the chromosomes are decondensed (red and blue lines), and only one centrosome exists as denoted by the full black circle. The G_1 checkpoint control mechanism ensures that everything is ready for DNA replication, which subsequently takes place in the **synthesis (S)** phase. This process is illustrated in Fig.1.5 in a simplified manner with the yellow tubes representing the complex machinery which is required to fulfill this task. For closer details a higher cell biology textbook, e.g.

[69] can be consulted. Note that in interphase S, the centrosomes duplicated, and the rates of RNA transcription and protein synthesis are very low. The last step in interphase is called **Gap 2 (G_2)**. Here the cell grows some more until the G_2 checkpoint is reached and everything is ready to enter the mitotic phase.

Mitotic phase In **prophase**, the replicated chromosomes, each consisting of two identical, closely associated sister chromatids, condense. This is illustrated with broader red and blue lines. The kinetochores (white circle) assemble at the centromere of the chromosome. Outside the still intact nuclear envelope, the centrosomes start to move apart and the mitotic spindle (thin black lines) assemble between them. **Prometaphase** (not shown in Fig.1.5) starts abruptly with the breakdown of the nuclear envelope. Subsequently, spindle microtubules invade the nuclear space and attach to the kinetochores allowing the chromosome to undergo active movement. Polar microtubules start pushing against each other, thus moving the centrosomes further apart. At **metaphase**, the chromosomes are aligned at the equator of the spindle, thus forming the so called metaphase plate midway between the spindle poles. This even alignment is counterbalanced by the pulling forces of the microtubules in a similar fashion to a tug-of-war of more or less equal strength. This eventually leads to the destruction of cyclin B [92] and successful transition to **anaphase**.

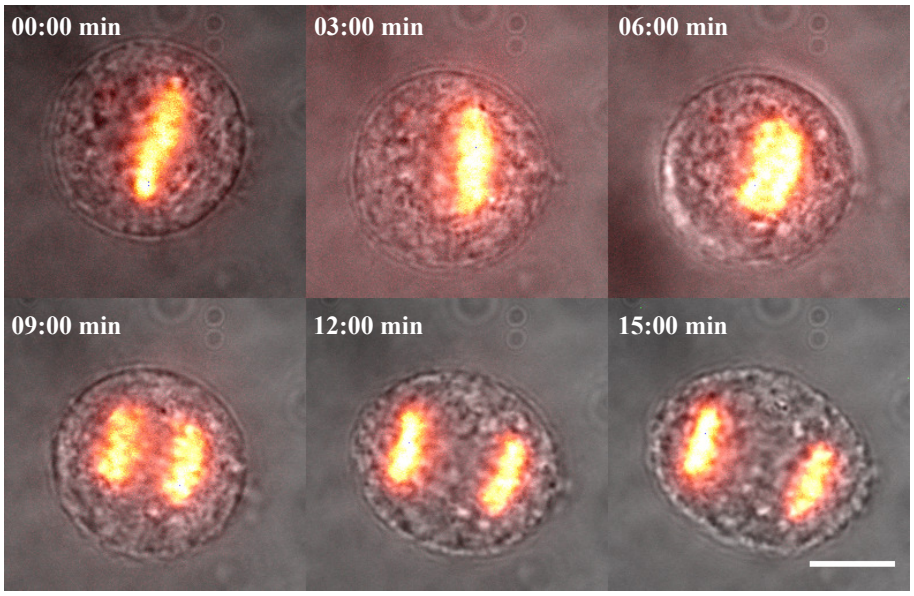

Figure 1.6: Time series of a HeLa cell undergoing cell division. Imaging was done with a wide-field/epifluorescence microscope and a 100x objective. Cells were measured at $T = 37\,°\mathrm{C}$. Chromatin was stained using Hoechst 33342. Further details can be found in Sec.2.2. The first panel shows the chromosomes aligned in metaphase plate. Panels with time stamps (03:00-12:00)min show the sister chromatids as they are pulled by microtubules to opposite sites of the spindle. The last panel shows the cell at the edge to telophase where the two sets of chromatins unwind again and a contractile ring starts to pinch the cell. Scale bar 10 µm.

At this stage of the cell cycle, chromosomes synchronously break at the centromeres and each individual sister chromatid is pulled slowly towards opposing spindle poles. Both, the shortening of kinetochores microtubules, as well as the movement of the poles contribute to chromosome segregation. A time series of a cell undergoing division from meta- to telophase is shown in Fig.1.6. The DNA in this experiments was visualized using the organic compound Hoechst 33342 as a fluorescent dye. During **telophase**, the two sets of chromosomes arrive at the spindle poles and subsequently unwind into chromatin. A new nuclear membrane assembles, reforming the nuclear envelope around each set of chromatin, thus completing the formation of two new nuclei. This event marks the end of mitosis. In addition to this, the division of the cytoplasm begins with the formation of a contractile myosin II and actin filament ring (shown in red in Fig.1.5). The process of division of cytoplasm is called **cytokinesis**. The actin and myosin filament ring cleaves the cell until eventually two daughter cells emerge and the cycle may start all over again.

It is possible for the cell to leave the replicative cell cycle and to become arrested in a so called **resting phase (G_0)**. This phase can be evoked by contact inhibition, i.e. cells are to dense and stop dividing [93], or multiple other stress factors. The most prominent of these triggers is starvation of cells [94], but others have been shown to get equal results [95]. The **quiescent state** is i.a. initiated by microtubules that - originating from spindle poles - cover up the nucleus [96]. A terminal G_0 resting state also occurs for most fully differentiated metabolic active cells and adult neurons.

1.4. The kinetoplastid Tryponosoma brucei

In 1894 David Bruce observed a species of parasitic kinetoplastea belonging to the genus *Trypanosoma* in the blood of a south African cow, which was named *Trypanosoma Brucei* in his honor in 1899 [97, 98]. The group of kinetoplastea is made up of flagellated protists (eukaryotic cells, that do not belong to fungi, plants, or animals) belonging to a variety of common free-living species of phylum Euglenozoa [99–101]. *T. brucei* is traditionally grouped into three subspecies, of which two are human parasites and one is a non-human vertebrate parasite. This three species are: *T. b. gambiense* & *T. b. rhodensiense*, that infect humans, and the one initially observed, *T. brucei* [98].

The about 15 µm long parasite [102] causes a vector-borne disease in vertebrates that is called *African trypanosomiasis*, better know as sleeping sickness in humans. It is transmitted via *tsetse* flies as insect vectors between mammalian hosts, by biting during the insect's blood meal. Over the course of their life cycle, the parasite undergoes massive changes in morphology and in cell surface proteins that may cause antigenic variation and eventually enables persistent evasion of the mammalian host's adaptive immunity, i.e. leading to chronic infections [98, 103].

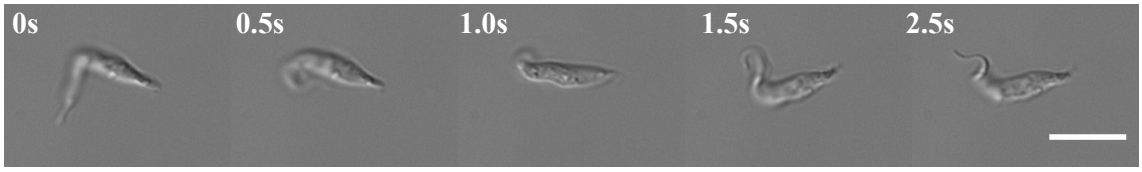

Figure 1.7: Time series of a parental 29-13 (wild-type) *Trypanosoma brucei* in motion. Images were acquired using a bright field (BF) microscope equipped with a 20x dry objective and a recording frequency of $\nu = 10\,\mathrm{Hz}$. For convenience only every fifth image is displayed. The beating flagellum is clearly visible on the left side of the parasite. Note that the kinetoplastid is moving in direction of the flagellum (here from right to left) in every panel. Scale bar 10 µm.

In the course of this thesis, only non-infectious procyclical *T. brucei* in their insect vector form were used for experiments. A typical time series of a wild type (WT) parasite in motion can be found in Fig.1.7. The beating flagellum is clearly visible and the cork screw-like motion can be observed. It is noteworthy that the *T. brucei* moves in direction of the flagellum, i.e. from right to left in every panel. Fig.1.8 shows a false color scanning electron microscopy (SEM) image of a *T. brucei* found in the gut of a *tsetse* fly host. The body is shown in orange and the flagellum is colored in red. The single flagellum, which is a crucial and multifunctional organelle involved in cell propulsion, morphogenesis and cytokinesis, is mostly build of cytoskeletal filaments (microtubules).

The shape of the trypanosomes body itself is crucially dependent on their subpellicular cytoskeleton, a highly ordered array of sub-plasma membrane, parallel microtubules [102]. In contrast to the dynamic mammalian microtubule network, the MT corset in trypanosomes is highly stable, yet a transient dynamic nature has to be implemented during the life cycle differentiation [104, 105]. How such transitions between dynamic and stable phases are regulated is yet to be discovered. In contrast to mammalian cells where regulation of MT dynamics is well characterized via biochemical properties of tubulins, activities of MT-associated proteins (MAPs), and posttranslational modifications of alpha- and beta tubulin [106], the regulating mechanisms for trypanosomes are widely unknown. Since *T. brucei* only have one alpha- and beta-tubulin tandem repeat in their genome, regulation via differential isoforms is not an option. Therefore, posttranslational modifications of tubulin are of interest to explain the phenomenon. These changes are done by specific enzymes, of which the largest group is the family of tubulin-tyrosine ligase like proteins (TTLL) [107]. Hence, these enzymes are of special interest regarding the structure of the subpellicular cytoskeleton which may affect the function of the flagellum and in turn eventually has influences on the motility and mobility of single organisms.

Figure 1.8: False color SEM of procyclic form of *Trypanosoma brucei* found in the gut of tsetse fly host. The cell body is shown in orange and the flagellum is color coded red. Figure adapted from [108]. Scale bar 5 µm.

1.5. Microscopy & fundamentals of image acquisition

Microscopy is a widely spread experimental technique in biophysics, medicine and biology. It includes the application of microscopes to view objects that would be to small to resolve with the naked eye only. Primitive magnification glasses, lenses and eye ware have been used for centuries and in the 1670s Antonie van Leeuwenhoek pioneered as the first acknowledged microscopist with the development of a simple, yet high magnification microscope [109].

Today there are several other state-of-the-art microscopy techniques besides light microscopy, e.g. electron, X-ray or atomic force (AFM) microscopy. None of the latter have been used in the course of this work, hence the following paragraphs will only deal with light microscopy, its sub-types and applications in more detail.

Compound microscopes are the most prominent representatives of light microscopes. They come in various shapes, setups, and applications such as inverted, stereoscopic, phase contrast, or differential interference contrast (DIC) microscopes just to mention a few. However, their basic structure is similar. In total, only three things are required. First, a light source of some kind must be focused onto the specimen by lenses in the condenser to guarantee sufficient illumination. Second, at minimum a single lens close to the specimen – called the objective – focuses a real image inside the microscope. Third, the eyepiece or ocular magnifies this real image and projects it onto a detector as an enlarged inverted virtual image of the studied objects [69].

1.5.1. Fluorescence microscopy

In fluorescence microscopes the specimen is detected with the aid of fluorescent dyes. These fluorophores are chemical compounds that re-emit light upon excitation with specific electromagnetic radiation. The emitted light typically has lower energy and hence a longer wavelength then the absorbed radiation. This phenomenon is called *Stokes shift* and is the critical property that makes fluorescence so powerful. By filtering out all of the excitation light and allowing the emitted fluorescence to freely pass to the detector, it is possible to see only fluorescently labeled objects [110]. This renders the approach superior to absorption techniques, since with fluorescence even single molecules are visible if the signal-to-noise ration (SNR) is sufficiently high.

A useful tool for understanding excitation and emission processes in fluorophores is given by the **Jablonski diagram**. This more graphic approach was first conceived by the polish physicist Aleksander Jabloński in the 1930s [111]. An example of a Jablonski diagram is shown in Fig.1.9. The singlet states (S) of the molecule are shown on the left side of the diagram. The ground state is identified by S_0 and represents the lowest energy, i.e. the energy of a molecule that has not been excited by electromagnetic radiation. The higher levels S_1 and S_2 (not shown in Fig.1.9) represent excited singlet states with higher energy in which an outer electron is boosted into a different orbit. Note that all the singlet states maintain the paired $\pm 1/2$ spin states of the electrons with each electron in a pair having opposite spins [110]. In contrast to the singlet states, in triplet states (right side of Fig.1.9) an outer electron is not only boosted to a new orbital, but has also undergone a subsequent reversal in spin. Therefore, the former pair of electrons are now parallel in spin. This transition is forbidden in quantum theory at zero Kelvin due to no collisions, hence making it relatively unlikely to happen. Nevertheless, electrons sometimes undergo this intersystem crossings from singlet to triplet state.

When a fluorophore molecule is excited by a photon of a certain wavelength λ_0, the radiation is absorbed and a transition from ground state to S_1 with higher energy takes place. The photon itself caries an energy inversely proportional to its wavelength

$$E_0 = h\frac{c_0}{\lambda_0}. \tag{1.17}$$

In Eq.1.17, h is the Planck constant and c_0 is the speed of light in vacuum. The absorption takes place on a femtosecond (10^{-15} s) timescale and is indicated with a blue arrow in Fig.1.9. The system subsequently relaxes with non-radiative transitions – indicated by small black curved arrows – to a lower energy in the excited state within some picoseconds (10^{-12} s). Following these transition, the system may emit a photon with an energy lower than E_0, i.e. the emitted light has a longer wavelength. The process which takes place in nanoseconds (10^{-9} s) is called fluorescence and is indicated with a green arrow. Next to

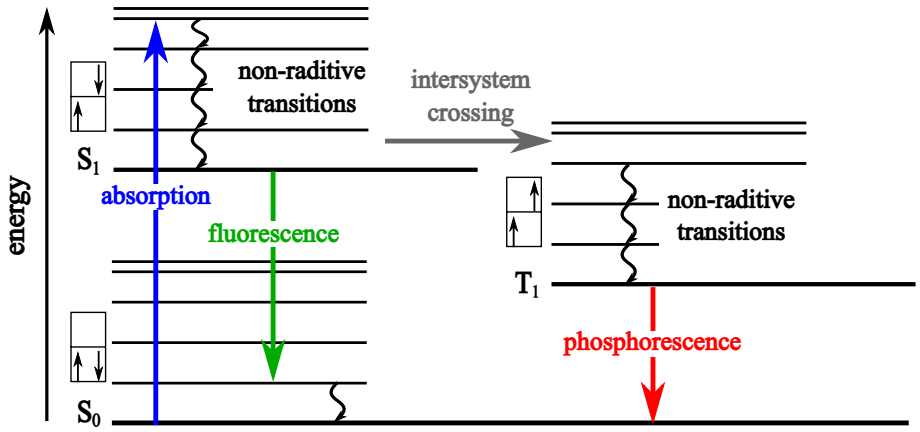

Figure 1.9: Jablonski diagram displaying the energy states of a molecule. S_0 indicates the singlet ground state with lowest possible energy. After a photon of energy E_0 is absorbed (blue arrow), the system is in the excited singled state S_1. It undergoes non-radiative transitions and subsequently emits a photon of longer wavelength (green arrow). Due to overlap in energy levels of S_1 & T_1 (triplet state), the system may also cross over (gray arrow) and subsequently convert to a lower triplet energy level ('forbidden transition'). From here, it takes another forbidden transition to emit a photon of even less energy than fluorescence. This process – indicated by a red arrow – is called phosphorescence.

fluorescence, intertsystem crossing describes another pathway of energy loss in the excited S_1 singlet state. Many fluorophores show overlap of their triplet state vibrational energy levels with their respective lowest S_1 energy. This favors the aforementioned forbidden transition from an excited singlet to a triplet state as indicated by the gray arrow. After internal conversion to the lowest T_1 energy level, there is no easy way back to the singlet ground state. The outer electron has to again undergo a forbidden transition. Since these transitions are unlikely, an emission event on the microsecond (10^{-6} s) timescale may occur, which is called phosphorescence (red arrow in Fig.1.9). Some of the triplet state molecules may also undergo photochemical reactions that eventually result in irreversible bleaching and phototoxicity.

Fluorophores come in a variety of colors and shapes. They typically are constructed from several atomic groups, or planar or cyclic molecules with several π-bonds [112]. A lot of these chromophores were synthesized artificially, but some of them occur naturally. The most prominent of the latter is the so called **green fluorescent protein (GFP)** that was first isolated from the jellyfish *Aequorea victoria* and studied by Osamu Shimomura in 1962 [113, 114]. For his outstanding work on the discovery and development of GFP, he later received the Nobel Prize in Chemistry in 2008 together with Roger Tsien and Martin Chalfie. Since the potential of fluorescent proteins is enormous and its usage is widespread among researchers, many different mutants of GFP have been engineered [114]. The first major improvements were made by Tsien et al. in 1995 [115]. They managed to increase the fluorescence and photostability while shifting the major excitation peak to 488 nm,

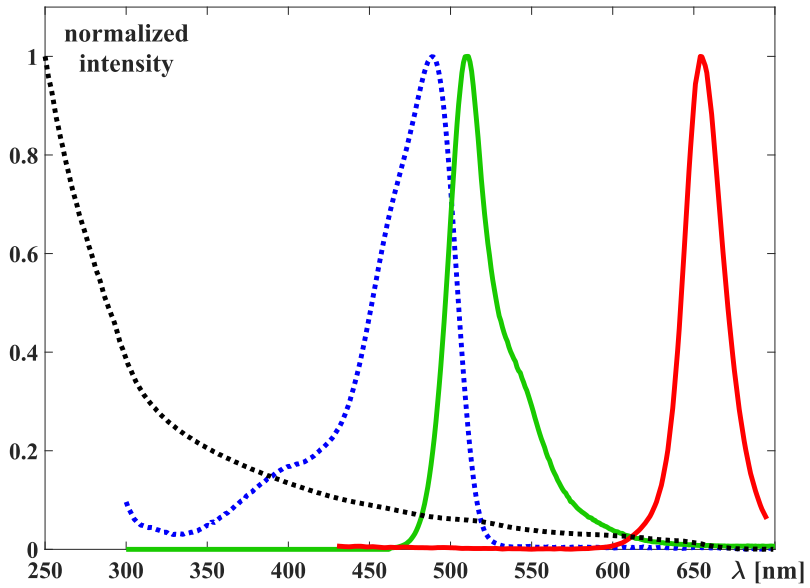

Figure 1.10: Absorption (dotted lines) and emission (full lines) spectra of two different kinds of marker. The EGFP absorption (blue) has a maximum at $\lambda_{ex} = 488\,\text{nm}$ while the Stokes shifted emission (green) has a maximum at $\lambda_{em} = 510\,\text{nm}$. Note the symmetry of absorption and emission spectrum of EGFP due to similarities of transition to vibrational singlet states [110]. In contrast to fluorophores, quantum dots have a broad excitation spectrum (dotted black line) and a pronounced emission peak (red) at a wavelength depending on their actual size.

thus now fitting commonly available FITC filter sets. The use of GFP in mammalian cells was allowed by the discovery of **enhanced GFP (EGFP)** in 1995 [116]. The absorption and emission spectra of EGFP can be found in Fig.1.10. The maximum of the absorption spectrum (dotted blue line) is, as stated before, at $\lambda_{ex} = 488\,\text{nm}$ while the Stokes shifted emission (solid green line) has a maximum at $\lambda_{em} = 510\,\text{nm}$. The symmetry between the absorption and emission curves are noteworthy in these spectra. They occur owing to the similarity of transitions to vibrational states in S_0 and S_1 of the molecules.

Another possible marker species for quantitative measurements of small scale fluctuations and imaging in cells are **quantum dots (qdots)**. These tiny semiconductor particles of only a few nanometers extent have deviating electric and optical properties compared to larger particles due to quantum mechanical effects. When a semiconducting quantum dot is exposed to light in the excitation range – in most cases UV light – an electron may transition from its valence band to the conductance band. Subsequently, the excited electron drops back to the valence band releasing its energy in the from of a photon during the process. This light emission is called photoluminescence. Since the wavelength of the emitted light is depending on the energy differences between valence and conductance band, qdots' color can be tuned using their general composition and size [117]. The excitation and emission spectra of qdots primarily used during the course of this thesis are shown in Fig.1.10. The dotted black curve depicts the wide range of excitation wavelength, from

UV to visible light and is similar in shape for most quantum dot subspecies, whereas the solid red line is the emission spectrum with a pronounced peak at a certain wavelength. Despite their broad wavelength range of light absorption, the emission wavelength of these materials is independent of the excitation wavelength. For example, whether exciting at 400 nm or 633 nm, the shape of the emission band of Qdot 655 nanocrystals remains the same, while the intensity is approximately 11-fold higher at equal input powers with 400 nm excitation. Light absorption and consequent excitation at shorter wavelength, with fixed emission, results in a large 'apparent Stokes shift'. Short wavelength excitation improves sensitivity by reducing autofluorescence and takes advantage of the inherently greater light absorption of these materials in the blue to violet spectral region [117]. The quantum dots used during the course of this thesis will be explained in more detail in section 2.2.1. One advantage of quantum dots over fluorophores is the photostability of the semiconductor nanocrystals. They show less bleaching as well as a higher brightness owing to the high extinction coefficient combined with a comparable quantum yield to fluorescent dyes [117]. Thus, they are excellent tracers for long-term live-cell imaging and dynamics studies. A minor drawback of quantum dots is their irregular blinking that might perturb tracking experiments. However, depending on the choice of quantum dots and experimental circumstances, single particle tracking (SPT) experiments with quantum dots have demonstrated their versatile character [118].

Most of the fluorescence microscopes, especially those used in the life sciences, are **epi-fluorescence microscopes**. The schematic representation of their design is shown in Fig.1.11. It is similar to an ordinary light microscope except that the illuminating light is passed through two sets of filters adjusted to the specific wavelengths. Light from a light source passes the excitation filter, where all but the relevant wavelengths are absorbed, thus leaving only the appropriate range through. Note that usually dichroic mirrors are used in these kind of setups to redirect the light to the objective. The light illuminates the fluorophores in the specimen through the objective lens. In return photons of a different, higher wavelength are emitted and the fluorescence is focused to the detector by the same objective. Note here that for greater resolution of the images a higher numerical aperture (NA) is needed. On its way, the emission light now passes the dichroic mirror and is filtered again for potential autofluorescence and background light by the emission filter. Eventually only the emitted fluorescence reaches the detector. With this method a higher SNR compared to ordinary light microscopy can be achieved [69, 110, 119].

A more advanced fluorescence microscopy technique is the **confocal laser scanning microscope (cLSM)**. In contrast to conventional (i.e. wide-field) fluorescence microscopy where the entire specimen is flooded evenly with light and all parts are excited at the same time, a cLSM uses illumination of a distinct spatially limited spot only. This is achieved by adding a pinhole in an optically conjugated plane to the point detector so that only

fluorescence emitted from the focal plane is detected and out-of-focus light is blocked [120]. Emission and detection focal planes overlap in this configuration, hence the term confocal. A schematic illustration of a cLSM is shown in Fig.1.12. Changing the pinhole size enables variation of detected intensity and z-discrimination, thus allowing enhancements in optical resolution and contrast. The focal volume is shifted in the specimen with the aid of scanning mirrors, hence enabling the creation of a more dimensional image when using a point detector. Note here that only one point at a time is detected and the resulting image is thus a montage of multiple single images and not all parts of the specimen are excited at the exact same time. Regarding this aspect it becomes clear that the scanning speed and dwell time per pixel are crucial quantities for a laser scanning microscope and therefore have to be adapted to fit the experimental needs. This could lead to artifacts in dynamic, rapidly changing systems, or to more pronounced bleaching and phototoxicity due to the specimen being exposed to more energy during long-term measurements.

In order to perform fluorescence microscopy, the right choices of settings have to be made. Beginning with the light source, an intense, near monochromatic illumination is required. The main three types of light sources used in most commercial and home-build setups are: mercury-vapor or xenon-arc lamps with excitation filters, lasers, and high-power LEDs. Lamp and filter combinations and LEDs are more commonly used for widefield epifluo-

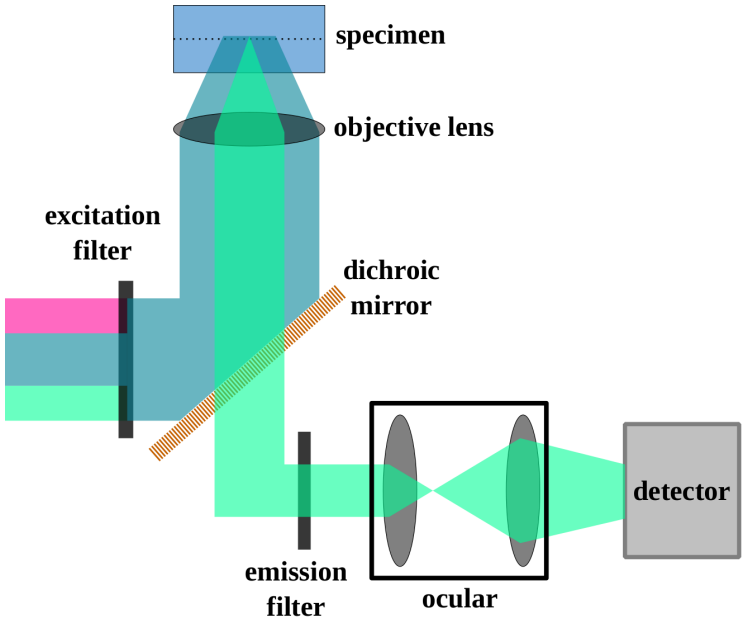

Figure 1.11: Schematic representation of an epifluorescence microscope. Illumination from a light source passes the excitation filter, where all not-suitable wavelengths are suppressed. A dichroic mirror is used to redirect the light to illuminate the fluorophores in the specimen through the objective lens (shown in blue). The emitted photons, here shown in green to symbolize the Stokes shift, pass the objective again first and an emission filter second. The latter ensures that only fluorescence from the targeted wavelength range is collected by the detector.

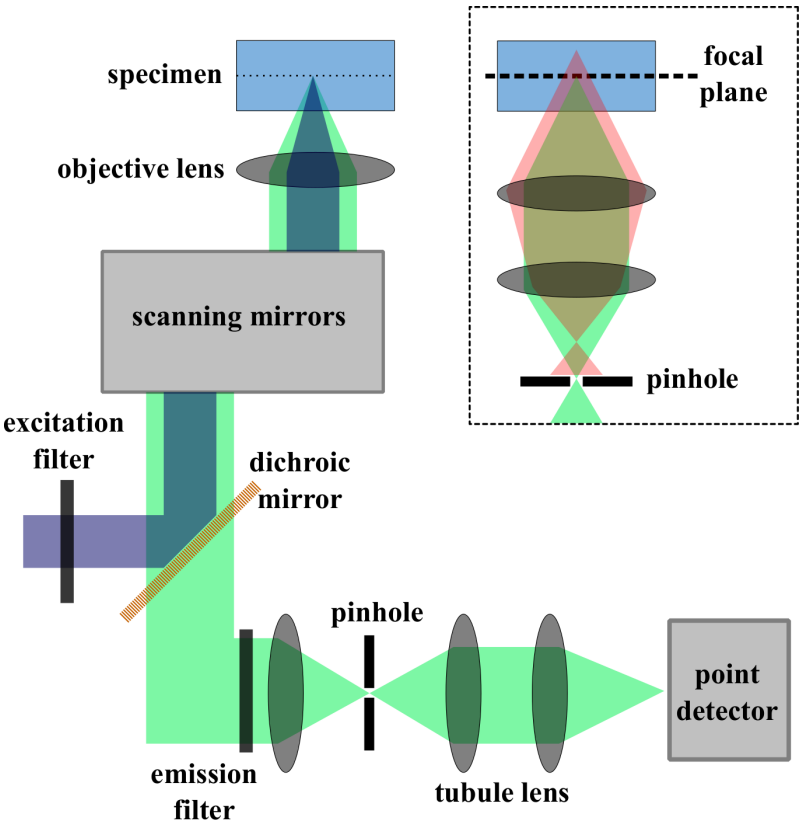

Figure 1.12: Schematic representation of a confocal laser scanning microscope. The illumination (blue) is selected by wavelength via an excitation filter. Scanning mirrors move the focus in the focal plane. Similar to an epifluorescence microscope, the emission light (green) passes a dichroic filter and is filtered for background and back scattered light via an emission filter. A pinhole in the pathway is used for spatial selection and blocking out-of-focus light (see inset: red light path) before a tubular lens system projects the image onto a point detector.

rescence microscopy, whereas lasers are usually used for more advanced applications like total internal reflection microscopy (TIRF) or (confocal) laser-scanning microscopes (LSM) [119]. As described before, picking the correct set of filters is crucial to the experiments, since without suitable ranges of excitation and emission wavelength no signal can be collected at the detector. Speaking of the detector, the most fundamental collector of photons is indeed still to this day the human eye. In a lot of applications and microscopes, eyepieces are used to get an overall impression of certain regimes in the specimen, before more technical advanced detectors such as charge-coupled devices (CCD) fulfill the role of data acquisition.

2. Experimental methods & materials

The upcoming chapter describes the methods and materials used during the course of this thesis. Working with biological samples usually requires elaborate preparation before performing experiments, and therefore cell culture and experimental techniques are an essential part of working in a biophysical laboratory.

The first section is dedicated to the experiments performed with human cervical cancer cells. Here, the basic cell culture techniques used in the course of this thesis, including seeding, bead loading, synchronization, cytoskeletal breakdown, and ER disruption are explained. Then, the used tracer particles and stains with their associated protocols are presented. After this, a more detailed description of the control measurements is given.

Second, the culture and experimental conditions for single particle tracking of Trypanosoma brucei and the concepts of small interfering RNA, as well as corresponding protocols for control experiments are described.

The last section in this chapter is used to describe the different microscopy setups and their characteristics used in this thesis, whether it be for quantum dots SPT experiments or for the observation of T.brucei motion patterns.

2.1. Cell culture and techniques

2.1.1. Seeding and plating of HeLa cells

As a model system for mammalian cells, human cervical cancer cells (**HeLa**) were used. These cells were cultured in Dulbecco's Minimal Essential Medium (DMEM, *Invitrogen*, Carlsbad, CA) with phenol red, supplemented with 10% bovine calf serum (BCS, *Biochrom*, Holliston, MA) and 1% penicillin/streptavidin (*ThermoFisher/Gibco*, Waltham, MA), in the following called D10. The phenol red in cell culture medium is used as an acidity detector, since it changes color from red to a more orange color when pH values change from neutral to acidic. The antibiotics penicillin and streptomycin (streptavidin) are used to prevent bacterial contamination of cell cultures due to their effective combined action against gram-positive and gram-negative bacteria. The cells were incubated in Corning tissue-culture treated culture dishes at 37 °C in 5% CO_2 atmosphere until a confluence of $\approx 70-80\%$ was reached. This was usually achieved every 2-3 days when cells were splitted in a 1:5 ratio. Cells in culture tend to show different behavior, if they are used to shortly after they were thawed or when they are to old [121]. Therefore, only passages 6 to 18 were used in experiments.

Prior to plating of the cells, dishes were coated with 0.5% matrigel matrix with protein concentrations of $c = (8-12)^{\mathrm{mg}}/_{\mathrm{ml}}$ (*Corning Life Science*, New York, NY). To achieve good results, 225 µl matrix was diluted in 45 ml Opti-MEM (*ThermoFisher/Gibco*, Waltham, MA) using frozen pipette tips. A sufficient amount of this solution (e.g. 300 µl per 35 mm diameter dish) was added and the dish with matrigel matrix was incubated for 25 min at 37 °C. Afterwards the supernatant was aspirated and dishes were ready for plating.

Cells were plated on different dishes, depending on the microscope employed for imaging. If the microscope had an incubation chamber (heat box) that covered the whole sample holder with sample, objective and stage, 35 mm µ-Dishes® with high glass bottom (170 µm ± 5 µm, #1.5H D263 M sterilized Schott glass, *ibidi*®, Gräfelfing, Germany) were used. In experiments, where temperature control was established directly at the specimen, 35 mm diameter ΔT dishes (*Bioptechs*, Butler, PA) with ITO coating were used. All experiments were performed 36-48 hours after seeding was finished.

2.1.2. Incorporation of tracer particles

Incorporation of tracer particles into living cells without changing neither the cells' fundamental behavior nor the inert tracers properties is a challenging endeavor. Multiple techniques have been prompted, some of which are more promising than others. In the following paragraph, a short overview of techniques with their respective advantages and disadvantages is listed.

The most obvious approach of getting tracers or other rather large particles into the cytoplasm of a living cell is by letting the cell do all the work itself. The process by which a cell internalizes extracellular material is called **endocytosis**. During this process, the material is surrounded by an area of cell membrane, which subsequently is incorporated into the cell, hence forming a vesicle. Endocytosis is grouped into two different processes depending on particles size. Pinocytosis, or cellular drinking, describes the internalization of small volumes or particles smaller than 500 nm, whereas phagocytosis refers to the uptake of particles larger than 500 nm. The latter is often referred to as cellular eating [69]. Since this mechanism is naturally occurring and therefore inherits less stress to the cell, the method seems to be superior. But there is one flaw: During the process of endocytosis, the tracer particle would be engulfed by membrane and therefore it's size as well as the biochemical surface composition would change. Hence, no control over the desired properties is possible.

Another method of tracer particle incorporation is membrane fusing with the aid of a **fusion reagent**. To this end, Fuse-It-beads (*ibidi*®, Gräfelfing, Germany) was used to perform experiments. In principle, the desired tracer is engulfed by the Fuse-It liposomal carrier which fuses with the cell membrane and releases the included cargo directly in the

cytoplasm [122]. Despite this experimentally rather simple approach sounding promising, meaningful results could not be achieved with this reagent, since its own fluorescent tracer resulted in intensive levels of background fluorescence in the experiments.

Electroporation is a technique used in microbiology allowing chemicals, DNA or other drugs to be introduced into the cytoplasm of cells. In this method, an electrical field is applied to the cell in order to increase the permeability of the cell membrane, allowing the tracer particle to enter the cell via passive transport mechanisms. During this process, the surface biochemistry of the inert particle remains the same, thus suppressing unwanted effects. A major disadvantage of the approach is the overall more damaging nature. Only about 50% of cells do not undergo apoptosis after the procedure of electroporation. Another flaw is the passive transport mechanism. Larger tracers or molecules take a long time to diffuse into the cytoplasm of the cell. Therefore, the membrane might already be sealed again.

A more direct method of particle introduction into the cytoplasm is **microinjection**. Here, a glass micropipette is used to penetrate the cell membrane and to inject a liquid substance at a microscopic level. Common microinjectors have inner capillary needle diameters of more than 1 µm, with the outer diameter being even larger, and use an injection pressure of approximatly 0.14 bar [123–125]. Thinner capillaries have to be handmade and thus require more equipment and practice. Hence, the dimensions of the available ready-to-use microinjectors have not been suitable for experiments with HeLa cells, since the cells are too small.

The technique of choice for incorporation of tracer particles into the cytoplasm of cells in the course of this work was **bead loading**, firstly suggested by McNeil & Warder in 1987 [126]. They described and characterized this "exceptionally rapid and simple technique for loading large numbers of cultured cells with large macromolecules" [126]. To this end, cells are grown until they reach a confluency of more than 80%. Afterwards the culture medium is replaced by a thin layer of the cargo to load. Whereas the original publication described the loading process of large molecules, e.g. 150 kDa dextran into cells, quantum dots of $\sim$ 25 nm diameter were used in this work. The *Qdots 655 ITK carboxylated core (CdSe)-shell (ZnS)* quantum dots (*ThermoFisher*, Waltham, MA) were provided as an 8 µM solution in 50 nM borate with a pH of 9.0 in stock. For bead loading experiments, the quantum dot stock was diluted to a working concentration of 1:1000 in phosphate-buffered saline (PBS) with 1% bovine serum albumin (BSA). First, 8 µl quantum dot working solution was used to replace the priorly aspirated culture medium. Afterwards a monolayer of monodisperse glass beads (G4649-100G, *Sigma-Aldrich*, St. Louis, MO) of 100 µm diameter was gently placed on the specimen with the aid of a thin filter membrane attached to the bottom of a carrier, called the bead loader. A sequence of 7-10 subsequent accelerated movements with an amplitude of approximately 4 cm in which the glass bottom

dish eventually touches the surface of the working bench at the end of each repetition had to be performed in order to push the cargo through the cell membrane. After adding culture medium, the cells were incubated another 45 min at 37 °C. Before imaging, the glass beads were washed off gently using PBS and DMEM without phenol red, and a sufficient amount of imaging medium was added to the dish.

2.1.3. Cytoskeletal breakdown

As already mentioned in section 1.3, actin filaments and microtubules are the essential parts of the eukaryotic cytoskeleton. These structures are dynamic in living cells and might give a potential source for ambient active noise in the cytoplasm. In order to study the influences of fluctuations imposed on the system due to non-equilibrium actions of the cytoskeleton and molecular motors on the thermal driven Brownian motion of inert particles inside the cytoplasm, polymerization inhibition of actin filaments and depolymerization of microtubules was performed, respectively.

Actin filament polymerization inhibition was achieved using two different drugs. First, *Cytochalasin D* (CytD) from ThermoFisher (Waltham, MO) was used. This alkaloid produced by specific kinds of molds is a member of the class of mycotoxins. The cell-permeable chemical is a potent inhibitor of actin polymerization [127]. It binds to the barbed end of F-actin filaments, inhibiting both the association and dissociation of subunits. The compound causes the disruption of actin filaments and inhibition of actin polymerization. Cytochalasin D is about 10–fold more effective than cytochalasin B, and does not inhibit monosaccharide transport across cell membranes. CytD is soluble in dimethyl sulfoxide (DMSO) and was stored at a stock concentration of $c_S^{\mathrm{CytD}} = 1\,\mathrm{mM}$. Note that the working concentration of DMSO in live cell experiments should not exceed 1% [128, 129]. Following other reports [127, 130, 131], the working concentration of CytD was reduced to $c_W^{\mathrm{CytD}} = 2\,\mu\mathrm{M}$. To this end, cells were incubated an additional 30 min at 37 °C after bead loading was performed with 500 µl imaging medium that contained 1 µl CytD stock solution, resulting in the desired working concentration.

In contrast to CytD, *Latrunculin A* (LatA) inhibits actin filament polymerization by binding to actin monomers near their nucleotide binding cleft with 1 : 1 stoichiometry. Therfore, it blocks the binding of G-actin monomers to ATP. Since only ATP-bound actin monomers are able to polymerize, the filament cannot be build. Latrunculin A inhibits binding of thymosin β_4 and nucleotide exchange on actin, but does not inhibit binding by profilin or DNase I [132]. It is noteworthy that LatA is 100 times more potent then CytD [130, 133], thus stock- and working concentrations had to be adapted. For experiments, cells were treated with a 0.2% solution of LatA ($c_S^{\mathrm{LatA}} = 100\,\mu\mathrm{M}$) stored in DMSO, diluted in imaging medium resulting in a working concentration of $c_W^{\mathrm{LatA}} = 200\,\mathrm{nM}$ right after bead loading. Subsequently, cells were incubated for another 30 min at 37 °C before imaging.

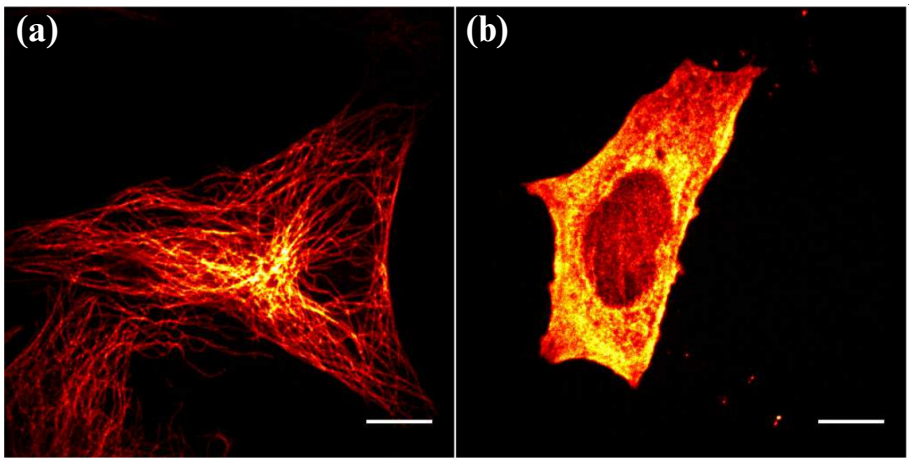

Figure 2.1: Immunostaining of HeLa cells with anti-α-tubulin mouse mAB as a primary antibody. **(a)** Intact microtubule cytoskeleton in untreated cells. MT filaments can be seen spanning the whole cell, with denser packing at the microtubules organization center (brighter area close to nucleus). **(b)** Cells treated with a 10 µM nocodazole solution as described below. The treatment leads to a disruption of microtubule filaments and a hazy cytosolic fluorescence in almost all parts of the cell. Scale bar 10 µm. Figure adapted from [134].

Microtubules depolymerization was performed as described before [134–136] using the drug *nocodazole* (Noc). Branded an anticancer drug, nocodazole has been shown to interfere with the structure and function of microtubules in mitotic cells as well as in interphase. It is thought to bind directly to tubulin causing conformational changes and prohibiting further polymerization of MT [137]. In the course of this work, nocodazole ($\geq$ 99%, tested with thin-layer chromatography (TLC), *Sigma-Aldrich*, St. Louis, MO) provided as powder was used and diluted to a cencentration of 10 mM in DMSO. To achieve these low concentrations, a two step dilution process had to be met. First, 2 mg of nocodazole in powder form had to be diluted in 10 ml DMSO of which another 0.1 ml had to be diluted in 6.6 ml DMSO yet again. This sequence yields the desired stock concentration of 3 µg/ml. After bead loading, culture medium was replaced with imaging medium with 1% Noc, gaining the desired working concentration of 10 µM without exceeding DMSO concentrations as proposed by [128]. Subsequently cells were chilled on ice for 10 min to break the microtubules, followed by a 15 min recovery phase at 37 °C before eventually performing experiments. Fig.2.1 illustrates the effects of nocodazole treatment on HeLa cells. In Fig2.1**(a)** intact microtubules were labeled with anti-α-tubulin mouse monoclonal antibody (*Cell Signaling Technology*, Danvers,MA) as a primary antibody. One can see the dense network spanning almost all parts of the cell. Especially noteworthy is the denser packed microtubule organization center (brighter areas) close to the nucleus. Since there are no microtubules in the nucleus, this organelle appears to be void, with only a few filaments crossing over or under, respectively. Fig.2.1**(b)** shows a HeLa cell after nocodazole treatment as described above. The dense network structure changed to a more

hazy cytosolic fluorescence, since mostly monomers are diluted in the cytoplasm after breakdown. These significant changes illustrate the efficiency of the drug treatment. Note that it was not possible to image the same cell before and after the Noc protocol was performed due to experimental limitations.

2.1.4. Disruption of the endoplasmic reticulum

Next to the cytoskeleton, the endoplasmic reticulum (ER) is an all-encompassing cellular organelle that has been shown to be highly active [72, 134, 136]. In Fig.2.2, fluorescence staining of the ER network was done via Calreticulin-GFP, as described in Sec.2.2. In the left panel, an unperturbed ER network reaching from the perinuclear region to the outer cell periphery is shown. Note that the ER is a three-dimensional structure in the cell, whereas Fig.2.2 only shows a single plane with a thickness of $\Delta z = 0.1\,\mu\text{m}$. To study the influences of the vast ER network and its interconnection with cytoplasmic diffusion properties of tracer particles, ER disruption was done with two different methods.

First, treatment with **filipin III** was performed with a protocol adapted from [138]. Filipin III is a drug that breaks down the ER in living cells [139]. The underlying mechanism is still unclear, but it may be secondary to the cholesterol sequestering action of this compound [138]. Prior to performing experiments, 1 mg filipin III (from *Streptomyces filipinensis*, *Sigma-Aldrich*, St. Louis, MO) provided as powder was resolved in methanol in order to obtain a stock concentration of $10\,^{\text{mg}}/_{\text{ml}}$. Working concentrations in live cell experiments were reduced to $15\,^{\mu\text{g}}/_{\text{ml}}$. The treatment was applied during bead loading

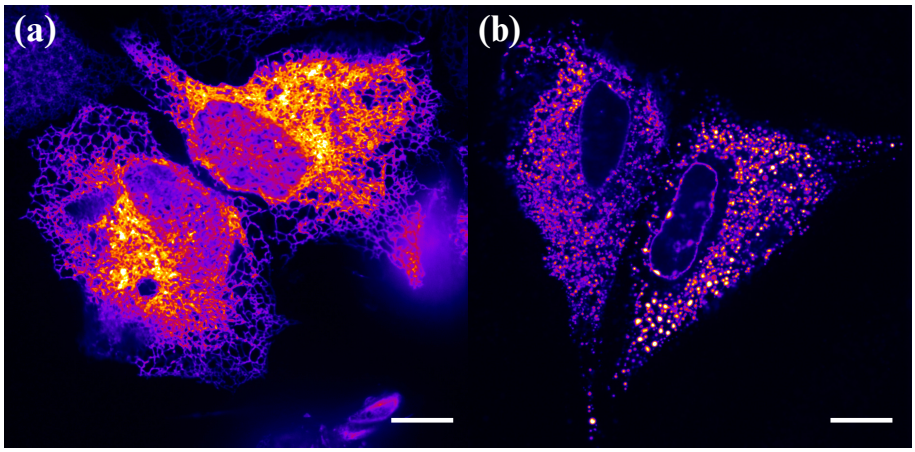

Figure 2.2: Representative fluorescence images of HeLa cells stained with Calreticulin-GFP. **(a)** Intact endoplasmic reticulum in untreated cells. The dense network is present all over the cell, spanning from the perinuclear region to the cell periphery. **(b)** Cells treated with filipin III diluted to $15\,^{\mu\text{g}}/_{\text{ml}}$ in imaging medium as described above. The ER is completely broken with no visible network structure left. ER fragments are accumulated in small clustered without interconnection on larger scales. Scale bars 10 µm.

and imaging. Cells were exposed to filipin at least 30 min prior to and during particle-tracking experiments. Since cells should not be fully confluent during filipin experiments, concentrations while plating cells had to be adapted. Temperatures of 25 °C were not exceeded during experiments. The resulting fragmentation of the ER network was checked by fluorescence imaging of Calreticulin-GFP and was in agreement with previous reports [138]. A representative image of two HeLa cells with fully fragmented ER is shown in Fig.2.2**(b)**.

A second approach of disrupting the ER network was performed using **osmotic stress** or **hypotonic pressure**, as described in [140]. It was shown that swelling of cells results in the formation of polydisperse ER vesicles, i.e. fragmentation of the network structure. To achieve the hypotonic environment in cells, the imaging medium was replaced with highly diluted imaging medium (1:20 in pure water) right after glass beads from the bead loading procedure were washed off. It was shown by King et. al that the integrity of the ER membrane maintained during the hypotonic treatment [140]. Further investigations revealed that the process of ER vesiculation was even reversible (experiments done by Konstantin Speckner and not presented in this thesis). Hence, the assumption that the treatment provides meaningful results is reasonable. An exemplary cell that had undergone hypertonic treatment is shown in Fig2.3. Again, fragmentation of ER's fine tubular network into numerous polydisperse micron sized vesicles is clearly visible.

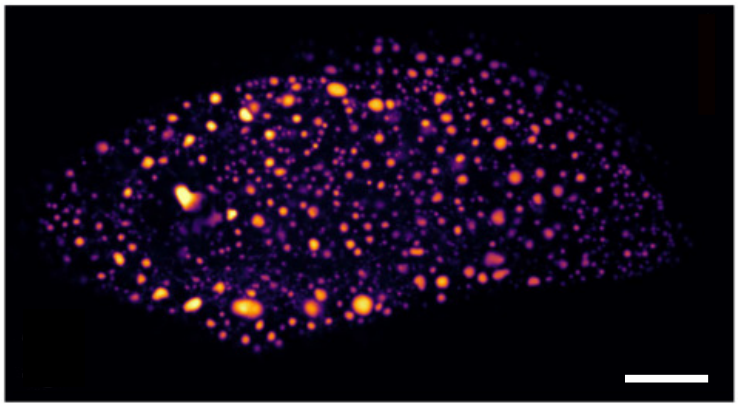

Figure 2.3: Fluorescence image of the vesiculated ER after hypotonic treatment. ER's fine tubular network as seen in Fig2.2 (a) transformed into numerous polydisperse micron-sized vesicles. Scale bar 10 µm.

2.1.5. Cell cycle synchronization

To bring cells in culture at different stages of the cell cycle to the same phase, cell cycles need to be synchronized. This synchronization is vital in biology and biophysics, since it allows for population-wide data collections instead of relying on single-cell experiments. There are two major types of cell cycle synchronization. First, there is physical fractionization, a process by which a population of cells is divided into subpolpulations due to physical characteristics such as cell size, viscoelastic behavior, or density. A second method is a procedure where cells arrest at a cell cycle checkpoint due to the addition of an exogenous substance, called chemical blockage [141]. The main advantage of these techniques is that they do not require removal from cell culture environment. While the latter method is generally more precise, some imperfections might occur nevertheless. These include perturbance of cellular function due to the chemical manipulation and insufficient proportion of synchronized cells.

In the course of this work, an arrest-and-release approach was made that involved treatment with a chemical block and subsequent release by washing off the block as described previously by [14]. To this end, nocodazole (*Sigma-Aldrich*, St. Louis, MO) with a stock concentration of $3\,\mu g/ml$ was used again. As described before, nocodazole is a rapidly-reversible microtubule polymerization inhibitor and therefore it can be used to arrest cells at the spindle assembly checkpoint at metaphase-anaphase transition. The drug blocks the formation of the mitotic spindle, hence the sister chromatids cannot attach and cannot be separated in the dividing cell. Interestingly, cells' interphase metabolism is not disrupted by this and released cells return to normal cell cycle progression [142]. Synchronization of cells was done on the evening before bead loading experiments were performed. Dishes were gently washed with PBS. Afterwards $5\,\mu l$ Noc from stock had to be diluted per $1\,\mu l$ culture medium (D10). Cells were then incubated for $12-18h$ at $37\,°C$ in 5% CO_2 atmosphere overnight. Since microtubules are vital for cellular functions, the sustained use of nocodazole potentially perturbs these mechanisms and eventually causes apoptosis and cell death, if nocodazole exposure time exceeds 18 hours. Before imaging the next morning, nocodazole had to be washed off gently two times using PBS. When performing synchronization, one has to keep in mind that cells tend to round up and might reduce the number of focal adhesion points with the substrate resulting in a less adherent population. Hence, using strong vacuum pumps for aspiration of medium as well as strong flows while washing the cells are not recommended. Thus, rather gentle addition and removal of fluids is advisable.

2.2. Tracers and fluorescent labels

2.2.1. Quantum dots

In the course of this work, quantum dots were used as tracer particles in bead loading experiments as described in 2.1.2. To this end, Qdot® 655 ITK™ (Innovator's Tool Kit) carboxyl quantum dots (*ThermoFisher*, Waltham, MA) were used. This nanometer-scale crystals are made of a semiconductor material (CdSe), which are shelled with an additional semiconductor layer (ZnS) to improve their chemical and optical properties [117]. A transmission electron microscopy image of the nanoparticles at a magnification of 200,000 times is shown in Fig2.4**(a)**. The material has a narrow, symmetric emission band with a maximum at $\lambda = 655\,\text{nm}$ and a broad excitation spectrum reaching from UV to visible light as depicted in Fig.1.10. The qdots are further coated with a polymer layer, facilitating dispersion in aqueous solution while retaining their optical properties, thus allowing experiments in cellular environments. The size of these tracers is comparable to larger macromolecules' hydrodynamic radii [143] as seen in Fig2.4(b). Therefore, they are well-suited candidates for measurements of cytoplasmic diffusion. The polymer coating has -COO surface groups, allowing modifications such as macromolecular attachments. In this work, the quantum dots' surface was not altered to avoid specific binding.

Quantum dots were provided as a 8 µM solution in 50 mM borate buffer. After sonication of the quantum dots' stock vial for 5 min, 1 µl quantum dots stock solution was diluted in 1 ml PBS with 1% BSA. Since BSA is negatively charged, it binds salts, fatty acids, hormones and vitamins. Therefore, it reduces unspecific binding of molecules to the quantum dots surface coating on the one hand, and counteracts quantum dot accumulation on the other hand.

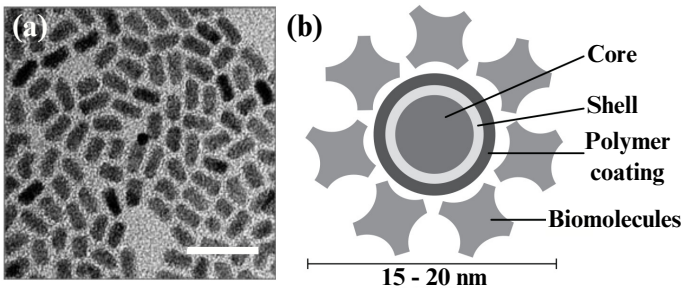

Figure 2.4: **(a)** Transmission electron microscopy (TEM) image of core-shell Qdot® nanoparticles at 200,000x magnification. The particles seem to be monodisperse and tend to have a more elongated oval like shape. Scale bar 20 nm. **(b)** Schematic representation of the overall structure of a Quantum dot conjugate. The layers represent the distinct structural elements and are roughly to scale. Figure adapted from [117].

2.2.2. Fluorescent dyes: labeling and transfection

In order to visualize intracellular compounds or organelles, fluorescent labeling is – next to ordinary wide field light microscopy – the go-to technique in the life sciences.

DNA staining in interphase and mitotic cells was achieved using the *bisBenzimide H 33342 trihydrochloride* (**Hoechst 33342**) blue fluorescent dye (*ThermoFisher*, Waltham, MA). The dye is excited at approximately 350 nm and its emission maximum is in the cyan-blue wavelength range around 461 nm, thus it can be excited with standard mercury- or xenon-arc lamps, or with the aid of UV lasers. Hoechst is cell-permeable, hence it can be easily introduced into the cytoplasm and even nucleoplasm by means of addition to culture medium. In the nucleus, it binds preferentially to the minor groove of adenine-thymine regions of DNA. In application, the dyes stock concentration was 10 $^{mg}/_{ml}$ in water or DMSO. The dye is stable in aqueous solution at low temperatures ($2-6\,°C$) for at least 6 month when protected from light, but should be stored frozen for long term storage. The already plated and otherwise treated cells were stained with 1% Hoechst 33342 at stock concentration in imaging medium without phenol red for 30 min at 37 °C. Afterwards the cells are washed to remove remaining unbound dye, thus reducing background fluorescence in experiments [144]. A time series of HeLa cells stained with Hoechst is shown in Sec.1.3 Fig.1.6.

A much more elaborate method of labeling organelles in living or fixed cells is by transfection. In general, transfection is the process of artificially introducing nucleic acids – such as DNA or RNA – with methods other than viral infection [145–148]. The introduction of foreign nucleic acids by means of various biological, chemical, or physical mechanisms usually results in changes of cellular properties, whether or not these changes are beneficial for studying the cell depends on the used protocol and introduced nucleic acids. If done right, transfection reveals interesting insights into gene function and protein expression and is a powerful tool in microbiology and biophysics.
The two main purposes of transfection are to specifically enhance or inhibit gene expression, or to produce recombinant proteins. During this work, transient chemical transfection was utilized to create a recombinant protein in human cells that retains in the lumen of the ER and is labeled with an additional fluorescent protein. *Calreticulin-GFP* (**CRT-GFP**) was generated by Peter Steyger (plasmid #80978, *Addgene*, Watertown, MA) using GFP with the addition of KDEL[2] by polymerase chain reaction (PCR) using pEGFP-N2 (*Takara-Bio*, Kyoto, J) as a template, digested with NotL/Xbal and subcloned into pcDNA3.1 [149]. Transfection was done using the lipofection technique. In this method genetic material is injected into the cell by means of liposomes – small phospholipid bilayer bound vesicles – that can easily merge with the cell membrane. To this end, *Lipofectamine™ 3000 reagent*

[2]Sorting of resident soluble proteins retained in the lumen of the ER is dependent on a C-terminal tetrapeptide signal. In mammalian cells, this is usually the KDEL (Lys-Asp-Glu-Leu) protein.

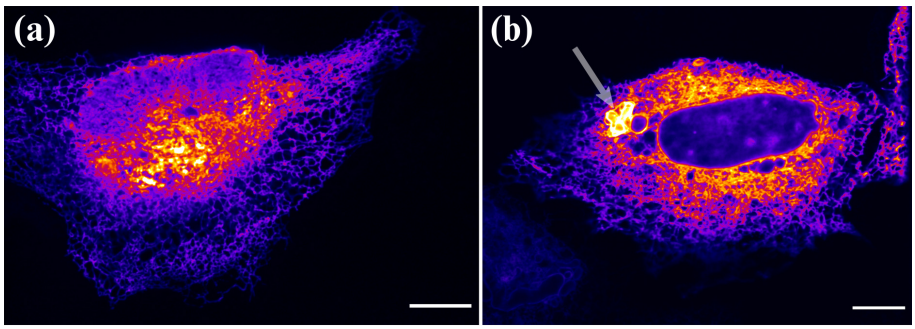

Figure 2.5: Representative fluorescence image of HeLa cells trancfected with **(a)** CRT-GFP and **(b)** CNX-GFP. Calreticulin labeled ER lumen shows the anticipated phenotype, whereas Calnexin labeling showed occasional larger non-tubular, bubble like structures of the ER in the perinuclear region reminiscent of disrupted network, indicated by an arrow. Scale bar 10 µm.

(*ThermoFisher*, Waltham, MA) was used to perform lipofection on $70-90\%$ confluent cells. Best transfection efficiencies are achieved, when cells are analyzed after a $2-4$ days period of incubation at $37\,^{\circ}\mathrm{C}$ in 5% CO_2 atmosphere [145]. Visualization of CRT-GFP was done using an excitation wavelength $\lambda_{\mathrm{ex}} = 491\,\mathrm{nm}$ and GFP-suitable emission filters in the range of $(525 \pm 25)\,\mathrm{nm}$.
Another possible ER marker used during the course of this work was *mPA-GFP-Calnexin-N-14* (**CNX-GFP**, plasmid #57122, *Addgene*, Watertown, MA). Representative fluorescent images of CRT-GFP as well as CNX-GFP labeled ER are shown in Fig.2.5.

2.3. Quantum dot control experiments

Validating and interpreting data acquired in experiments is usually a difficult task, especially when researching new environments, using new techniques, or a combination of both. Therefore, assumptions made about the investigated systems have to be checked using appropriate controls. This requires challenging characteristics, beginning with the most fundamental ones and eventually leading to more elaborate approaches. In this thesis, control experiments regarding quantum dots SPT experiments were addressed using different approaches.

Since the cytoplasm of cells is often described as a crowded aqueous fluid [11, 15, 55, 69, 87], an artificial environment mimicking its viscoelastic properties was synthesized. To this end two different approaches were made.
First a viscose sucrose solution with a dynamic viscosity η higher than water was made. Since $\eta_{\mathrm{H_2O}} = 1\,\mathrm{mPa\,s}$ at $T = 20\,^{\circ}\mathrm{C}$, the viscosity of the sucrose solution should at least be one order of magnitude higher. To achieve this, 1.5 g sucrose ($C_{12}H_{22}O_{11}$, LOT# BCBZ5586) was diluted in 1 ml *Ultra Pure Water* (LOT# 1943440) both from *Sigma-Aldrich* (St. Louis, MO), hence creating a 60% per weight sucrose solution with a viscosity

$\eta_{\mathrm{Suc}} \approx 50\,\mathrm{mPa\,s}$ at $T = 25\,^{\circ}\mathrm{C}$ [150]. Mixing of the solution was achieved by thermoshaking the mixture for roughly 4 hours at 40 °C. After this 4 µl quantum dot stock solution was diluted in 196 µl sucrose solution, followed by 15 min on a bench rocker 3D nutating shaker. In a second approach an environment with even higher dynamic viscosity was examined. To this end quantum dots were diluted in a (1:50) ratio in pure *glycerol BioUltra* for molecular biology (LOT# BCBW1105, *Sigma-Aldrich*, St. Louis, MO) yielding a viscosity of $\eta_{\mathrm{Gly}} \approx 1\,\mathrm{Pa\,s}$ at $T = 25\,^{\circ}\mathrm{C}$, hence, an increase by three orders of magnitude compared to water.

Following other protocols, DMSO was used in this work as an important solvent that can solubilize a wide variety of otherwise poorly soluble molecules. This property has lead to an ubiquitous use and widespread applications in combination with its apparent low toxicity [151]. On the other hand, it was shown that DMSO in higher concentrations $> 10\%$ may lead to apoptosis, due to cell membrane pore formation [151]. Overall it is not advised to use DMSO in concentrations larger than 1% when performing live cell experiments [128, 129]. In order to verify that non of the observed changes of cell properties and diffusion characteristics presented in this thesis are induced by to high DMSO concentrations, control measurements with DMSO concentrations tailored to fit experimental conditions were performed. To this end, dishes were prepared as described in Sec.2.1.1 and washed one time using prewarmed PBS. Subsequently 500 µl imaging medium with 0.2% DMSO was added, followed by a 30 min incubation at 37 °C, thus following the ordinary protocol without any use of additional drugs except DMSO. Eventually cells were imaged as described in Sec.2.5.

2.4. Trypanosoma brucei subspecies brucei

2.4.1. T.brucei culture

As mentioned before, *T.brucei* is a kinetoplastid protozoan parasite and is the causative agent of African trypanosomiasis, which is transmitted to both humans and livestock through the bite the tsetse fly. The flies inject the infective stage (metacyclic trypomastigotes) from their salivary glands into the blood and lymphatic fluid of the host, where they undergo differentiation and enter the central nervous system by evading the host immune system through the use of antigenic variation of their surface glycoprotein coat [98, 102]. For single particle tracking experiments on kinetoplastea, the *T.brucei* subspecies brucei, strain *Lister 427 29-13 (TetR T7RNAP)* as a procyclic form cell line that expresses the T7 RNA polymerase and the tetracycline repressor genes, were used. The strain Lister 427 was derived by sequential stable transfection of procyclic form of wild-type *T.brucei*. The parent strain is a virulent lab strain isolated in 1960 from a sheep in Uganda and transferred to the Lister Institute in London in 1961. The reagent was obtained through BEI

Resources, NIAID, NIH: *Trypanosoma brucei*, Strain Lister 427 29-13 (TetR T7RNAP), #42012 [152].

Maintenance and clonation of *T.brucei* mutants used in the course of this work was done by the group of Prof. Klaus Ehrsfeld (Dept. Genetics, UBT). The basic procedure is nevertheless briefly explained here. First, the culture should be agitated at or near peak density. Next, $0.5 - 1$ ml of culture has to be transferred aseptically into a new T-25 tissue culture flask containing 10 ml SDM-79 medium (*Life Technologies*, Inchinnan, UK) adjusted to contain 10% (v/v) heat-inactivated BCS and 15 µg/ml G418 and 50 µg/ml hygromycin. Incubation of the culture has to be done at 27 °C with the cap screwed on tightly. Transfer should be done every 3 to 7 days, empirically determined on the quantity of the inoculum. In the culture used here, transfer was done every 3 or 4 days, when the population density had exceeded $\rho = 3{\cdot}10^6 \mathrm{ml}^{-1}$. Cell growth was measured using a CASY cell counter (*Roche Innovatis AG*, Bielefeld, Germany).

For imaging *T.brucei* were plated on Corning™ rectangular (22×40 mm) borosilicate cover glass with a thickness of $0.13 - 0.17$ mm (*ThermoFisher*, Waltham, MA). The cover glass was attached to the non-gridded section of a Thoma chamber ($0.0025\,\mathrm{mm}^2$) hemocytometer to provide a distinct z-spacing of ≈ 100 µm, thus allowing enough space for the kinetoplastea to not be squeezed, but still sufficiently tight space for them to not wander off into another focal plane while imaging. The whole setup chamber was turned up side down during imaging, hence allowing observation through the thin coverglass. Since *T.brucei* are highly mobile even at lower temperatures compared to mammalian cell lines, all experiments were done without any heating, i.e. at a temperature of approximately $T = 24$ °C.

2.4.2. Small interfering RNA

The presumably essential role of tubulin-tyrosine ligase like (TTLL) and other proteins in the transient dynamics of subpellicular cytoskeleton in *T.brucei* and thus its influence on motility and mobility has already been introduced in Sec.1.4. One way of studying the role of these proteins, is silencing them. Hence, the translation of their respective mRNA into amino acids and later proteins has to be suppressed. In the following paragraphs a brief introduction in how these changes are implemented in kinetoplastids is given.

The technique of choice for specific protein suppression of a population of individual specimen is the so called RNA interference with **small interfering ribonucleic acids (siRNA)**. These $20 - 25$ base pair long class of double-stranded (ds) non-coding RNA molecules interferes with the expression of specific genes with complementary nucleotide sequences by degrading mRNA after transcription and hence preventing translation [69]. The mechanism by which small interfering RNA silences genes through repression of transcription works as follows:

1. A dicer (endoribonuclease) cuts long dsRNA by cleaving into smaller dsRNA which may now enter the cell.
2. Once inside the cell, the siRNA gets incorporated into other proteins to form the RNA-induced silencing complex (RISC).
3. When part of the RISC, the still double-stranded RNA is unwound to form single-stranded siRNA.
4. Since the strand with a base pairing at the 5' end is less stable, it remains in the RISC and can now start scanning for complementary mRNA.
5. If an appropriate mRNA is found, the RISC binds it and cleaves it, eventually slicing it up.
6. The mRNA is recognized as abnormal by the cell which causes degradation and in turn prevents translation of the specific mRNA into proteins.

By means of stable transfection, mutant populations can be cultured. These subpopulations have one specific gene each that can be depleted when the RNA interference is induced by a specific drug. Hence, not yet induced mutants should show similar behavior as individuals of the wild type (WT) population. In this work, two different mutant subpopulations were investigated that all target the TTLL protein pathway, yielding a total of 6 conditions (not induced/induced or $\pm$ for short) for evaluation. In the following paragraph, a more detailed description on the generation of the two specific mutant cell lines is given.

Generation of TbTTLL6A- and TbTTLL12B-RNAi cell lines The RNAi constructs, *pALC14-TbTTLL6A* and *pALC14-TbTTLL12B* were created using the stem loop vector *pALC14*, which allows the doxycycline inducible production of hairpin dsRNA with the use of a single doxycyclin-inducible procyclin promotor [153]. DNA sequences for *TbTTLL6A* (Tb927.3.5380) and *TbTTLL12B* (Tb927.11.2420) were retrieved from TriTrypDB. For *pALC14-TbTTLL6A* a 266 base pair DNA fragment was amplified using the sense primer $TbTTLL6A_{for}$ and the anti-sense primer $TbTTLL6A_{rev}$. For *pALC14-TbTTLL12B* a 180 base pair fragment was amplified using the sense primer $TbTTLL12B\text{-RNAi}_{for}$ and the anti-sense primer $TbTTLL12B_{rev}$. To avoid off-target effects, suitable RNAi fragments were selected using the RNAit software [154]. The PCR fragments were cloned into the RNAi vector using the restriction sites *HindIII*, *XbaI*, *XhoI* and *BamHI*. The final constructs were linearized with NotI and transfected into procyclic cells by electroporation in an Amaxa Nucleofector II (Lonza, Germany) [155]. Transformants were selected with 1 µg/ml puromycin and eventually RNAi was induced with 1 µg/ml doxycycline.

2.4.3. Poly-L-lysine coating

Trypanosoma brucei are highly mobile with step velocities of some micrometer per second. In order to determine the dynamic offset for particle tracking of parasites and therefore getting a reference point for non-motile *T.brucei*, live procyclic cells were settles onto *poly-L-lysine* coated cover glass. *Poly-L-lysine* is a synthetic amino acid chain that is positively charged having one hydrobromide per unit of lysine. *Poly-L-lysine* is widely used as a coating to enhance cell attachment and adhesion to both plasticware and glass surfaces.

The 0.1 $^{\mathrm{mg}}/_{\mathrm{ml}}$ *poly-L-lysine* stock solution (*Sigma-Aldrich*, St. Louis, MO) was thawed at room temperature and diluted to a concentration of 50 $^{\mu\mathrm{g}}/_{\mathrm{ml}}$ with sterile water. Surfaces were coated with sufficient a volume and allowed to sit overnight at room temperature. Before settling parasites, residual *poly-L-lysine* solution was aspirated and the surface was rinsed with sterile water. All other experimental conditions were kept as described earlier.

2.5. Microscopy and image acquisition

In the following section, all utilized microscope setups, as well as image acquisition conditions are explained in detail. Since measurements were done on several setups with multiple distinct features, the order of the following listing will be:
First, microscopes and image acquisition conditions used to acquire data regarding quantum dot tracking in human cervical cancer cells, including TIRF-microscopy in wide field mode measured at the Colorado State University (Fort Collins, CO), laser scanning microscopy, and wide field fluorescent microscopy in chronological order.
Second, the bright field illumination data acquisition for T.brucei is specified.

2.5.1. Acquisition of quantum dot SPT data

TIRF in wide-field mode The following data acquisition was done in close cooperation with X. Xu (Department of Electrical and Computer Engineering) and Prof. Dr. Krapf (School of Biomedical Engineering) at Colorado State University (Fort Collins, CO).
Images were acquired using a Nikon NIS-Elements 4.51 software in a custom-build microscope equipped with an Olympus PlanApo 100× objective with a numerical aperture (NA) of 1.45 and a CRISP ASI autofocus system [156]. Optical aberrations of the imaging system were corrected using a MicAO 3DSR adaptive optics system from Imagine Optics (Orsay, France) inserted into the emission pathway between the microscope and the electron multiplying CCD (EMCCD) camera [157]. The sample temperature was kept at $T = 37\,^{\circ}\mathrm{C}$ using a Bioptechs stage heater in combination with specially designed ΔT dishes (*Bioptechs*, Butler, PA) with ITO coating. Quantum dots were excited using a 100 mW laser at wavelength $\lambda_{\mathrm{ex}} = 561\,\mathrm{nm}$ (OBIS 561 nm LS 100 mW, Coherent, Santa Clara, CA)

under continuous illumination. For excitation, an optical filter with ND = 1 was used. Since the utilized setup is primarily used to perform total internal reflection microscopy, but this feature was not desired in this particular study, an incident angle below the critical angle was chosen to provide a sufficient penetration depth of multiple micrometers. Emission of the quantum dots was collected through an appropriate bandpass filter (Di01-R488/561-25x36 lasers BrightLine® dual-edge laser dichroic beamsplitter, *Semrock*, Tulsa, OK). Hoechst excitation was done using a 405 nm diode-laser with intensity adjusted to 5 mW. For bright field (BF) illumination, an Intensilight wide-field light source was used. Time series images of quantum dots fluctuations were acquired in a water-cooled back-illuminated EMCCD camera (iXon DU-888, *Andor*, Belfast, UK) operated at −85 °C at a rate of 20 $^{\text{frames}}/_{\text{second}}$ in interphase cells, and at a rate of 10 $^{\text{frames}}/_{\text{second}}$ in all other experimental conditions to compensate for a worse SNR due to the treatments. The camera gain was set to 100 and a total of 2050 frames were recorded. Both, fluorescence images of chromatides stained with Hoechst and BF images were acquired prior to and right after time series of quantum dots images with 100 ms exposure time and respective gains of 40 and 100 each.

Confocal laser scanning microscopy In addition to the aforementioned image acquisition with a total internal reflection microscope in wide-field mode, imaging was performed with a *Leica SP5 confocal laser scanning microscope*, hereinafter referred to as **SP5** or **cLSM** from Leica Microsystems (Wetzlar, Germany). In the setup, a 63×/1.4 NA oil immersion objective (*HCX Pl APO lambda blue* 63×*/1.4 NA oil IMM*, Leica Microsystems) was used. Control measurements and osmotic stress experiments were carried out at 37 °C using a custom-build incubator chamber that covered the sample as well as the stage and objective. ER disruption experiments using filipin III were done without the use of a heating box, i.e. at room temperature. Samples were illuminated at 476 nm using a 1 mW laser with its power tuned to 30% and emission was detected in the range 630 − 680 nm with the smart gain set to 750 V. Image acquisition was designed to meet the Nyquist criterion and respecting the diffraction limit. The pinhole was set to one Airy unit (equivalent to 91.3 µm with the used experimental conditions) throughout, i.e. every pixel in an image corresponds to a diffraction-limited volume. Images of quantum dots were taken with 256 × 256 pixels with a pixel size of 160.2 nm at a 6× zoom factor resulting in an image size of $(41 \times 41)\mu m^2$. Therefore, multiple cells could be observed at once. Bidirectional scanning speed was set to 1400 Hz resulting in a pixel dwell time of 1.53 µs. Thus, a frame time of 100 ms could be achieved, matching exposure times of previously performed experiments. A total of 2050 frames per stack were acquired, hence the imaging was comparable to the previous camera-based measurements at the TIRF microscope in wide-field mode.

Wide-field fluorescence microscope In an attempt to replicate bead loading data with camera-based acquisition techniques, measurements were done at wide-field fluorescence microscope in cooperation with the Experimental Physics VI lab (Biological Physics, UBT, Prof. Dr. Kress).
Images were acquired at a custom-built setup with a *Nikon Eclipse Ti-E* microscope base equipped with a 60×/1.27 NA water immersion objective (*CFI Plan Apochromat IR* 60×*C WI*, *Nikon Instruments Europe B.V.*, Amsterdam, Netherlands) and custom-made incubator chamber. Experiments with filipin III were done at room temperature, whereas control experiments were carried out at 37 °C. For excitation of quantum dots, an *Intensilight C-HGFI precentered fiber illuminator* and appropriate filters (ND=1 and *GFP-LP*, excitation: $473 - 497$ nm, emission: $505 - 950$ nm) both from *Nikon* (Tokyo, Japan) were used. Time series with 2050 images per stack were acquired in a TE (Peltier)-cooled EMCCD camera (Andor Luca R DL-640M-VP, *Andor*, Belfast, UK) with image size reduced to 256×256 pixel (pixel size 133 nm) and exposure times of single images set to $\tau_{ex} = 60$ ms to achieve maximal frame rates of 10 Hz. Bright field images were acquired prior to and right after each time series with an exposure time of 300 ms and the EM gain set to 2, whereas the EM gain was set to 240 during quantum dot imaging.

2.5.2. Observation of *T.brucei* motion patterns

Time-resolved bright-field illumination imaging of individual trypanosomes was performed at room temperature using a *Leica DMI 6000* microscope (*Leica Microsystems*, Wetzlar, Germany). At the beginning of each measurement day, the *Köhler illumination* was adjusted using a *Convolaria* test sample. For optimal image quality, intensity of BF illumination was set to 75, the aperture blind was set 6 and the transition light field blind was set to 8. Images were acquired with a monochrome digital CCD camera *DFC360FX* using a 20×/0.70 NA IMM air immersion objective. Due to the rather small magnification, compared to the aforementioned objectives, a large field of view (448.9×335.2 µm) was provided. The setup was controlled by the Leica Application Suite X (LAS X, 3.6.0.20104). Imaging was performed at a frequency of ten frames per second over a total time period of 3 min, yielding 1800 frames, each with a camera exposure time of 5 ms. To achieve a representative sampling of the available motion patterns, at least three different regions were selected for each condition in each of which at least five individuals were monitored. Samples were imaged a maximum of 30 min after preparation to prevent ageing processes that could perturb the motion patterns.

3. Evaluation methods

In the following chapter, the methods used for evaluation of the acquired data will be described in more detail. During the course of this thesis, a lot of multidimensional data have been carefully collected. Most of the data are time series of images that contain the spatial and temporal evolution of intensity profiles of tracers of any kind. These tracers are either photon emitting quantum dots or absorption profiles of T.brucei illuminated with a bright field light source. In a first step, the data, i.e. the trajectories, have to be extracted from the stacks. A detailed description on how this is done in this work is given in the section on single particle tracking.
After the trajectories are extracted from the 2D image time series, the motion behavior of the tracers is evaluated. Beginning with a more basic approach, the time-averaged mean squared displacement (TA-MSD) is calculated, from which the anomaly exponents and the generalized transport coefficients can be derived. Since time series were acquired with precise temporal resolution, velocities can be assigned to each step and therefore the velocity autocorrelation function (VACF) is a meaningful quantity to look at.

Since the two studied systems show different motion patterns, further methods of evaluation had to be adjusted. Therefore, more elaborate evaluation methods are discussed in more detail, first for quantities extracted from quantum dot SPT experiments in human cervical cancer cells, and second regarding measurements with kinetoplastids.

3.1. Single particle tracking

Understanding the complex interactions between a variety of different cellular components and deciphering their presumably highly heterogeneous environment in time and space is a challenging task. Thus, having access to monitoring the mobility of the components that underlie the dynamic organization of the cell is crucial, since important cues for the understanding of living systems on a microscopic basic can be found with insights in the subcellular environment. Central to the advances of revealing the physical mechanisms underlying the enormous complexity of living cells is the development of least-invasive techniques capable of visualizing dynamic processes with high sensitivity and spatiotemporal resolution [158]. One of the most fundamental techniques for gathering dynamic data with high possible spatiotemporal resolution is single particle tracking. **SPT** describes the observation of the motion of individual tracer particles within a medium. Whether or not the tracked particles are biological molecules inherent to the cell and tagged with a fluorescent tracer, or exogenous particles introduced through least-invasive means, the underlying principles of SPT stay the same. A schematic representation of the workflow while performing SPT experiments is given in Fig.3.1.

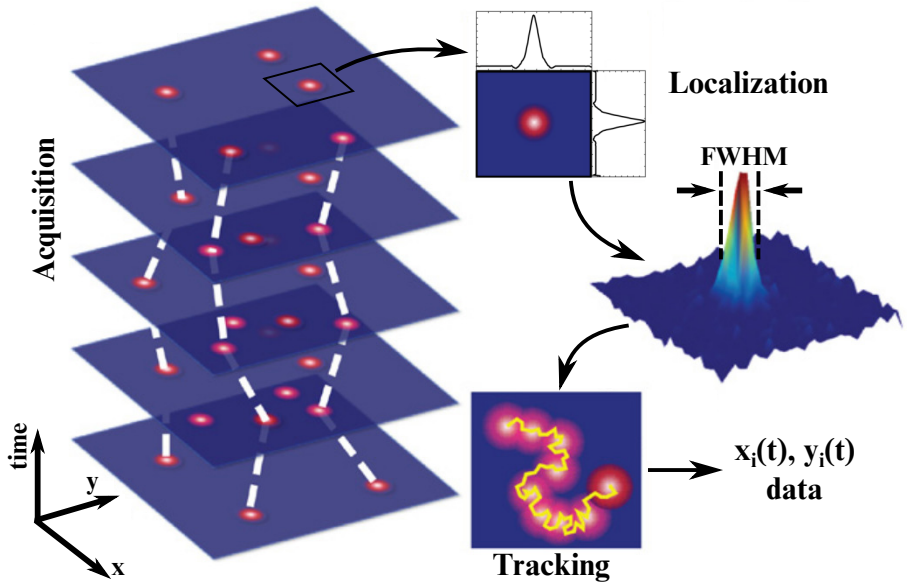

Figure 3.1: Schematic representation of a single particle tracking experiment. First, acquisation of image time stacks as described in Sec.2.5 has to be done. Red spots imply tracer positions in every frame at time t_j. Next, localization of tracer particle i at the respective time has to be done. The accuracy of spatial positions is ultimatly dependent on the full width at half maximum (FWHM) of the point spread function (PSF), the number of photons collected from the emitter, and the overall level of other noise sources during the experiment. After spatial localization at every time t_j, positions have to be linked to generate the track of each particle. Eventually trajectories have to be extracted. Figure adapted from [158].

In a first step, image time stacks have to be acquired as described before in Sec.2.5. In essence, an image of a single point object, e.g. a quantum dot, acquired with an optical microscope will be collected at a detector as a diffraction pattern with the shape of concentric rings of decreasing intensity as a function of distance to the center. Since the central disk - called the Airy disk - contains most intensity, it is most interesting for extraction of information. Its profile can be approximated according to equation Eq.3.1 with a 2D Gaussian such that I_0 is the central intensity and σ is the standard deviation of the intensity profile connected to the point spread function (PSF) of the microscope.

$$I(x,y) \approx I_0 \exp\left\{-\frac{(x-x_0)^2}{2\sigma^2}\right\} \exp\left\{-\frac{(y-y_0)^2}{2\sigma^2}\right\} \tag{3.1}$$

In microscopy experiments, two objects cannot be resolved individually if their mutual distance is smaller than the full width at half maximum (FWHM) of each intensity profile. Hence,

$$\mathrm{FWHM} = \sigma\sqrt{8 \cdot \log(2)} \approx \lambda/2\mathrm{NA} \tag{3.2}$$

where λ is the wavelength of the excitation light and NA is the numerical aperture of the

objective. Using the inputs given in Sec.2.5, it was calculated that two particles with a distance of $\Delta r \gtrapprox 210\,\mathrm{nm}$ can be resolved as individuals. For distances larger than the FWHM, two objects appear to be distinguishable and their centroid position can be fitted using Eq.3.1. The maximum position of this 2D Gaussian can be derived with higher precision compared to the spatial resolution set by experimental restrictions. In fact, a spatial precision of just a few nanometer can be achieved. In order to get subpixel precision, the tracer particle density has to be sparse enough so that every point of interest can be investigated separately.

After repeating the localization step for each individual particle i in every single frame t_j with temporal distance Δt, linking of the respective positions has to be done. In systems with ultra-low particle densities, connections between consecutive positions, i.e. finding the position $\mathbf{r}(t_{j+1})^{(i)}$ can simply be made by searching for the nearest neighbor to position $\mathbf{r}(t_j)^{(i)}$ at time $t_j + \Delta t$. High particle densities lead to the creation of combinatorial problems, which in turn my lead to tracking artifacts. Therefore, more elaborate linking algorithms have to be used. These include: correlation tracker [159], energy minimization [160] or linear assignment problem algorithms [161]. For more detailed insights see [158, 162].

In a last step, the data are extracted as trajectories of each individual particle and are now ready to be evaluated.

The usefulness of SPT trajectories depends on spatial localization precision, the accuracy of finding centroid positions, the maximum temporal resolution due to the setup, and the experimental observation time. The precision of localization is generally determined by the number of photons collected to form the image which is fluctuating. These variations in emitted as well detected photons are due to stochastic emission, background noise, dark counts, pixalation and detector noise, and autofluorescence of the sample. The result of these uncertainties is the so-called **static localization error**. The accuracy of the centroid positions depends on the detector settings, as well as the algorithm used to fit the assumed curve to the data. Since every experiment has physical limitations in time resolution, it is only possible to track motion down to a certain minimal limit. Fluctuations that occur between time frames will never be observable, hence a **dynamic localization error** will be present in measurements. More data points in a trajectory are equivalent to more information, thus sufficient experimental observation time is crucial.

The explicit settings used to extract SPT trajectories are listed in the following section.

Quantum dot in HeLa cells Trajectories were extracted from image stacks using the TrackMate plugin in FIJI introduced by Tinevez et. al [162]. As an input for TrackMate, the blob diameter - a threshold diameter connected to the FWHM - of Qdots was estimated via the intensity profiles of 30 quantum dots immobilized on the coverslip, yielding an

average of 3.2 ± 0.5 pixels for the FWHM of the point spread function. Localization of particle positions was performed using the *Laplacian-of-Gaussian* algorithm with a blob diameter set to 4 pixels. The minimal threshold was chosen to be higher than 200, thus excluding background noise and unwanted fluctuations. A median filter was used to further suppress noise and therefore enhance SNR. Sub-pixel localization – executed with Gaussian fits – was switched on to provide higher particle position resolution. No additional filters were applied to the detected spots. Identified particle positions were linked using the *simple linear assignment problem* (LAP) tracker adapted from Jaqaman et. al [161]. In the algorithm the maximum linking distance as well as the maximum gap-closing distance was set to 2 pixels, to ensure that only positions belonging to the same quantum dot were linked. The maximum frame gap, i.e. the maximum time a position was still assigned to a trajectory even if no suitable particle was detected in its previous frame, was set to 2 and the maximum number of gaps was set to $n_g \leq 5$. This was done to avoid artificial jumps in the tracks but still connect trajectories of quantum dots that were potentially blinking. Only tracks with a minimum frame count of $N \geq 50$ were regarded subsequently, therefore fulfilling the criterion of a sufficiently long observation times. Spot statistics and tracks were exported from TrackMate as `.csv` and `.xml` files, respectively. Afterwards trajectories were converted to `ASCII` files in `MATLAB` for processing and handling. All subsequent statistical analysis of trajectories with $N \geq 50$ positions and time lag Δt between successive frames was performed using custom-written `MATLAB` codes that have been checked for proper function via fBM simulation data.

Tracking of *T.brucei* motion patterns Data collected for observation of motion patterns of kinotplastids do not fulfill classic criteria of SPT data, like diffraction-limited detection signals from point-like emitters, or even any photon emitting tracer at all. In fact, the raw data collected in these experiments are absorption profiles of *T.brucei* using bright-field microscopy. Hence, the data could not be tracked according to the protocol described above for quantum dots, but rather a new approach had to be adapted. Despite the unconventional data, tracking was feasible with the aid of prior image processing. To this end, the open source image manipulation and processing bundle FIJI for ImageJ was used again.

First of all, intensity values of all images were inverted before further analysis. This was done due to the empirically found fact that the used TrackMate algorithms are better at finding brighter peaks on darker background. For background correction, the mean of a region without any *trypanosome* traces was determined in every image and subsequently subtracted from the image. Improved tracking efficiency was achieved by enhancing contrast of the background-corrected images, allowing for 0.3% of pixels to be saturated.

As described before, trajectories were extracted from image stacks via the TrackMate plug-in in FIJI. Due to the transformations outlined above, the contours of the *T.brucei* could

be approximated by a blob with a diameter of $8 \pm 1\,\mu m$. Therefore, tracking was performed utilizing the *Laplacian-of-Gaussian* algorithm with a blob diameter set to 24 ± 2 pixels. The intensity threshold was set to 0.1 ± 0.02 corresponding to $10 \pm 2\%$ of maximum intensity of the image. As in previous evaluation, median filter and sub-pixel localization was switched on. The center-of-mass positions found with this approach were linked using the LAP tracker implemented in TrackMate [161, 162]. A maximum linking distance as well as a gap closing distance of $2\,\mu m$ were chosen as inputs for the algorithm and the gap closing maximum frame gap was set to 2. These values were chosen to be large enough to fit the rather fast motion of parasites of $\langle v \rangle \approx 10\,\mu m/s$ [163, 164], but small enough to prevent crossover of trajectories.
The minimum length of trajectories was chosen to cover at least $N \geq 50$ positions, corresponding to 5 s. Since image processing and acquisition of *trypanosome* data resulted in spots with larger diameter compared to quantum dots, some artifacts could occur. First, to prevent faulty tracked positions while evaluating the data, only trajectories that showed no gaps whatsoever were taken into account. This measure had to be taken since parasites did not show pronounced fluctuations in absorption, nor did they move so rapidly that large scale jumps were justified. Nevertheless it is noteworthy that this more rigorous selection procedures resulted in the termination of trajectories, if *trypanosomes* left the focal plain. Second, to prevent artifacts from edge effects, all trajectories with a center of mass closer than $3\,\mu m$ to any edge were discarded, thus allowing only unperturbed, fully imaged specimen to contribute to the statistics. Eventually an overall minimal track displacement condition, i.e. end-to-end distance, $|\mathbf{r}_N - \mathbf{r}_0| \geq 3\,\mu m$ was applied to remove dead, stuck, or overall immobile specimen. Note that this specific condition was not applied for measurements using *poly-L-lysine* coating, since these were expected to be stuck.
After tracking, all trajectories with $N \geq 100$ positions and frame time $\Delta t = 100\,ms$, as well as all associated metadata were exported as `.csv` and `.xml` files, respectively. Subsequently, tracks were converted to `ASCII` files and analyzed in `MATLAB` with custom-written codes.

3.2. Calculating the MSD and extracting the anomaly exponent

After SPT and data processing is performed and reconnected trajectories are obtained in a useful format, analyzing the trajectories and finding parameters of their (diffusive) motion and particle dynamics has to be done. To this end, the most common quantities extracted from SPT data are explained in more detail in the following sections.

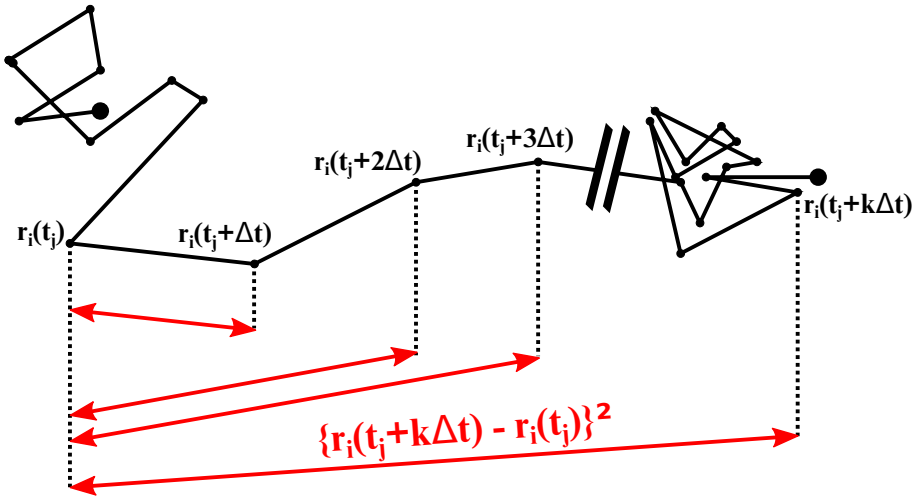

Figure 3.2: Schematic representation of the calculation of squared increments (red arrows) of a 2D trajectory (black line) with given frame time Δt at distinct sample times (solid black circles). The disconnection (two parallel black lines) indicate a unknown gap in the trajectory.

3.2.1. The mean squared displacement

The **mean squared displacement (MSD)**, described as the average extent of space explored by a tracer as a function of lag time $k\Delta t$ is the most common approach for the analysis of SPT data. The time-averaged MSD (TA-MSD) can be calculated, assuming a specific tracer i with trajectory $\mathbf{r}_i(t)$ diffusing in two dimensions with position coordinates $\mathbf{x}_i = \{x_i, y_i\}$ sampled at N discrete times $j\Delta t$, as:

$$\left\langle r^2(\tau) \right\rangle_t = \frac{1}{N-k} \sum_{j=1}^{N-k} \left[\mathbf{r}((j+k)\Delta t) - \mathbf{r}(j\Delta t) \right]^2 . \tag{3.3}$$

This equation is equal to Eq.1.7. A schematic representation of how to calculate the squared displacements of a two dimensional trajectory is shown in Fig.3.2. The trajectory is sampled with a given frame time Δt at distinct times (solid black circles). Note that to get to Eq.3.3 all possible lag times $\tau = k\Delta t$ have to be sampled. This was done using a sliding window approach. The resulting oversampling [165] does not change the slope of the MSD curve, but rather smoothens it due to averaging. It should be clear that larger lag times result in poorer statistics and therefore lead to larger deviations from the mean value in the ensemble average. This phenomenon is visible in Fig.3.3.

For normal diffusion, i.e. $\alpha = 1$, the MSD grows linearly in time according to Eq.1.10, as shown in Fig.3.3. In the figure, the ensemble average of individual time-averaged MSD curves is shown in black. The double logarithmic plotting allows for fast recognition of a power-law behavior. The weighted standard deviation of the individual trajectories

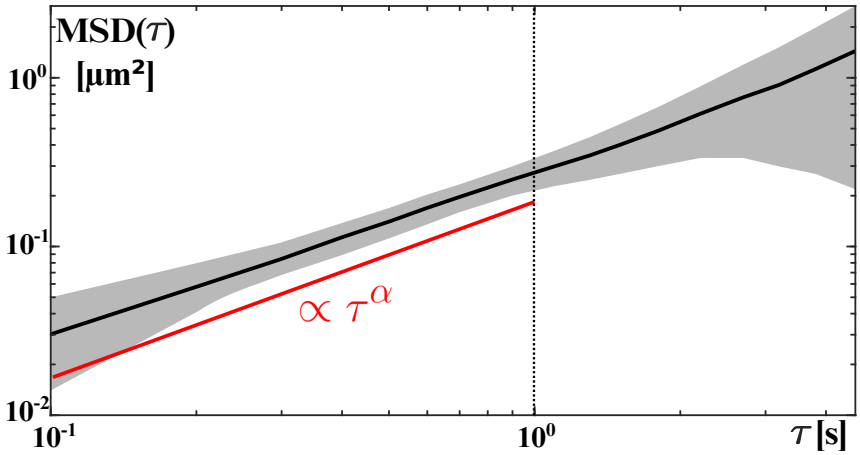

Figure 3.3: Double logarithmic plotting of the time-averaged MSD of quantum dots diluted in sucrose solution (60% w/w) in dependency of the lag time τ according to equation Eq.3.3. The ensemble average of 19 individual TA-MSDs (solid black line) shows linear scaling according to $\langle \mathrm{MSD}(\tau)\rangle_E = K_\alpha \tau^\alpha$ with $\alpha = 1$ (solid red line) in the fit range $100\,\mathrm{ms} \leq \tau \leq 1\,\mathrm{s}$. The weighted standard deviation of individual trajectories is depicted in gray. Note that the deviations are larger for short lag times due to dynamic and static offset as described in 3.1. The deviations for longer lag times are due to poor statistics.

TA-MSDs is depicted as a gray area. As mentioned before, poor statistics for large lag times τ result in larger deviations. On the other hand, dynamic and static offsets due to experimental limitations as described in Sec.3.1 lead to deviations for data in the small lag time regime. Note that the ensemble-averaged TA-MSD for trajectories of different length has to be calculated using weighted functions with factors w_i such that w_i depends on the number a specific lag time τ_j is present while calculating the TA-MSD of the individual trajectory $N_i(\tau_j)$. Hence longer trajectories might influence smaller lag times more in the ensemble average. Due to this, only trajectories of the same length have been ensemble-averaged at most. The weighted ensemble average can be calculated according to:

$$\langle \mathrm{MSD}(\tau)\rangle_E = \frac{\sum_{i=1}^{N} (w_i \cdot \langle \mathrm{MSD}(\tau)\rangle_t)}{\sum_{i=1}^{N} w_i}. \tag{3.4}$$

Following previous reports [30, 158], time-averaged MSDs were fitted with a simple power-law $\langle \mathrm{MSD}(\tau)\rangle_t = K_\alpha \tau^\alpha$, i.e. linearly in logarithmic spacing, in the range $\Delta t \leq \tau \leq 10\Delta t$, with $\Delta t = 0.1\,\mathrm{s}$ as depicted in Fig.3.3 with a solid red line. The anomaly exponent α and the generalized transport coefficient K_α were extracted from the fit. Due to the double logarithmic plotting, the power-law behavior appears as constant inclination proportional to the anomaly exponent.

After extracting the diffusion anomaly and the generalized transport coefficient for individual trajectories, both quantities were analyzed via their respective probability density functions (PDF). Different experimental conditions were compared on the basis of mean values extracted from the distributions, as well as shape and scaling behavior of the individual PDFs.

To validate the significance of the mean exponent $\langle\alpha\rangle$ and to probe for potential perturbation of power-law scaling due to statistic and dynamic localization errors [166], a bootstrapping approach as described in the following section was exploited.

3.2.2. Averaging and bootstrapping

In general, a **bootstrapping approach** could be any metric that relies on random sampling with replacement. Thus, it is a technique that allows estimations of the tested distribution of almost any statistics using random sampling methods [167, 168].

The basic idea in bootstrapping is that the true probability distribution P of a population is unknown, but an empirical distribution $\tilde{P}$ is given due to sampled data. Assuming now that conclusions can be drawn on the basis of $\tilde{P}$ and that inference are analogous to inference of the original unknown data P, resampling of $\tilde{P}$ increases accuracy of inference. In other words, in bootstrapping-resamples, the known sample is treated as the population; thus by drawing new samples $\hat{P}$ with replacement, the quality of inference of the 'true' sample is measurable. This only works, if $\tilde{P}$ and $\hat{P}$ are reasonable approximations of P.

For the bootstrapping approach used in the course of this work, the following scheme was used:

(i) Randomly select a non-exhaustive ensemble of $N = 100$ TA-MSDs $\langle \mathrm{MSD}(\tau)\rangle_t^{(i)}$ extracted from a total set of several hundred individual trajectories for a given constant condition (e.g. length N, drug used, ...). This is the new sample population $\hat{P}$ drawn from $\tilde{P}$.

(ii) Average the sample population to a single, sub-ensemble-averaged TA-MSD and determine the scaling exponent $\hat{\alpha}$.

(iii) This random drawing with replacement from the total set of TA-MSDs $\tilde{P}$ and subsequent averaging was repeated $M = 200$ times to obtain the PDF $p(\hat{\alpha})$ for the values of the anomaly exponent.

Since both $\tilde{P}$ and $\hat{P}$ are of a reasonable degree of statistical relevance and therefore are reasonable approximations of the underlying 'real' population, conclusions can be drawn on the basis of the comparison of estimators of the empirical samples.

Note here that the standard deviation and thus the width of the newly found PDF of $\hat{\alpha}$ values obtained with the bootstrapping approach is determined by the ratio $\tilde{\sigma}/\sqrt{M}$, where $\tilde{\sigma}$

is the standard deviation of the $p(\tilde{\alpha})$ derived from the individual TA-MSDs. This holds true since finding $p(\hat{\alpha})$ boils down to an arithmetic averaging of individual values of anomaly exponents. For creating each sub-ensemble-averaged MSD, either one of the following averaging approaches was exploited.

First, a **simple arithmetic averaging** of individual TA-MSDs was used according to equation Eq.3.5. It is the most commonly used measure of central tendency in a set of data and is defined as being equal to the sum of the numerical values of each and every observation divided by their total number.

$$\langle \mathrm{MSD}(\tau) \rangle_{t,\mathrm{a}} = \frac{1}{N} \sum_{i=1}^{N} \langle r^2(\tau) \rangle_t^{(i)} \tag{3.5}$$

Since the MSD is not a single number, but a variable dependent on τ, averaging has to be done for every single lag time.
Even if the arithmetic mean is often used to describe central tendencies, it is not a robust quantity. In fact, it is greatly influenced by outliers and skewed distributions. Since the data reported on in this thesis are of experimental nature and hence prone to show strong deviations, another averaging approach was used.

Following Eq.3.6, the **geometrical mean** was calculated during bootstrapping. It is defined as the Nth root of the product of N observations:

$$\langle \mathrm{MSD}(\tau) \rangle_{t,\mathrm{g}} = \left(\prod_{i=1}^{N} \langle r^2(\tau) \rangle_t^{(i)} \right)^{1/N}. \tag{3.6}$$

Compared to the aforementioned arithmetic mean, the geometric mean captures outliers better, in the sence that it does not overrate them and since it only applies to positive numbers, it can be used in the context of squared displacements. It is noteworthy that the logarithm of equation Eq.3.6 is similar to the mean-log-square displacement proposed by Kepten et.al [169] which can be used to reduce systematic errors in the estimation of $\langle \alpha \rangle$,

$$\log \left[\left(\prod_{i=1}^{N} \langle r^2(\tau) \rangle_t^{(i)} \right)^{1/N} \right] = \frac{1}{N} \sum_{i=1}^{N} \log \left[\langle r^2(\tau) \rangle_t^{(i)} \right]. \tag{3.7}$$

When studying the intracellular fluctuations one is forced to be in the range of small increments. Therefore, to prevent numerical inaccuracies in the calculation because of small numbers and rounding errors, equation 3.7 rather than equation 3.6 was used in the implementation of the algorithm.

An example of the bootstrapping approach is shown in Fig.3.4. The solid black circles show the PDF of anomaly exponents of 10,000 individual trajectories from simulation, whereas

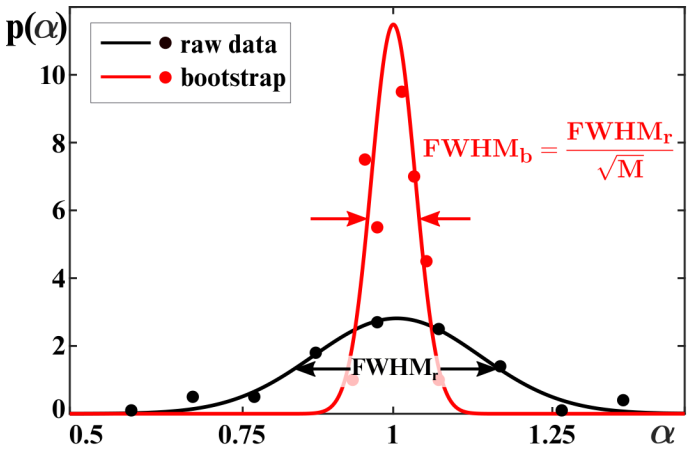

Figure 3.4: PDF of anomaly exponents α of 10,000 simulated trajectories before (black circles) and after (red circles) the bootstrapping approach using $N = 100$ and $M = 25$. Colored solid lines show Gaussian fits to the data. The change in FWHM is apparent, while the mean value $\langle\alpha\rangle$ is preserved. The width of the bootstrapped PDF can be tuned via the number of repetitions M.

the red solid circles represent the data after bootstrapping with geometrical averaging of $N = 100$ random drawings and only $M = 25$ repetitions. The solid black and red lines are Gaussian fits to the respective data. Binning of all histograms were done using Scott's rule. The approach does not change the mean value of the distribution, but obviously tightens the FWHM as indicated by the black and red arrows, respectively. Note here that the FWHM of the normal distribution can be converted to fit the representation of the standard deviation σ via:

$$\mathrm{FWHM} = 2\sqrt{2\ln 2} \cdot \sigma. \tag{3.8}$$

In conclusion, the great advantage of bootstrapping is its simplicity. The approach allows for straightforward estimation of standard errors of complex and not yet fully understood distributions. Moreover, bootstrapping is a convenient method to get other groups of sample data without the cost of repeating the experiment. It also is an appropriate way to check for stability of results as well. However, when using bootstrapping approaches, always keep in mind that no new data is created, but only presentation is changed and a sufficient statistics of data is needed either way.

3.3. The velocity autocorrelation function

After visiting the most common estimators for diffusion, namely the (generalized) transport coefficient K_α and the anomaly exponent α, another typical quantity accessible from SPT data – the **velocity autocorrelation function** (VACF) – is studied.

To this end the velocity at time t given via the increments in a period δt

$$\mathbf{v}(t) = \frac{\mathbf{r}(t+\delta t) - \mathbf{r}(t)}{\delta t} \tag{3.9}$$

was extracted for every single trajectory. Subsequently, the temporal autocorrelation of these velocities was calculated and ensemble averaged to be:

$$C_v(\tau) = \frac{\langle \mathbf{v}(t) \cdot \mathbf{v}(t+\tau) \rangle_{t,\mathrm{E}}}{\langle \mathbf{v} \rangle^2}. \tag{3.10}$$

The VACF is an indicator of the underlying mechanism that describes the random motion. Therefore, assuming different mechanisms lead to a multitude of predictions for the VACF of which some are briefly described below, beginning with the most persuasive description of the data presented in this thesis: antipersistent fractional Brownian motion.

The VACF for such a fBM shows a prominent negative peak as expected for antipersistent random walks. These anticorrelations occur since the particle is bound to be in a viscoelastic medium. The distinct memory kernel can be tested on all time scales by varying $\delta t = k\Delta t$ in multiples of the frame time Δt resulting in pronounced negative peaks for $\tau = \delta t$. Hence, by rescaling the time as $\xi = \tau/\delta t$, all VACF traces should collapse to a single master curve. The ensemble-averaged VACF according to Eq.3.10 of simulated fBM data of $M = 10,000$ trajectories with individual length $N = 100$ calculated using the `wfbm` routine in `MATLAB` with a Hurst coefficient of $H = 0.275$ (cf. $\alpha = 0.55$) is shown in Fig.3.5. The ensemble-averaged VACF is depicted with full black circles while the gray area is the weighted standard deviation of individually calculated VACFs. The dashed gray line marks the zero position and serves as a guide to the eye. The correlation starts out to be positive, due to its self-similarity, but tumbles down quickly and reaches its minimum at $\xi = 1$, after which it approaches $C_v = 0$. The deviations from zero, i.e. no correlation, occur due to trajectory-to-trajectory fluctuations. The analytic prediction of the VACF for fBM, namely

$$C_v(\xi) = \frac{(\xi+1)^\alpha + |\xi-1|^\alpha - 2\xi^\alpha}{2} \tag{3.11}$$

rescaled to $\xi = \tau/\delta t$ with $\delta t = 5\Delta t$ in the simulation is shown in red. Here the anomaly exponent is set to $\alpha = 0.55$, i.e. the value used in the simulation. When comparing experimental data to the analytical prediction given in Eq.3.11, α was set to the value $\langle\alpha\rangle$ found with the bootstrapping approaches.

Comparing the VACF of fBM to another model for subdiffusive behavior – namely unbound CTRW – one notices big differences in shape and behavior. According to Burov and Metzler [12, 18] the position correlation in an interval $[t_i, t_j]$ with $t_j > t_i$ and initial conditions

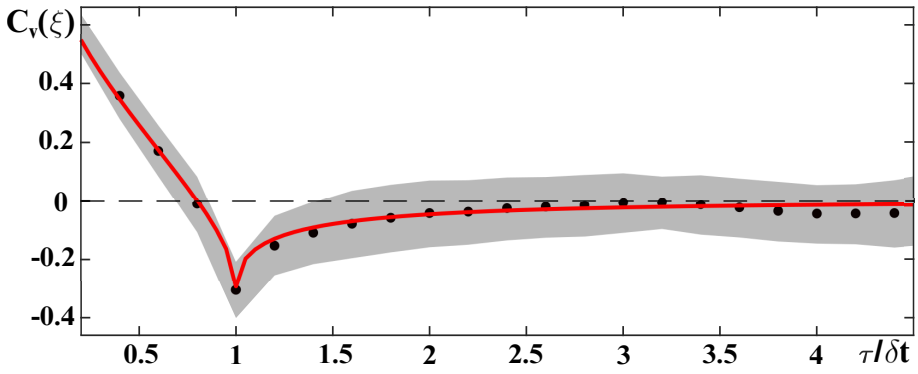

Figure 3.5: Ensemble-averaged VACF of 10,000 simulated fBM trajectories (full black circles), rescaled to $\xi = \tau/\delta t$ with $\delta t = 5\Delta t$. Weighted standard deviations shown as gray area. The 'no correlation' threshold, i.e. $C_v = 0$ is shown as a dotted line and serves as a guide to the eye. The solid red line is the analytical prediction of the VACF according to Eq.3.11, with $\alpha = 0.55$.

$\mathbf{r}(t = 0) = 0$ is given by the following expression:

$$\langle \mathbf{r}(t_i)\mathbf{r}(t_j)\rangle = \frac{2K_\alpha}{\Gamma(1+\alpha)} \left[\min\{t_i, t_j\}\right]^\alpha , \tag{3.12}$$

where K_α is the generalized transport coefficient and α is the anomaly exponent. This result for unbound CTRW is due to the fact that jump lengths have zero mean in the given interval. With Eq.3.12, the normalized VACF can be found to be:

$$\frac{C_v(\tau)}{C_v(0)} = \begin{cases} \frac{\delta t^\alpha - \tau^\alpha}{\delta t^\alpha} & \tau \leq \delta t \\ 0 & \tau \geq \delta t \end{cases} . \tag{3.13}$$

Since the unbound CTRW is a Markovian process, i.e. there is no correlation of different jumps, the velocity autocorrelation function does not yield any negative values. Hence, it can be easily distinguished from the VACF for fractional Brownian motion and therefore the VACF can be used to decide which underlaying process is the most reasonable. It is noteworthy that Eq.3.13 is non-analytic at $\tau = \delta t$. This observation has been confirmed in simulation [18].

In contrast to the aforementioned subdiffusive processes of random motion, the following paragraph will focus on the **persistent random walk** as described before in Sec.1.2.2. It is an example of a Gaussian process with stationary probability distribution and bound variance. In contrast to a Wiener process, the drift term in such a process is not constant, but dependent on the current state. In fact, a positive drift is set if the current value of the process is less than the long-term mean and the opposite holds true if the state of the process is larger than the long-term mean. Hence, the mean acts as an equilibrium level and the process can be dubbed *mean-reverting*. The persistence in increments on

a characteristic timescale defined by the persistence time τ_P results in a positive velocity autocorrelation according to [65]:

$$C_v(\tau) = \frac{nD}{\tau_P} \cdot e^{-\tau/\tau_P}. \tag{3.14}$$

In contrast to the VACFs mentioned before, the velocity-correlation of persistent random motion decrease more slowly and only approximates $C_v = 0$ asymptotically, with a decay time governed by its persistence time.

Eventually, since velocity autocorrelation functions come in various but distinct shapes, they are a good estimator of the underlying process creating their respective trajectories and therefore are a reasonable quantity to analyze.

3.4. The statistics of normalized increments

In recent years, a more elaborate quantity regarding random walk processes, namely the probability distribution function of displacements, gained more attention [21, 89, 90, 170]. For this purpose the histograms of the displacement distributions are usually plotted for certain lag times δt. Since random walks should not have any preferential direction regarding 'artificial' coordinates in the laboratory system and thus no systematic differences are assumed, x- and y-directions can be calculated individually for each trajectory and subsequently combined into a single set.

To this end, the PDF of the normalized increments χ within a certain lag time $\delta t = k\Delta t$ were inspected. The individual time series of increments $\Delta x_i = x(t_i + \delta t) - x(t_i)$ and $\Delta y_i = y(t_i + \delta t) - y(t_i)$ were calculated and normalized by their distinct root-mean-squared step length according to Eq.3.15.

$$\chi_i(\delta t) = \frac{\Delta x_i}{\sqrt{\langle \Delta x^2 \rangle_i}}, \quad \text{with } \langle \Delta x^2 \rangle_i = \tfrac{1}{N} \sum_{i=1}^{N} \Delta x_i^2 \tag{3.15}$$

For a homogeneous random walk – be it due to fractional or normal Brownian motion – the individual trajectory displacement distributions should exhibit a Gaussian distribution independent of the time scale ($k\Delta t$), since neither spatial nor temporal heterogeneity should come in effect. This holds true due to the fact that the central limit theorem (CLT) enforces a Gaussian shape of $p(\chi)$. For such a process the distribution is defined by

$$p(\chi; \mu, \sigma) = \frac{1}{\sqrt{2\pi\sigma^2}} \exp\left(-\frac{(\chi - \mu)^2}{2\sigma^2}\right). \tag{3.16}$$

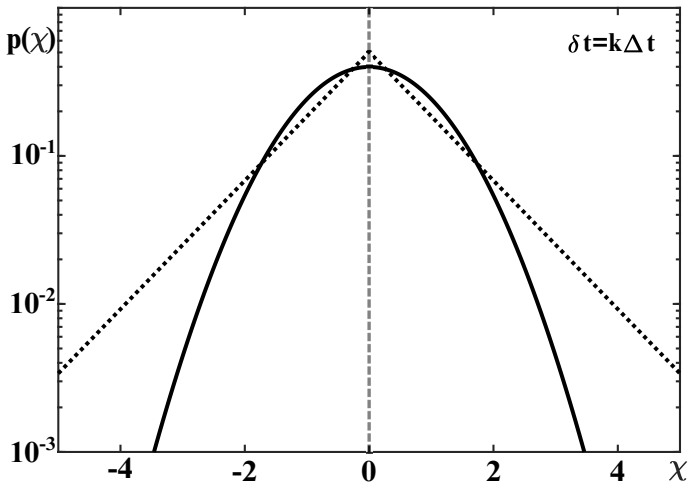

Figure 3.6: Semilogarithmic plotting of the PDF of normalized increments χ for an arbitrary lag time δt. The solid black line shows an anticipated *Gaussian* for Brownian motion according to Eq.3.16 whereas the dotted black line represents a *Laplace* distribution (Eq.3.17). Both distributions have the same mean $\langle\chi\rangle = 0$ (dashed line) and standard deviation $\sigma = 1$, but show significant differences in the overall shape.

The mean value of this distribution is $\mu = \langle\chi\rangle_i = 0$ and the standard deviation is $\sigma = 1$, due to normalization. Note that setting the variance to $\sigma^2 = 2nDt$ results in Eq.3.16 becoming the propagator for Brownian motion.

It has been shown in previous studies [21, 90] that other, non-Gaussian kinds of increments displacement distributions could occur for specific conditions of Brownian motion, when the homogeneity of the system is broken. For SPT on protein-labeled mRNA in living *E.coli* for example, Lampo et. al [89] observed an exponential (*Laplace*) distribution according to

$$p(\chi;\mu,\sigma) = \frac{1}{\sqrt{2\sigma^2}} \exp\left(-\frac{\sqrt{2}|\chi-\mu|}{\sigma}\right). \tag{3.17}$$

Again, it can be found that the mean value vanishes ($\mu = 0$) and the standard deviation is $\sigma = 1$. Fig.3.6 shows the PDFs according to Eq.3.16 and 3.17 with solid and dotted black lines respectively in semilogarithmic space for an arbitrary lag time $k\Delta t$. While both distributions have the same mean $\mu = 0$, variance $\sigma^2 = 1$ for normalized displacements, the Laplace distribution has 'wider wings' compared to the Gaussian. Hence, the statistics of normalized increments could reveal interesting insights in Brownian, yet non-Gaussian motion behavior due to sterical or temporal heterogeneity [21, 90].

3.5. The local convex hull approach

Identifying transport modes in a complex biological environment is a challenging problem. While a wide variety of experimental observations revealed anomalous diffusion features in microscopic biophysics [6, 11, 22, 23, 33, 34], their origins maintain debatable. Since advances in optical microscopy have significantly increased the accuracy of SPT over the last decades [158], new evaluation analysis of single trajectories have arisen, many of which from statistical theory.

The detection of different phases in single random trajectories due to spatial or temporal variation of diffusivities, change in Hurst coefficient in fBM, or any other perturbation of homogeneity has been the focus of some recent theoretical studies [171, 172]. They proposed a model-free detection of change points between distinct phases in an intermittent stochastic process. To this end, the **local convex hull (LCH)** is exploited. This geometrical quantity and its properties (e.g. the diameter or volume) are used to discriminate between distinct phases of individual trajectories.

The convex hull is the smallest possible convex envelope that contains all points of a finite set. Mathematically speaking, it is the set of all convex combinations of the subset $\{\mathbf{r}_1, ..., \mathbf{r}_n\} \subset \mathbb{R}^d$:

$$\mathrm{Conv}(\mathbf{r}_1, ..., \mathbf{r}_n) = \left\{ \sum_{j=1}^{n} a_j \mathbf{r}_j | a_j \geq 0, \sum_{j=1}^{n} a_j = 1 \right\}. \tag{3.18}$$

In a two-dimensional planar space, the convex hull of a finite set is a convex polygon with the vertices being some of its points. Since this work only features 2D trajectories, convex hulls of higher dimensions are not discussed here.

Going one step further, the time dependent local convex hull of a single trajectory was computed using the `quickhull` algorithm [173] for two dimensional data sets in its `MATLAB` compatible function `convhull`[3]. The local convex hull was computed over $2k + 1$ points $\{\mathbf{r}(t_j - k\Delta t), \mathbf{r}(t_j - (k-1)\Delta t), ..., \mathbf{r}(t_j + k\Delta t)\}$ around a distinct time t_j and the geometrical property of its local diameter $S_d(t_j)$ was extracted.

$$S_d(t_j) = \mathrm{diam}\left[\mathrm{Conv}(\mathbf{r}_{j-k}, ..., \mathbf{r}_{j+k})\right] \tag{3.19}$$

Note here that the diameter of the LCH is simply the largest distance between any two points in the sequence. Another functional that can be computed using the LCH is its volume. However, this work focused on its diameter and since both quantities show similar temporal developments, no further attention was paid to the volume. The integral-like

[3] When using this routine, a colinearity check regarding x- and y-increments has to be implemented to avoid one-dimensional data sets that cannot be handled.

character of this approach requires less statistics within individual trajectories as compared to a local TA-MSD analysis. Hence it can proof useful when dissecting different modes of motion.

For consistency with the previous analysis of the PDF of normalized increments $p(\chi)$ as discussed in Sec.3.4, rescaling of all trajectories had to be done. Therefore, the individual increments of the trajectory with length $N = 100$ were rescaled by the respective average displacement at minimal length scale

$$\Delta r = \sqrt{\langle |x_{i+1} - x_i| \rangle^2 + \langle |y_{i+1} - y_i| \rangle^2}, \tag{3.20}$$

for $i = 1, ..., N-1$. After rescaling, the diameter of the local convex hull of the individual trajectory was computed.

A schematic depiction on how the LCH, as well as its diameter, was found is shown in Fig.3.7**(a)**. The solid gray line is an arbitrary two-dimensional trajectory $\mathbf{r}_i(t)$ of length N with distinct time sampling with frequency Δt^{-1} at times t_j shown as solid black circles. The LCH was computed at all times $k\Delta t \leq t \leq (N-k)\Delta t$ according to Eq.3.18 and its corresponding diameter $S_d^{(i)}(t = t_j)$ was extracted. In Fig.3.7**(a)** three representative LCHs (color coded areas) at distinct times t_j (color coded crosses) are shown in blue, red and green. Their diameters S_d are depicted as dotted lines, color coded to fit the area.

In panel **(b)** of Fig.3.7, the temporal development of the diameter of the local convex hull $S_d(t)$ is shown. It is worth noting that the first point to evaluate is always $t_j = k\Delta t$ since earlier times lack sufficient statistics to compute a meaningful LCH. It can be seen that the diameter of the LCH changes quite a bit over the course of the trajectory. Temporal changes in the diameter of the local convex hull could in turn hint towards embedded heterogeneity of the motion. In this subfigure, the diameters of the local convex hulls according to the distinct times color coded in Fig.3.7**(a)** are shown again using crosses according to the colors used before.

To further investigate on possible perturbations of simple Brownian motion and presumably underlying heterogeneities, the probability distribution function of LCH diameters had to be calculated. Assuming stationarity – hence combining all values $S_d(t)^{(i)}$ of all trajectories $\mathbf{r}_i$ from one condition into a single PDF – revealed a non-Gaussian shape for $p(S_d)$, thus suggesting some sort of heterogeneity to be encoded in the trajectories. A more pronounced tail of the PDF towards larger S_d values could possibly hint towards at least two states of mobility, i.e. a more dominant less mobile fraction and a state with higher mobility encoded in single trajectories.

To probe whether or not a particle undergoes different modes of motion within individual trajectories, a threshold value θ had to be defined. In Fig.3.7**(c)** this threshold is shown with a dashed line. Since this threshold is somewhat arbitrary, a meaningful value has

to be found. To this end, the mean μ and the standard deviation σ of the previously found PDF $p(S_d)$ was used to define θ. Therefore, for any excursion $S_d(t) \geq \theta$, the moving particle was classified to be in the high-mobility state (light orange areas in Fig.3.7**(c)**). In the context of this thesis, this state will be called 'off'-state. If the threshold value is not exceeded, the particle is rated to be in the low mobility state, hereinafter called 'on'-state (light gray areas in Fig.3.7**(c)**). Subsequently, the residence times τ_{off} and τ_{on} of the mobility states can be quantified as indicated with black arrows in Fig.3.7**(c)**. Note here that every individual $S_d(t)^{(i)}$ yields on average several dwell times of both states, which

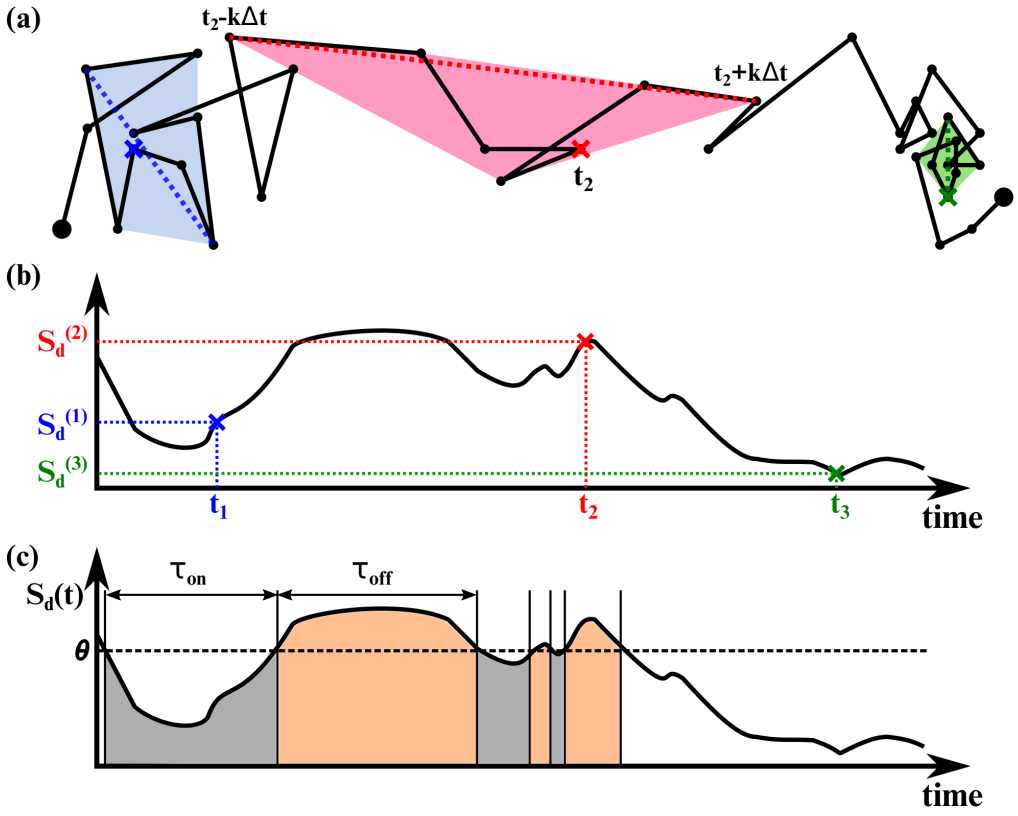

Figure 3.7: Schematic depiction of the LCH approach. **(a)** shows an arbitrary trajectory of a switching random walk process (solid black line) with distinct time sampling t (full circles) and frame time Δt. At times t_j, depicted as blue, red and green crosses, respectively, the individual local convex hull (color coded shaded areas) was computed and the diameter $S_d(t_j)$ (color coded dotted lines) was determined. In this example $k = 3$ was chosen. **(b)** The temporal development of the diameter of local convex hulls $S_d(t)$ of a single trajectory is shown. Note here that the first time point to evaluate is always $t = k\Delta t$. The computed $S_d^{(j)}$ from above are shown with their respective color coding. **(c)** To distinguish whether or not a particle is in a state of somewhat higher mobility, a threshold value θ (dashed black line) had to be defined. All conditions $S_d(t) \geq \theta$ were rated to be in a more mobile ('off') state indicated by the light orange area while time spend in less mobile ('on') states is shown in gray. The choice of θ is somewhat arbitrary and will be discussed later. Examples of the sections a single trajectories stays in one or the other state – the so called residence times τ_{off} & τ_{on} – are indicated by black arrows.

can be displayed as $p(\tau)^{(i)}$. Since no information on how long the current mode is already employed when beginning measurements, nor how long the last state will be occupied after terminating experiments is available, the first and last extracted residence time of each individual trajectory are discarded. In Fig.3.7**(c)** the first and last assigned state are shown without any color coding (i.e. in white) to illustrate that they were not taken into account. Trajectories that did not show any intermittent behavior, i.e. switching from one state to another according to the assumed threshold, were assigned to the current state they occupied and their residence time was given as $\tau_{\max} = (N-2k)\Delta t$. Therefore, the fraction of trajectories that showed intermittent behavior depending on the assigned threshold could be evaluated. Again, assuming stationarity, the individual PDFs of residence times can be combined into one single PDF $p(\tau)$ for each condition. It is worth noting at this point that the fairly short experimental time series with only $N = 100$ positions cannot accurately reveal the value of mean residence times if they are larger than $N\Delta t$. Yet, when assuming a Markovian nature of the process, meaningful exponential PDFs can be obtained that yield an estimate for the ratio $\langle\tau_{\mathrm{on}}\rangle/\langle\tau_{\mathrm{off}}\rangle$.

In summary, the convex hulls of single trajectories normalized to their minimal length scale using a small number of consecutive points was computed, which reflects individual dynamics on a local scale. With this approach, time series of the maximum diameters $S_d(t)$ of the locally found convex hulls could be defined and analyzed. When assuming stationarity, all S_d values can be combined into a single PDF and conclusions can be drawn based on the mean value, standard deviation, and shape of $p(S_d)$. Looking at the individual LCHs again, a threshold based on the previously found mean value and standard deviation can be defined that dissects the trajectory into more and less mobile states. Subsequently the distributions of residence times of these states can be extracted and analyzed.

3.6. The autocorrelation of fluctuations in squared increments

Searching for signs of temporal variations of diffusive characteristics in trajectories of tracer particles – presumably induced by heterogeneity in their local environment – can be tricky, since a lot of popular quantities do not probe for heterogeneity to begin with or hide traces of non-Gaussian behavior in ensemble or time averages. Additional support in the search for non-homogeneous diffusion on the other hand could be given by the **autocorrelation of squared increments** $G(\tau)$ [174].

The ensemble-averaged autocorrelation of squared increments $\Delta r^2(t) = |\mathbf{r}(t+\Delta t) - \mathbf{r}(t)|^2$ is given by the following equation:

$$G(\tau) = \left\langle \frac{\langle \Delta r^2(t) \cdot \Delta r^2(t+\tau)\rangle_t - \langle \Delta r^2(t)\rangle_t^2}{\langle \Delta r^2(t)\rangle_t^2} \right\rangle_{\mathrm{E}}. \tag{3.21}$$

This quantity should consequently yield $G(\tau) = 0$ for all $\tau > \Delta t$ if a pure, non-switching (fractional) Brownian motion is assumed. The development of $G(\tau)$ of an ensemble of M simulated pure fBM trajectories with an anomaly exponent $\alpha = 0.7$ and N positions is shown in Fig.3.8. $G(\tau)$ is basically zero beyond the basic time increment $\tau = \Delta t = 0.1\,\mathrm{s}$ for all simulated, pure fBM data. The length of the trajectory does not change the long term behavior of $G(\tau)$ in any way. Note here that for short trajectories ($N = 100$, red full circles), a negative but constant value is assumed. This artifact is due to statistical errors in the calculation: Subtracting the baseline when calculating the autocorrelation of squared increments is only correct up to an uncertainty $\sim 1/\sqrt{N}$. This yields a constant $G(\tau \gg \Delta t) \sim -1/N$ that subsides for longer trajectories.

On the other hand, for sufficiently long trajectories of an intermittent dichotomous process with rates k_{on} and k_{off}, the autocorrelation of squared increments should decay as [174]:

$$G(\tau) \propto \exp\left[-(k_{\mathrm{on}} + k_{\mathrm{off}})\tau\right]. \tag{3.22}$$

Hence $G(\tau)$ basically describes how long a random walk is fueled by a homogeneous PDF of step increments with a certain mean length before switching to another random walk process with a different mean length. Therefore, a decay of the autocorrelation of squared increments might as well confirm the existence of (at least) two mobility states in the generation of heterogeneous random walk trajectories.

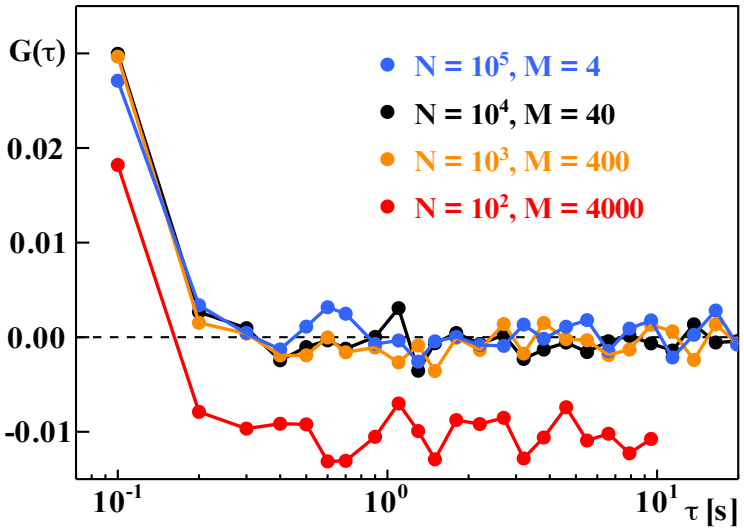

Figure 3.8: The ensemble-averaged autocorrelation of fluctuations in the squared increments of M simulated, pure fBM trajectories with $\alpha = 0.7$ and N positions yields $G(\tau) \approx 0$ (dashed black line) for all $\tau > \Delta t$. Statistical errors may occur for short trajectories resulting in a negative, but constant offset (see $N = 100$, red circles). The uncertainty subsides for longer trajectories.

3.7. Other properties of motion

When examining modes of motion, many different properties can be chosen. In the following paragraph, some of these quantities and how to calculate them are listed. Since most calculations presented in the following are straight forward and do not need any in depth explanations, it was decided not to give them separate sections.

Instantaneous velocity One of the most basic quantities to extract from trajectories of somewhat persistent motion is the instantaneous velocity $v_\mathrm{i}(\delta t)$. It is defined by the ratio of the increments length $\Delta r_i = |\mathbf{r}_{i+k} - \mathbf{r}_i|$ divided by the lag time, hence, $v_\mathrm{i}(\delta t) = {}^{\Delta r_i}/_{\delta t}$ with $\delta t = k\Delta t$. The probability distribution function $p(v_\mathrm{i})$ can be subsequently compared for different experimental conditions.

Straightness This quantity proposed by Wagner et. al [175] relates the net displacement of a certain part of the trajectory with time lag $\delta t = k\Delta t$ to the sum of all step lengths walked during this period according to:

$$S_j(k\Delta t)^{(i)} = \frac{|\mathbf{r}_{j+k} - \mathbf{r}_j|}{\sum\limits_{l=j+1}^{j+k} |\mathbf{r}_l - \mathbf{r}_{l-1}|}. \tag{3.23}$$

Similar to the LCH approach discussed earlier (see Sec.3.5), the straightness S was calculated for $N-2k$ sections j of each individual trajectory $\mathbf{r}_i(t)$ with length N. Subsequently, all values S_j of all trajectories were combined into one PDF $p(S)$ for matching experimental conditions since stationarity was assumed. In contrast to the LCH, the straightness is a self-normalizing quantity, hence increments did not need to be normalized before calculation to make them comparable. Due to this, $0 \leq S \leq 1$ holds true generically, with the limiting cases obviously being $S = 0$: the particles position at t_j and $t_j + \delta t$ are equal; and $S = 1$: all steps were taken in the exact same direction, i.e. $\langle \mathbf{r}(t) \cdot \mathbf{r}(t+k\Delta t) \rangle_t = 1\,,\ \forall k \in \mathbb{N}$.

Mean asphericity In contrast to the more often used radius of gyration as a measure of size, the asphericity or asymmetry A provides a measure of shape of the random walk [176]. It can mathematically be expressed by using the principle radii of gyration R_1 and R_2 of the ellipsoid best enclosing the trajectory as [134]

$$A = \frac{(R_1^2 - R_2^2)^2}{(R_1^2 + R_2^2)^2}. \tag{3.24}$$

In general, random walks have – contrary to the naïve expectation – aspherical geometries. The asphericity can have values between $A = 0$ (sphere like) and $A = 1$ (rod like), with $\langle A \rangle = {}^4/_7$ for a two-dimensional random walk for example [176].

Gaussianity To probe the underlying random walk model of the SPT data, the stationary distribution of increments can be analyzed using the Gaussianity as proposed by Ernst et. al [25]. This quantity relates the time-averaged quartic moment of a two-dimensional trajectory

$$\left\langle r^4(\tau)\right\rangle_t = \frac{1}{N-k}\sum_{j=1}^{N-k}(r_j - r_{j+k})^4 \tag{3.25}$$

to its squared TA-MSD (see Eq.3.3) such that

$$\gamma(\tau) = \frac{2\left\langle r^4(\tau)\right\rangle_t}{3\left\langle r^2(\tau)\right\rangle_t^2} - 1. \tag{3.26}$$

In general, the Gaussianity should be strictly zero for any random walk model with Gaussian statistics of increments. Strong deviations from zero indicate that the increments are in fact not distributed normally and therefore hint towards changes in the diffusivity in individual trajectories. Nevertheless, the Gaussianity cannot say anything specific about the causes of these deviations. Hence, it is merely an indicator that the diffusion itself is heterogeneous in some way.

3.8. Extracting the helical frequency of persistent *T. brucei* motion

Motion patterns of tracers show distinct features that can help interpret data acquired during SPT. All of the above described measures can be evaluated independent of their origin of trajectories, be it simple diffusion, fractional Brownian motion, or more persistent motion behavior. Therefore, they are all useful while determining the underlying principles of motion.

Since trajectories extracted from (most) kinetoplastids center-of-mass movements show distinct, mostly persistent motion with traces that describe a corkscrew- or wave like pattern as shown in Fig.3.9**(a)**, a more elaborate evaluation, namely the extraction of the **helical frequency** ν_h along the predominant direction of motion, had to be done.

To begin with, a trajectory $\mathbf{r}(t)$ of length N, acquired by SPT of *tryponosomes* as shown in Fig.3.9**(a)** with a black line, was linearly interpolated using a window size w_s. To this end, the start- and end points of a section l of a single trajectory were determined to be:

$$\mathbf{r}_{\mathrm{start},l} = \begin{cases} \mathbf{r}_1 & l = 1 \\ \mathbf{r}_{\mathrm{end},l-1} & l > 1 \end{cases} \tag{3.27}$$

and

$$\mathbf{r}_{\mathrm{end},l} = \frac{1}{w_s}\sum_{j=(l-1)w_s+1}^{l\cdot w_s}\mathbf{r}_j\,, \tag{3.28}$$

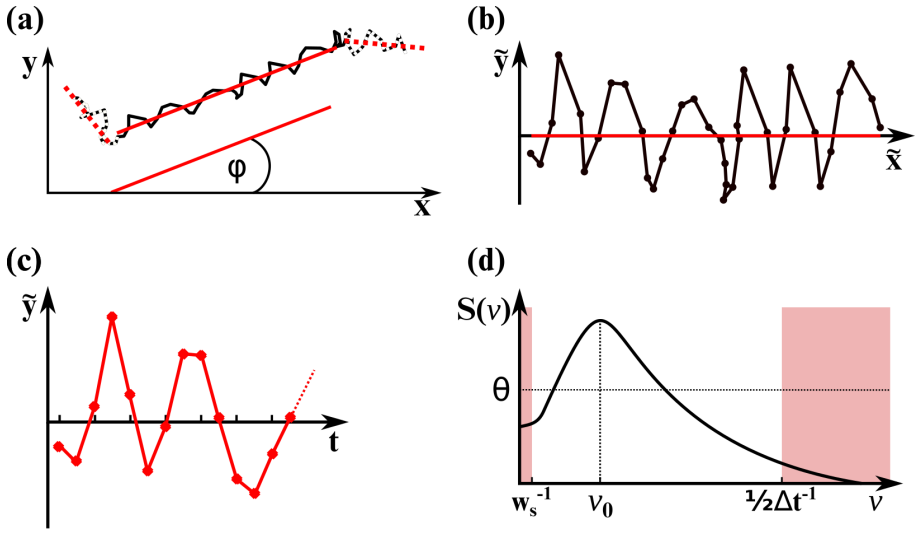

Figure 3.9: Extracting the helical frequency. **(a)** Segment l of a trajectory i (full black line) with linearly interpolated spline (full red line). Previous and following segments are indicated by dotted lines respectively. The angle between spline and x-axis is calculated to be φ. **(b)** Spline and original track segment are transformed by translation to the origin and rotation by $-\varphi$. Distinct coordinates $(\tilde{x}, \tilde{y})$ are shown as black circles. **(c)** The spatial coordinates are translated to a time series of deviations from the spline $\tilde{y}(t)$ and the PSD of the segment is calculated using a fast Fourier transform. **(d)** depicts the determined spectrum $S_l(\nu, T)$ according to Eq.3.29. The peak frequency ν_0 is determined from all values $w_s^{-1} < \nu < 1/2\Delta t^{-1}$ where $S(\nu_0) \geq \theta$. Eventually all obtained values $\nu_0 = \nu_\mathrm{h}$ are combined into a single PDF for matching experimental conditions.

respectively and the interpolation between this points was done using a spline (Fig.3.9**(a)**: red line). The trajectory as well as the spline of the last and next sections $(l \pm 1)$ are shown as dotted lines. Next, the angle φ between x-axis and spline had to be determined. Subsequently, a coordinate transformation had to be done. Hence, the spline segment l and the corresponding original trajectory part l had to be translated to the origin and rotated by $-\varphi$, yielding the transformed coordinated $\tilde{\mathbf{r}}_l(\tilde{x}, \tilde{y})$ as shown in Fig.3.9**(b)**. In a next step, the deviations from $\tilde{y} = 0$ had to be extracted for every distinct time sample (black circle), thus transforming the spatial coordinates to a time series $\tilde{y}(t)$, a cutout of which is depicted in Fig.3.9**(c)** as a red line. Subsequently, the power spectral density (PSD, see Eq.3.29) $S_l(\nu, T)$ of each individual segment l was calculated using a fast Fourier transform (FFT) and its main frequency ν_0 was determined.

$$S_l(\nu, T) = \frac{1}{T}\left|\int_0^T \exp\{i\nu T\}\tilde{y}(t)\mathrm{d}t\right|^2 \quad \text{with } T = w_s = k\Delta t \tag{3.29}$$

This process was repeated l times, hence assigning a mean frequency to each single segment. In a next step, all $\nu_0^{(l)}$ smaller than a certain threshold value θ were discarded. The threshold value $\theta = 0.5$ had to be assumed to rule out all segments that did not show any

clear helical frequency and thus prohibiting noise being interpreted as signal. Additionally all peak frequencies smaller than w_s^{-1} were not taken into account, since they were of no significance. A sketch of a representative PSD including all threshold values is shown in Fig.3.9**(d)**. Eventually all remaining frequencies were renamed $\nu_0 \rightarrow \nu_\mathrm{h}$ and combined into one PDF. It is worth noting that $\nu_\mathrm{h} \leq 5\,\mathrm{Hz}$ had to be assumed generally, due to the *Nyquist-Shannon theorem*, since the temporal resolution during experiments was $\Delta t = 0.1\,\mathrm{s}$ between consecutive frames.

Adding up, in this chapter a variety of different tools and evaluation approaches have been presented. To begin with, the fundamental technique used throughout this work, **single particle tracking**, has been introduced and the required sequence of operations used specifically for measurements with quantum dots in HeLa cells as well as for experiments on kinetoplastids were explained. Next, analysis of the SPT-data was done, beginning with one of the most common quantities when discussing diffusion: the **mean squared displacement**. Calculation and fitting of the TA-MSDs, as well as extraction of associated quantities like the anomaly exponents α and the generalized transport coefficients K_α was discussed. Since the data were large in number but widely distributed, a **bootstrapping** approach had to be implemented to illustrate the results in better detail.

After dealing with the basic evaluation, more elaborate indicators of perturbed motion behavior had to be employed. To this end, the **velocity autocorrelation function**, the **statistics of normalized increments**, the **autocorrelation of squared increments**, and the **local convex hull** have been developed to tackle the scientific question of heterogeneity in subcellular environment and their origins.

Since the motion patterns of inert nanoparticles diffusing in supposedly heterogeneous cellular environment and actively driven living *trypanosomes* are very different, other measures had to be employed to quantify the latter. To this end, the **instantaneous velocity** and the **straightness** were presented, and an approach to extract the **helical frequency** along the predominant direction of motion was derived.

PART II

Elucidating the origin of heterogeneous anomalous diffusion in the cytoplasm of mammalian cells

4. Results

*In this chapter the results of the single particle tracking experiments performed with quantum dots in human cervical cancer cells are presented. Parts of the results presented in the following chapter have been published in Phys. Rev. Lett., **125**, 058101 (2020) [177].*

4.1. Problem definition

Diffusion of supposedly inert tracer particles in complex aqueous environments like the cytoplasm of mammalian cells is often reported to be anomalous with a sublinear scaling of the MSD on a small spatiotemporal scale of a few micrometers and seconds. The rise of the anomaly in motion behavior might be partially explained by crowding effects due to large amounts of macromolecules and other intracellular compartments of largely varying sizes in the local environment of the tracer [6, 15, 88], however, the value of the anomaly exponent α in the cytoplasm [30, 33] is often observed to be considerably smaller, compared to artificial crowded fluids with a similar crowding level [24]. Thus, it seems plausible that crowding is not the only reason for the occurrence of subdiffusion in the cytoplasm and additional mechanisms have to be taken into account.

To this point, no general model exists that reliably describes cytoplasmic subdiffusion in its full extent. As shown by Wong et. al [22], the anomaly exponent of particles can be tuned continuously in an entangled actin filament network, depending on tracer and mesh size. Thus, it seems reasonable that caging effects alter the free diffusion of tracers inside a medium. Furthermore, experiments on non-specific interactions depending on the surface modifications of tracer particles [30] have supported the hypothesis that the local environment, i.e. non-inert crowders, may have an impact on the diffusion of particles. In the context of the intracellular environment, the cytoskeleton as well as membrane bound organelles, e.g. the ER, are promising candidates worth considering when searching for cytoplasmic binding partners that enforce the emergence of subdiffusion. Adding to the complexity, subdiffusion in microscopic biological environments has been reported to show traces of heterogeneity within individual trajectories [27, 89, 170], suggesting local variations in the media. Thus, spatiotemporal varying diffusivities [21, 89, 90] or heterogeneous diffusion processes could occur [12, 19]. Since living systems are far from equilibrium, the ambient active noise exerted by intracellular structures could act as a driving force of heterogeneous diffusion. However, the fundamental question of how a distribution of apparent transport coefficients, i.e. diffusing diffusivities emerges in the first place remains undetermined.

In summary, it is neither clear (i) which mechanism regulates the values of anomaly exponents α, nor (ii) how heterogeneous (sub)diffusion might emerge in an active environment due to non-specific interactions.

4.2. MSD, anomaly exponents and generalized transport coefficients

To explore the heterogeneous subdiffusion of tracers in the cellular environment, quantum dots were introduced into the cytoplasm of HeLa cells as described before. The particles motion has been tracked and the MSD, anomaly exponent α, and generalized transport coefficient K_α have been quantified as stated in Sec.3.2.

Establishing the evaluation method, control experiments of quantum dots in highly, but purely **viscous artificial fluids** as introduced in Sec.2.3 were quantified first. To this end pure glycerol with a viscosity $\eta = 1\,\mathrm{Pa\,s}$, and aqueous sucrose solution ($\eta = 50\,\mathrm{mPa\,s}$) were used. In both cases vanishing anomalies were observed. The PDFs of α obtained by the bootstrapping approach with their respective mean values $\langle\alpha_\mathrm{G}\rangle = 1.01 \pm 0.04$ (glycerol, dashed black line) and $\langle\alpha_\mathrm{S}\rangle = 0.97 \pm 0.05$ (sucrose solution, dashed red line) are shown in Fig.4.1**(a)**. Solid lines are best Gaussian fits to the obtained data displayed as red circles (glycerol) and black diamonds (sucrose). The mean value $\langle\alpha\rangle$ for sucrose solution is slightly lower than for glycerol, nevertheless both conditions show essentially normal diffusion. Representative TA-MSDs of SPT experiments on quantum dots in glycerol are shown in Fig.4.1**(b)** with grey lines. Note that almost all curves follow the anticipated linear scaling $\langle\mathrm{MSD}(\tau)\rangle_t \propto \tau$ in the double logarithmic plotting. The ensemble average $\langle r^2(\tau)\rangle_{\mathrm{t,E}}$ is shown in red. Since TA-MSDs show linear scaling for all time lags τ and the scaling neither over nor under shoots in the small time lag regime $\tau < 2\Delta t$, no significant offsets are observable in the measurements. It was thus assumed that dynamic and static offsets canceled each other out during experiments.

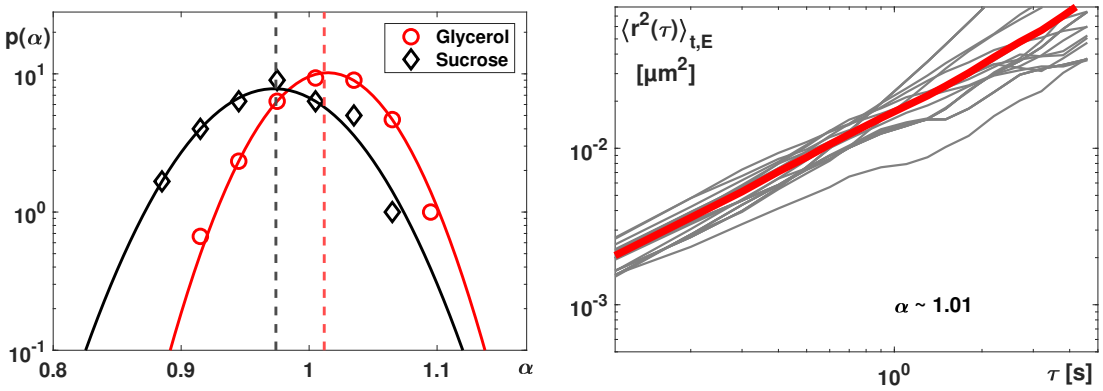

(a) PDF of anomaly exponents

(b) Time-averaged MSD

Figure 4.1: **(a)** Probability density function of α obtained via SPT in artificial, highly viscous fluids. **Red:** 100% glycerol ($\eta \approx 1\,\mathrm{Pa\,s}$) with $\langle\alpha\rangle = 1.01 \pm 0.04$ (dashed line). **Black:** 60% per weight sucrose solution ($\eta \approx 50\,\mathrm{mPa\,s}$) with $\langle\alpha\rangle = 0.97 \pm 0.05$ (dashed line). Full lines are best Gaussian fits to the data. **(b)** Representative time-averaged MSDs (grey lines) of quantum dots diffusing in glycerol shown in double logarithmic scaling. Individual curves as well as the ensemble average $\langle r^2(\tau)\rangle_{\mathrm{t,E}}$ (red line) show the anticipated linear scaling: $\langle\mathrm{MSD}(\tau)\rangle_t \propto \tau$.

Bead loading quantum dots into the cytoplasm of **untreated HeLA cells** was performed to get a reference to all upcoming experimental conditions. To this end, a grand total of 83 cells were used from which 4887 trajectories with $N \geq 100$ positions and 631 trajectories with $N \geq 500$ positions were extracted. Trajectories were subsequently limited to $N = 100$ and $N = 500$ positions respectively. The time series whose TA-MSD grew less than $\sim \tau^{0.075}$ or whose $\langle \mathrm{MSD}(\tau = 1s) \rangle \leq 1{\times}10^{-3}\,\mu\mathrm{m}^2$ were rated immobile and were hence discarded from the following analysis. Throughout the entire manuscript, bin sizes of probability density functions have been chosen to obey Scott's rule. The PDFs of anomaly exponents α obtained from untreated cells for different evaluation approaches are shown in Fig.4.2. Here the representative cases of short trajectories ($N = 100$) is depicted. The resulting raw TA-MSD fitting data, depicted as grey histogram, showed considerable trajectory-to-trajectory fluctuations with a mean value around $\langle \alpha \rangle = 0.59$. Employing the bootstrapping approach (see Sec.3.2.2) using an arithmetic average (red circles) supplied narrower width of the distribution but resulted in a constant shift in the mean value to $\langle \alpha \rangle = 0.79$ (dashed red line). Bootstrapping with geometric averaging (black diamonds) on the other hand resulted in a narrower PDF and retained the mean value $\langle \alpha \rangle = 0.58$ (dashed black line) within experimental uncertainty. This observation holds true for all PDFs of diffusion anomalies as shown in Table 1. Thus, the bootstrapped data with geometrical average was used in all further analysis and discussion.

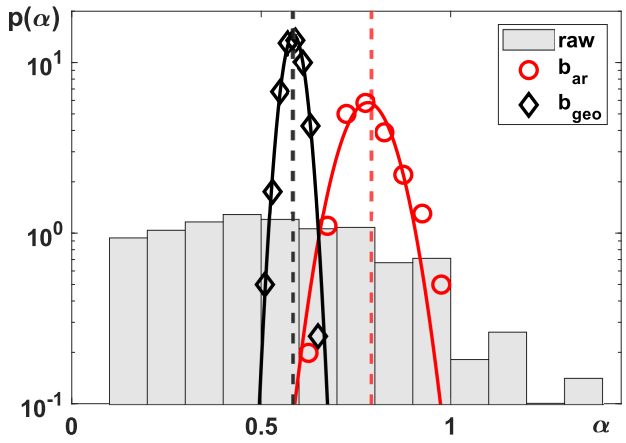

Figure 4.2: The PDF of anomaly exponents α obtained from individual TA-MSDs ($N = 100$) from untreated cells for different evaluation approaches. The raw TA-MSD fitting (grey histogram) shows a broad variation around a mean $\langle \alpha \rangle = 0.59$ (dashed grey line, obscured by the dashed black line). Bootstrapping the data with arithmetic averaging (red circles) reveals a constant over-estimation with mean value $\langle \alpha \rangle = 0.79$ (dashed red line), whereas employing the geometrical average during bootstrapping retrieved $\langle \alpha \rangle = 0.58$ as mean value (dashed black line). Note that the latter will be used as reference in all further discussion. Full lines are best Gaussian fits to the bootstrapped data.

Since SPT experiments on quantum dots were performed under different experimental conditions, i.e. on different microscope setups, the results observed under these different conditions have to be cross checked to varify their validity. To this end, **reference measurements** were done and compared to the results obtained for untreated cells (see Fig.4.2, black). To begin with, the influence of the drug DMSO on the diffusion of quantum dots inside the cytoplasm as used in the protocols described in Sec.2.3 was investigated. For this reason, quantum dots were tracked in cells treated with pure DMSO. A total of 228 trajectories ($N = 100$) were acquired from five cells and their mean anomaly was calculated to be $\langle\alpha\rangle = 0.65$ which is slightly higher than the value obtained for untreated cells. The PDF of anomalies is shown in Fig.4.3 color coded red. The width of the distribution is about the same size, with standard deviations being less than $\sigma \leq 0.03$ for the wide field reference (grey histogram) and the DMSO control (red circles) respectively. As an additional reference, quantum dots were tracked again in untreated cells using a laser scanning microscope (LSM) as described in Sec.2.5. 366 trajectories were extracted from 42 cell experiments from which a mean anomaly $\langle\alpha\rangle = 0.60$ was obtained. The PDF of these measurements are shown in Fig.4.3 with black diamonds. The variations experienced within the experiments were slightly higher compared to the previous data, resulting in an increased standard deviation $\sigma = 0.05$. Nevertheless, the mean values (dashed lines) are all in reasonable agreement with the reference.

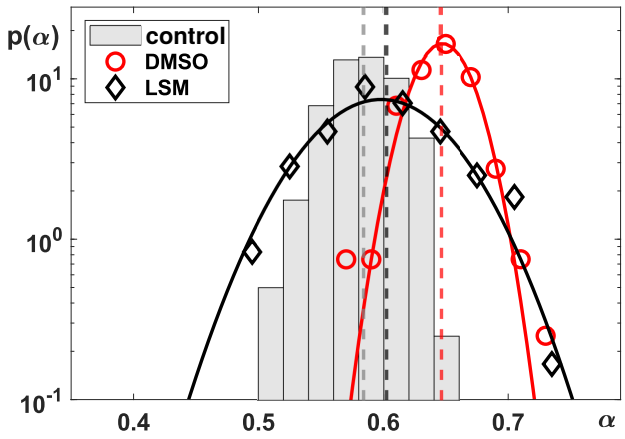

Figure 4.3: The PDF of anomaly exponents α obtained from individual TA-MSDs ($N = 100$) from different reference experiments. All measurements show a similar mean value $\langle\alpha\rangle \approx 0.6$. The grey histogram shows the PDF obtained from untreated cells & a TIRF microscope in wide field mode (control). The PDF obtained from cells treated with pure DMSO solvent without any additional drugs is shown with red circles. Measurements performed on untreated cells on a laser scanning microscope are depicted with black diamonds. Mean values are indicated by dashed lines with respective color coding. Full lines are best Gaussian fits.

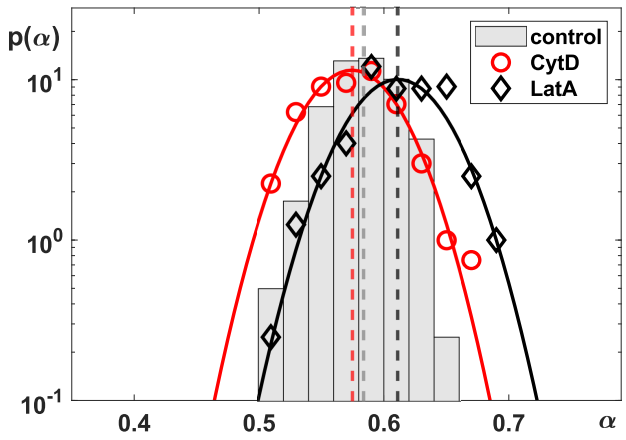

Figure 4.4: The PDF of anomaly exponents α obtained from individual TA-MSDs ($N = 100$) from experiments were actin breakdown was performed with *cytocalasin D* (CytD, red circles) or *latrunculin A* (LatA, black diamonds) respectively. Mean values (dashed lines with respective color coding) $\langle\alpha\rangle \approx 0.6 \pm 0.03$ show no significant variation across all three conditions.

Next, the motion of tracer particles in the cytoplasm of cells where actin filaments were disrupted with the aid of either ***cytocalasin D*** or ***latrunculin A*** as described earlier, was studied to find cues to the potential influence of intermediate filaments on the sub-diffusion of tracers. Fig.4.4 shows the PDF of diffusion anomalies for these two conditions in comparison to the control data presented before. In total, $n = 49$ (CytD) and $n = 75$ (LatA) cells were used from which 2968 & 3997 trajectories ($N = 100$), and 444 & 517 trajectories ($N = 500$) were extracted, respectively. The threshold values mentioned before were used again to rule out immobile quantum dots. The mean anomalies, as indicated again with dashed lines, were found to be $\langle\alpha\rangle = 0.58 \pm 0.03$ for CytD treated cells and $\langle\alpha\rangle = 0.61 \pm 0.04$ in cells where actin was depolymerized with LatA. Table 1 summarizes the results for trajectories with a minimum length $N = 100$ for better comparison.

Following the disruption of actin filaments, ***nocodazole*** was used to depolymerize the microtubular cytoskeleton as described in Sec.2.1.3. MTs are stiffer and larger in size, compared to actin filaments, thus perturbations of their integrity presumably influences the environment on a larger scale. Using this experimental condition, 4887 trajectories with at least $N = 100$ positions and 631 trajectories of length $N = 500$ could be extracted from 83 individual cells. The respective probability density function of diffusion anomalies extracted from trajectories with $N = 100$ positions is shown in Fig.4.5 as red circles. Its mean value $\langle\alpha\rangle = 0.45$ (dashed red line) is significantly lower compared to the reference experiments (grey histogram). However, the width of the distribution is once again in the same order of magnitude compared to the reference data shown as grey histogram.

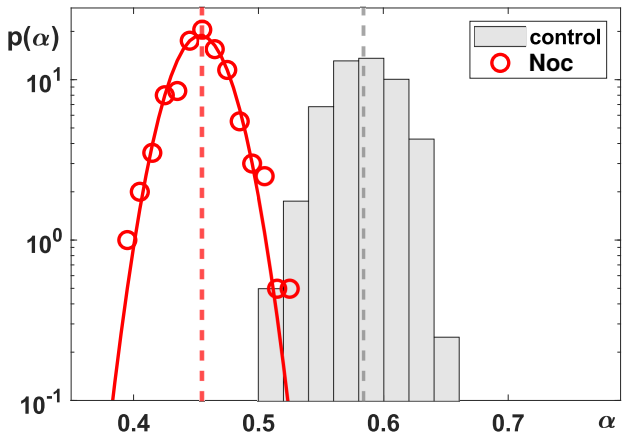

Figure 4.5: The PDF of anomaly exponents α obtained from the bootstrapping approach of power-law fits on individual TA-MSDs ($N = 100$) from cells with depolymerized MT network using Noc (red). Its mean value was found to be $\langle\alpha\rangle = 0.45$ which is significantly lower than the reference data (grey histogram). The full red line is the best Gaussian fit to the data.

All $\langle\alpha\rangle$ values for bootstrapped and raw data extracted from short trajectories ($N = 100$) of cells where the cytoskeleton breakdown was achieved either with *cytocalasin D* or *latrunculin A*, or *nocodazole* are summarized in Table 1.

	untreated	Noc	CytD	LatA
$\langle\alpha\rangle_{\text{raw}}$	0.59	0.45	0.58	0.61
$\langle\alpha\rangle_{\text{geom}}$	0.58	0.46	0.58	0.61
$\langle\alpha\rangle_{\text{arith}}$	0.79	0.66	0.82	0.86

Table 1: Mean anomaly exponents $\langle\alpha\rangle$ for trajectories ($N = 100$) in untreated cells and after cytoskeletal breakdown obtained with raw power-law TA-MSD fitting and bootstrapping (geometric and arithmetic) respectively. Standard errors were in all cases < 0.02.

Studying the influence of trajectories length on the observed motion, the PDFs of anomalies extracted from bootstrapped data with geometrical averaging from longer trajectories ($N = 500$) was compared to the data found for short trajectories. The PDFs of anomaly exponents for data acquired using untreated cells and cells where MT breakdown was done are shown in Fig.4.6 for both short (grey and red histograms) and long trajectories (black circles and red diamonds) as representative samples. In all cases, a shift to smaller mean values was observed whereas the shape of the distribution remained the same. However, the shift to lower anomaly exponents was significantly more pronounced for trajectories where cells were treated with nocodazole as presented in Table 2.

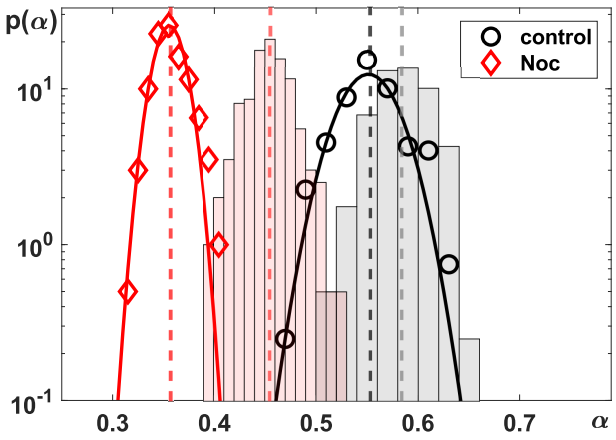

Figure 4.6: The PDF of anomaly exponents α obtained from the bootstrapping approach of power-law fits on individual TA-MSDs of longer trajectories ($N = 500$) from cells with depolymerized MT network using Noc (red diamonds) and untreated cells (black circles). The respective PDFs of the data extracted from shorter trajectories ($N = 100$) is shown as red and grey histograms as a reference. The values $\langle\alpha\rangle$ found for longer trajectories shift to smaller values independent of the treatment.

	untreated	Noc	CytD	LatA
$\langle\alpha\rangle_{\text{raw}}$	0.55	0.36	0.54	0.58
$\langle\alpha\rangle_{\text{geom}}$	0.55	0.36	0.54	0.57
$\langle\alpha\rangle_{\text{arith}}$	0.60	0.43	0.73	0.76

Table 2: Mean anomaly exponents $\langle\alpha\rangle$ for trajectories ($N = 500$) in untreated cells and after cytoskeletal breakdown obtained with raw power-law TA-MSD fitting and bootstrapping (geometric and arithmetic) respectively. Standard errors were in all cases < 0.02.

Comparing the different conditions for the cytoskeleton breakdown, representative geometrical averaged TA-MSDs from trajectories with $N = 100$ positions used for the bootstrapping approach are shown in Fig.4.7 as grey lines. The ensemble- and time-averaged MSD $\langle r^2(\tau)\rangle_{\text{t,E}}$ (red) approximately shows the anticipated scaling according to Table 1. Localization errors, i.e. buckling of the curves and thus a change in scaling, were not observed for individual trajectories at small lag times τ for neither of the presented conditions in Fig.4.7. However, time-averaged MSDs of individual trajectories show recognizable fluctuations, resulting in broadened distributions of anomaly exponents.

As stated earlier, experiments where the ER of HeLa cells was disrupted using the drug **filipin** or by applying **hypotonic pressure** were recorded on a LSM setup, yielding 295 and 81 trajectories of length $n = 100$ from 62 and 23 individual cells, respectively. Due to

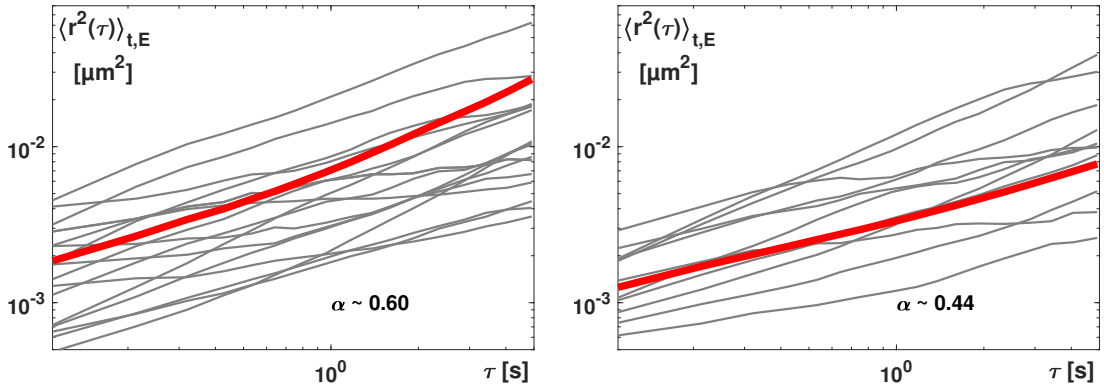

(a) Untreated cells (control)

(b) Nocodazole

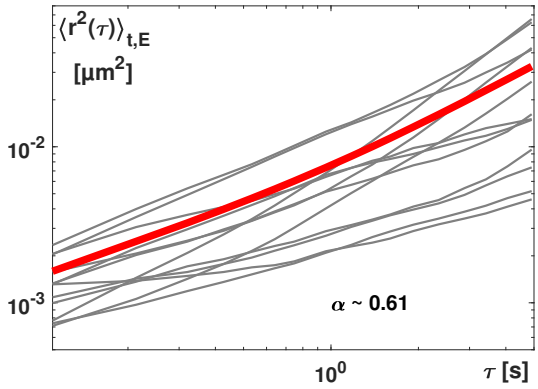

(c) Cytocalasin D

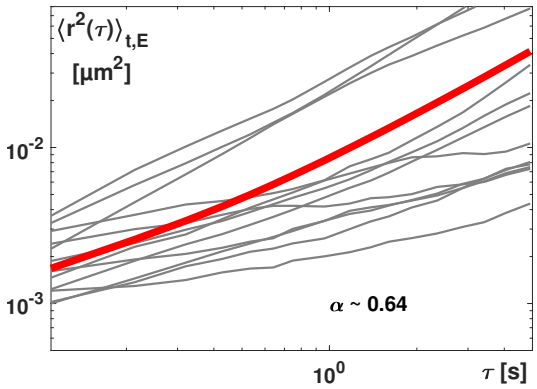

(d) Latrunculin A

Figure 4.7: Representative geometrical and time-averaged MSDs (grey lines) from trajectories with $N = 100$ positions used in the bootstrapping approach shown in double logarithmic scaling. No localization errors are observed at small lag time τ in **(a)** untreated, **(b)** nocodazole ,**(c)** cytocalasin D, or **(d)** latrunculin A treated cells. Individual curves show scaling distributed around the ensemble average $\langle r^2(\tau)\rangle_{\mathrm{t,E}}$ (red line), which shows the anticipated scaling: $\langle \mathrm{MSD}(\tau)\rangle_t \approx \tau^\alpha$ given in Table 1. The anomaly exponents from fitting the ensemble-averaged data is given as an inset.

cellular background fluorescence and the lower pixel integration time as compared to the camera-based tracking (see Sec.2.5), a significant positive offset was observed in individual time-averaged MSDs at small times, rendering the simple averaging and bootstrapping approach inappropriate for evaluation of the acquired data. Thus, a recently introduced and validated, more sophisticated resampling approach as introduced in [178] was used. The main advantage of the approach is that static localization errors do not interfere with extracting a meaningful average scaling exponent $\langle\alpha\rangle$ from resampled time average MSD data. To begin with, the usual TA-MSD, $\langle \mathrm{MSD}(\tau)\rangle_t$ with $\tau/\Delta t \in \mathbb{N}^+$ is calculated for every individual trajectory $\mathbf{r}_i(j\Delta t)$ with $j = 1, ..., N$. Subtracting the first value of each TA-MSD yields the quantity $v(\tau, \Delta t) = \langle r^2(\tau)\rangle_t - \langle r^2(\Delta t)\rangle_t$. When considering the even or odd positions of a specific trajectory only, two individual TA-MSDs with lag times

$\tau/\Delta t = 2, 4, ...$ could be calculated from the $N/2$ positions. Subsequent averaging of these two TA-MSDs and subtracting the first value yielded a new quantity: $v(\tau, 2\Delta t)$. Taken into account that

$$v(\tau, k\Delta t) = k^{\alpha} \cdot v(\tau, \Delta t), \tag{4.1}$$

the ratio of these functions can be calculated and thus $\langle\alpha\rangle$ can be extracted without fitting [178]:

$$\langle\alpha\rangle = \frac{1}{\log(2)} \left\langle \log\left(\frac{\langle v(\tau, 2\Delta t)\rangle_{\mathrm{g}}}{\langle v(\tau, \Delta t)\rangle_{\mathrm{g}}} \right) \right\rangle_{\tau}. \tag{4.2}$$

In the equation above, $\langle ... \rangle_{\mathrm{g}}$ indicates geometrical averaging over individual trajectories and $\langle ... \rangle_{\tau}$ denotes averaging over lag times $\Delta t \leq \tau \leq 10\Delta t$. As a control, the approach was applied to the camera based tracking data for trajectories of length $N = 100$ in untreated cells and in cells treated with nocodazole. Both controls confirmed the mean anomaly exponents of $\langle\alpha\rangle = 0.6$ and $\langle\alpha\rangle = 0.4$ within the given uncertainty compared to the results presented in Table 1, respectively. Evaluating tracking data for untreated cells gathered from confocal laser scanning image series yielded a slightly elevated value $\langle\alpha\rangle = 0.68$. These deviations are supposedly due to the measurement technique or potential cell batch variations. Time-averaged MSDs from cells treated with filipin and hypotonic pressure (osmotic shock) showed mean anomaly exponents that were overall consistent with untreated cells with tendencies to lower ($\langle\alpha\rangle = 0.59$) and slightly elevated ($\langle\alpha\rangle = 0.72$) values, respectively. All extracted mean anomaly exponents from the resampling approach are listed in Table 3.

Next to the mean anomaly exponent as presented before, the **generalized transport coefficients** K_{α} were extracted from time-averaged MSDs by a simple power-law fit to $\langle \mathrm{MSD}(\tau)\rangle_t = K_{\alpha}\tau^{\alpha}$ as stated in Sec.3.2.

As before, beginning with the most basic experimental environment, simple, artificial, highly viscous fluids were analyzed. Since these data showed normal diffusion, the diffu-

	untreated	Noc	filipin	osmotic shock
$\langle\alpha\rangle_{\mathrm{geom}}$	0.58 (0.61)	0.45	/	/
$\langle\alpha\rangle_{\mathrm{resample}}$	0.59 (0.68)	0.39	0.59	0.72

Table 3: Mean anomaly exponents extracted from the resampling approach for untreated (untreated: confocal image series), nocodazole-, filipin-treated, and osmotic-shocked cells. The resampling approach confirmed the results presented before, thus it is a trustworthy measure in itself. The slightly increased values for untreated cells are mostly likely due to cell batch variations (e.g. different passage numbers). Anomalies could not be extracted with the bootstrapping approach for filipin and hypotonic pressure data, due to static offsets in the TA-MSDs for small lag times τ. Standard errors were in all cases smaller than 0.02.

sion constant D instead of the generalized transport coefficient was extracted according to $\langle \mathrm{MSD}(\tau)\rangle_t = 4D\tau$. The extracted data for measurements in pure glycerol and 60% per weight aqueous sucrose solution are shown in Fig.4.8. The PDFs of the diffusion constants $p(D)$ obtained from trajectories of length $N = 100$, roughly have a lognormal shape. Since this distribution has a positive skewness, the mean value is not an appropriate measure, hence for comparison, the median values $\tilde{D}$, indicated by dashed lines, were used. The diffusion constant of quantum dots diffusing in 100% glycerol was estimated to be $\tilde{D} = 17{\times}10^{-3}\mu\mathrm{m}^2/\mathrm{s}$, which is in good agreement with previous results [165]. The same quantum dots diffusing in aqueous sucrose solution have a median transport coefficient of at least one order of magnitude higher, $\tilde{D} = 260{\times}10^{-3}\mu\mathrm{m}^2/\mathrm{s}$. Note that both artificial fluids discussed in this work show normal diffusion characterized by $\alpha = 1$. In contrast, all experimental data extracted from live cell imaging showed marked subdiffusion. Therefore, the generalized transport coefficient K_α had to be used to characterize the transport behavior. The PDF of generalized transport coefficients extracted from untreated cells is shown in Fig.4.9 as a grey histogram. The respective median value, indicated by a dashed line, was found to be $\tilde{K_\alpha} = 10{\times}10^{-3}\mu\mathrm{m}^2/\mathrm{s}^\alpha$.

Furthermore, in Fig.4.9 the PDFs of generalized transport coefficients obtained from trajectories ($N = 100$) of cells treated with different drugs are shown. Panel **(a)** shows actin filament depolymerization and MT breakdown. All distributions show the lognormal shape

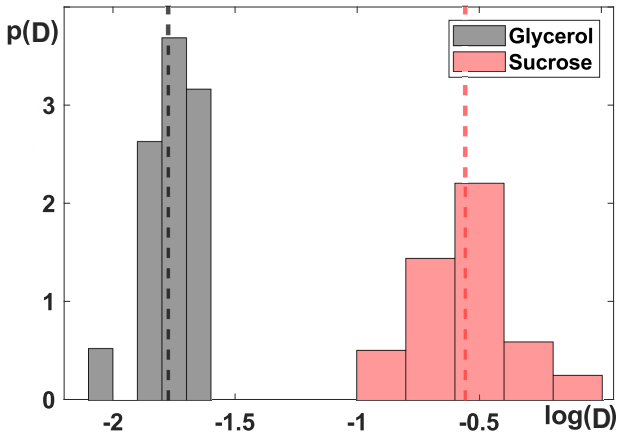

Figure 4.8: PDFs of diffusion constants obtained from trajectories of length $N = 100$ of quantum dots diffusing in different artificial environments (semi-logarithmic plotting). The distributions roughly have a lognormal shape (histograms), with their respective median $\tilde{D}$ indicated as dashed lines. **(a)** highly viscose artificial fluids: 100% glycerol (grey, $\tilde{D} = 17{\times}10^{-3}\mu\mathrm{m}^2/\mathrm{s}$) and 60% per weight aqueous sucrose solution (red, $\tilde{D} = 260{\times}10^{-3}\mu\mathrm{m}^2/\mathrm{s}$). Note that both artificial fluids show normal diffusion, hence $\alpha = 1$ and fitting was done according to $\langle \mathrm{MSD}(\tau)\rangle_t = 4D\tau$.

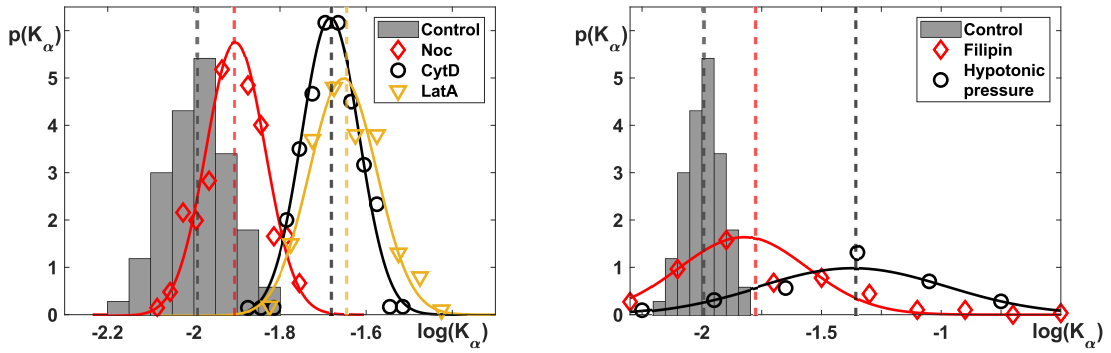

(a) Cytoskeleton breakdown **(b)** ER disruption

Figure 4.9: PDFs of generalized transport coefficients obtained from trajectories of length $N = 100$ of quantum dots in cells where **(a)** the actin filaments or MT were depolymerized, and **(b)** ER was disrupted. Grey histograms show data extracted from untreated cells. Dashed lines indicate median values. Solid lines are best Gaussian fits to the logarithmic data.

observed before in control experiments. Actin breakdown with cytocalasin D (black circles) and latrunculin A (yellow triangles) resulted in approximately the same median values of $\tilde{K_\alpha} = 21{\times}10^{-3}\mu m^2/s^\alpha$ and $\tilde{K_\alpha} = 23{\times}10^{-3}\mu m^2/s^\alpha$, whereas MT breakdown with nocodazole (red diamonds) resulted in a slightly lower median values $\tilde{K_\alpha} = 13{\times}10^{-3}\mu m^2/s^\alpha$. Nevertheless, all values are close to the one observed in untreated cells and only show slight deviations in width of the distribution. On the other hand, disruption of the ER network resulted in broader changes (see Fig.4.9**(b)**). Even if the median value of generalized transport coefficients extracted from cells treated with filipin (red diamonds) $\tilde{K_\alpha} = 24{\times}10^{-3}\mu m^2/s^\alpha$ is comparable to the values found before, the width of the PDF is at least one order of magnitude higher. The same holds true for measurements in with hypotonic pressure treated cells (black circles). In fact, the changes in the latter are even more drastic, since not only the width, but the median value $\tilde{K_\alpha} = 60{\times}10^{-3}\mu m^2/s^\alpha$ shows significant deviations from the control data (grey histogram).

Representative data on the dependency of generalized transport coefficients on the length of the acquired trajectories is shown in Fig.4.10. Data acquired from trajectories with

	untreated	Noc	CytD	LatA	Filipin	Osmotic shock
$\tilde{K_\alpha}$	10	13	21	23	24	60
σ_{K_α}	2	2	3	4	30	50

Table 4: Generalized transport coefficient (median) $\tilde{K_\alpha}$ and corresponding standard deviations of all experimental conditions. All quantities are in units of $[1{\times}10^{-3}\mu m^2/s^\alpha]$.

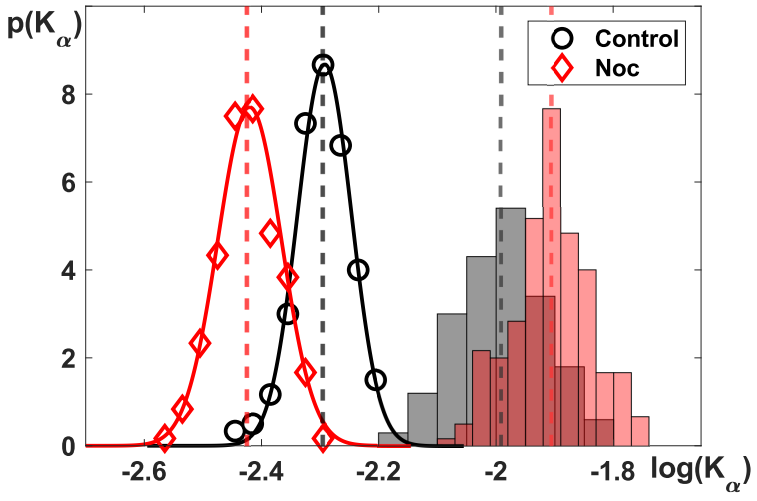

Figure 4.10: Representative PDFs of the generalized transport coefficients K_α, obtained by the bootstrapping approach from short trajectories $N = 100$ (histograms) and long trajectories $N = 500$ (symbols) of untreated (black) and nocodazole-treated cells (red). A significant shift to lower K_α was observed for all longer trajectories regardless of the applied treatment.

$N = 100$ positions is shown as grey and red histograms (untreated cells and MT breakdown with nocodazole). Full lines show best Gaussian fits to logarithmic data from trajectories with $N = 500$ positions (black circles and red diamonds, respectively). A significant apparent shift to lower K_α was observed for all conditions. A shift in generalized diffusion coefficients depending on the length of the trajectory segments was also observed prior by Ernst and Köhler [179]. For untreated cells, the median value was reduced to $\tilde{K_\alpha} = 5{\times}10^{-3}\mu m^2/s^\alpha$. However, nocodazole-treated cells showed an even more pronounced shift to $\tilde{K_\alpha} = 4{\times}10^{-3}\mu m^2/s^\alpha$.

In conclusion, the mean anomaly exponent as well as the generalized transport coefficient of quantum dots depend on the respective environment they are measured in. In artificial fluids, trajectories showed the anticipated linear scaling $\alpha \approx 1$, whereas tracers in the cytoplasm of HeLa cells showed marked subdiffusion. In untreated cells, the diffusion anomaly was found to be $\alpha \approx 0.6$ and the generalized transport coefficient was $K_\alpha \approx 15{\times}10^{-3}\mu m^2/s^\alpha$. Both results are in favorable agreement with previous studies [6, 22, 30, 62]. Disruption of intermediate filaments did not significantly change the observable measures. When depolymerizing the microtubular network however, a significant shift to more pronounced subdiffusion with $\alpha \approx 0.45$ was observed, while K_α did not show substantial changes. Neither filipin nor hypotonic pressure treatment – both utilized to disrupt the ER network – resulted in significant deviations from anomaly exponents seen in untreated cells. Nevertheless, their respective distribution of generalized transport coefficient showed drastic

changes. In both cases, median values shifted to higher mobility while the width of $p(K_\alpha)$ increased by at least one order of magnitude. When comparing results gained from short and long trajectories with $N = 100$ and $N = 500$ positions, respectively, a significant apparent shift to lower mobilities as well as a slight decrease in anomaly exponents was observed. Supposedly, a lower K_α facilitates the acquisition of longer trajectories, hence slightly biasing the data.

4.3. The velocity autocorrelation function

Going beyond the MSD, the ensemble-averaged velocity autocorrelation function (VACF) was analyzed for a variety of different experimental conditions as presented in Sec.3.3. Validation of the method was done using the SPT data for artificial fluids that showed normal diffusion. The ensemble-averaged normalized and rescaled VACF of all trajectories with $N = 50$ at $\delta t = k\Delta t$ with $k = [1, 3, 5]$ for quantum dots undergoing free diffusion in pure glycerol (black) and 60% per weight aqueous sucrose solution (red) is shown in Fig.4.11. Note that for better visibility the sucrose data was shifted upwards (+0.5). The full lines are the analytical predictions according to Eq.3.11 where mean anomalies were set to the values found in the bootstrapping approach (see Fig.4.1). Both functions show

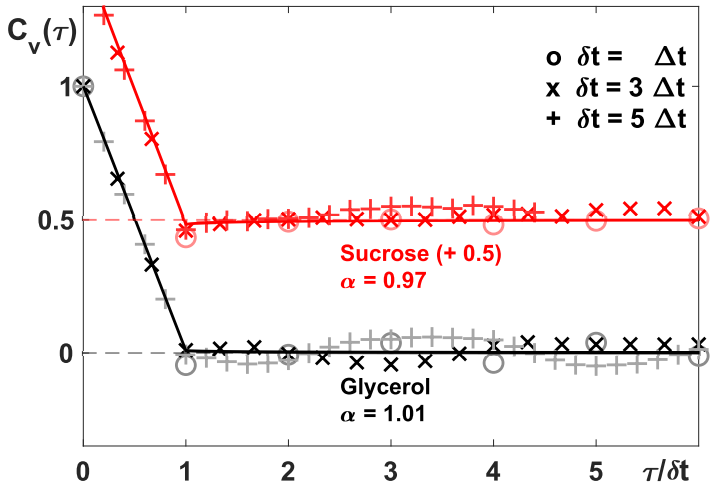

Figure 4.11: Rescaled and normalized VACF of all experimental trajectories with $N = 50$ at different δt for artificial fluids (pure glycerol: black, sucrose solution: red) in which tracers show normal diffusion. For better visibility the sucrose data have been shifted upwards. Full lines are analytical predictions according to Eq.3.11 with α set to the value shown. Both VACF agree with the anticipated prediction and do not show any significant correlation for $\tau \geq \delta t$. Dashed lines correspond to no correlation as guide to the eye.

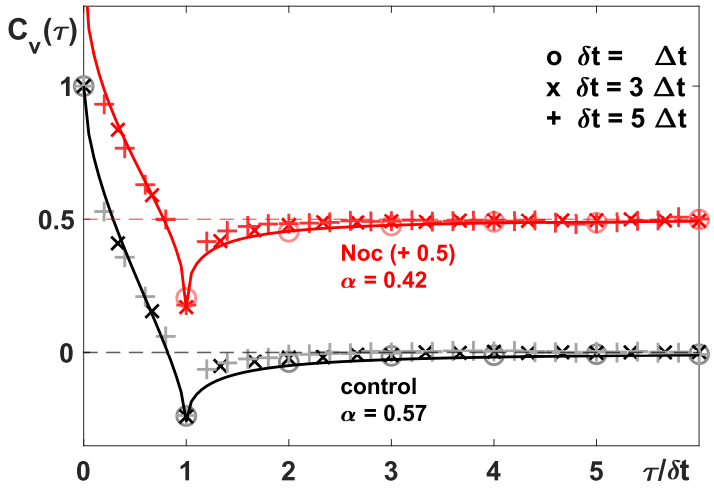

Figure 4.12: Rescaled and normalized VACF of all experimental trajectories with $N = 100$ positions at different δt for untreated cells (black) and cells where MT breakdown was achieved using nocodazole (red). For better visibility the Noc data have been shifted upwards. Full lines are analytical predictions according to Eq.3.11 with α set to the value shown. Both VACF show the for antipersistent fBM anticipated anti-correlation for lag times $\tau \gtrapprox \delta t$ with quick decay to no correlation (dashed lines) for longer lag times.

the anticipated decay until $\tau = \delta t$, after which no significant correlation was observed. Dashed lines are guides to the eye and correspond to no correlation ($C_v = 0$). Fluctuation for longer lag times are prone to unsatisfying statistics.

Looking at the VACF for experimental conditions that did not show normal diffusion when analyzing the mean anomalies, an overall remarkable agreement of the experimental data with the analytical prediction for fBM (Eq.3.11) without any fitting parameter was observed. In Fig.4.12 the results are presented for trajectories extracted from untreated cells (black) and cells where microtubules have been broken down using nocodazole (red). The respective normalized and rescaled VACFs are shown for three different time lags $\delta t = (1, 3, 5)\Delta t$, all of which showed decreasing correlation for $\tau < \delta t$ followed by a distinct negative dip at $\tau = \delta t$ for all conditions. Subsequently, (anti-)correlation decayed and eventually reached $C_v = 0$ for long lag times. The same behavior was observed when intermediate filaments were disrupted as shown in Fig.4.13**(a)**. Again, the prominent dip at $\tau = \delta t$ with subsequent decay of (anti-)correlation in experimental data is in excellent agreement with Eq.3.11. For data of untreated cells acquired at a laser scanning microscope (Fig.4.13**(b)**, red), however, the decay to no correlation for $\tau > \delta t$ was observed to be much more rapid. Nevertheless, a prominent dip in correlation was observed when analyzing this data as well.

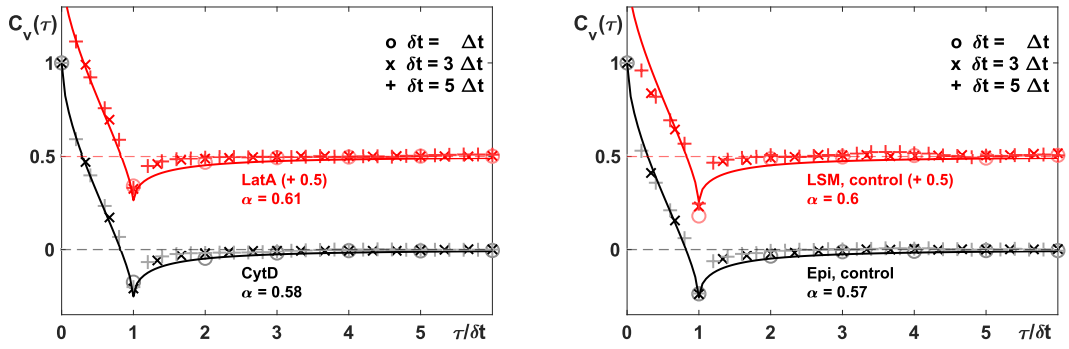

(a) Actin filament breakdown **(b)** Control vs. LSM (untreated cells)

Figure 4.13: Rescaled and normalized VACF of experimental trajectories with length $N = 100$ at different δt for **(a)** actin breakdown with cytocalasin D (black) and latrunculin A (red), and **(b)** untreated cell measured in epifluorescent mode (black) and using an LSM (red). For better visibility, LatA data and LSM data have been shifted upwards (+0.5). All VACF agree with their analytical prediction for fBM (Eq.3.11, full lines) with α set to the corresponding values shown in the figure. Dashed lines correspond to no correlation as guide to the eye.

Adding up, the data did show decaying correlation for any tested time lag δt prior to $\tau < \delta t$, however no correlation whatsoever was observed for lag times $\tau \geq \delta t$ for diffusion of quantum dots in artificial fluids. On the other hand, the ensemble- and time-averaged VACF showed significant anti-correlation for all data extracted from live cell imaging, regardless of the applied treatment. This data was in almost all cases very well described by the analytical prediction formulated in Eq.3.11 with the corresponding anomaly exponents set to the values found by the bootstrapping approach.

4.4. The statistics of normalized increments

Following the analysis presented in the previous sections, the PDF of normalized increments χ within a certain time lag δt was inspected. Therefore, time series were calculated and normalized by their respective individual root-mean-square displacement as described in Sec.3.4. Since systematic differences were neither observed nor expected between spatial directions in experiment, all normalized increments were combined into one single set of χ for each individual experimental condition. When assuming homogeneous (fractional) Brownian motion of the tracer particles, their PDF of normalized increments $p(\chi)$ was expected to follow a Gaussian. In Fig.4.14**(a)** the PDF of normalized increments from trajectories with $N = 50$ positions acquired from SPT measurements in artificial, viscose fluids (both glycerol and sucrose solution combined) for a time lag $\delta t = \Delta t$ is shown (black crosses). A normalized Gaussian distribution, indicated with a red line, describes the data

for small and large increments χ alike. Note that the combination of pure glycerol and 60% sucrose solution data and the reduction to $N = 50$ positions in single trajectories was done to achieve better statistics.

When analyzing measurements done in untreated cells for short time lags $\delta t < 3\Delta t$ as shown in Fig.4.14**(b)** & **(c)**, the PDF of normalized increments χ followed the anticipated Gaussian (red line) for small χ but showed significant deviations for larger increments. In fact, larger increments seemed to be overrepresented in these measurements hinting towards an increased mobility in some parts of the underlying mechanisms and thus a somewhat heterogeneous random walk process governing each individual trajectory. For

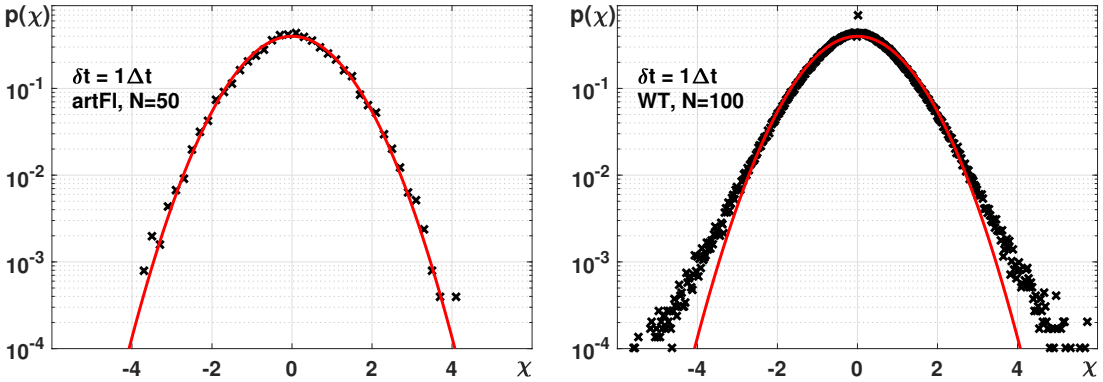

(a) Artificial fluids: pure glycerol & 60% sucrose solution ($\delta t = \Delta t$)

(b) Untreated cells ($\delta t = \Delta t$)

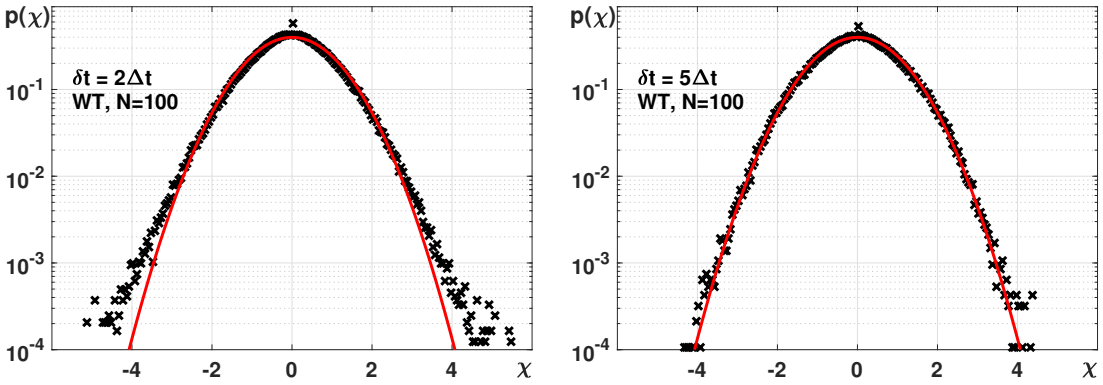

(c) Untreated cells ($\delta t = 2\Delta t$)

(d) Untreated cells ($\delta t = 5\Delta t$)

Figure 4.14: **(a)** The PDF of normalized increments χ from quantum dot trajectories with $N = 50$ positions tracked in artificial fluids for time lag $\delta t = \Delta t$ (black crosses) follows the anticipated Gaussian (red line) for all increments. The combination of pure glycerol and 60% sucrose solution data was done to achieve better statistics. **(b)** – **(d)** Respective PDFs of χ for trajectories ($N = 100$) of untreated cells and increasing time lag $\delta t = k\Delta t$ with $k = [1, 2, 5]$. For short time lags (**(b)**,**(c)**), the data followed the anticipated Gaussian (red line) for small χ but showed significant deviations at larger χ, suggesting some kind of heterogeneity in the random walk process. **(d)** For longer time lags ($\delta t = 5\Delta t$), the experimental data followed a Gaussian for all χ, i.e. observed deviations have subsided due to CLT.

longer time lags $\delta t = 5\Delta t$, the experimental data retrieved the Gaussian for all normalized increments as shown in Fig.4.14**(d)**, due to the central limit theorem.

To probe for potential interference of actin filaments or microtubules as causes of the heterogeneity in the random walk of inserted quantum dots, the PDFs of normalized increments of trajectories with $N = 100$ extracted from cells where cytoskeleton breakdown was achieved using either Noc, CytD, or LatA are shown in Fig.4.15. All conditions were evaluated with a combination of all spatial directions while using a time lag of either $\delta t = \Delta t$ (left panels) or $\delta t = 5\Delta t$ (right panels) to emphasize deviations. For all conditions tested, the PDFs of normalized increments showed strong deviations from a Gaussian shape for small time lags. Especially long increments seemed to be overrepresented once again, independent of the cytoskeletons integrity as seen by the pronounced 'wings' of the distributions (left panels). Interestingly, the magnitude of the deviations seemed to be independent of the applied treatment as well. For time lags $\delta t = 5\Delta t$ (right panels), all distributions regain their anticipated Gaussian shape indicated with a red line. This finding is in good agreement with the anticipation, since all processes should eventually be normally distributed due to the CLT.

Following the breakdown of the cytoskeleton, the impact of disruption of another crucial cell organelle, i.e. the endoplasmic reticulum, was studied. To this end, the ER was fragmented either with the aid of the drug filipin or using a hypotonic pressure protocol as described in Sec.2.1.4. The respective PDFs of increments χ are shown in Fig.4.16. In contrast to the PDFs for short time lags $\delta t = \Delta t$ in cells with perturbed cytoskeleton, disruption of ER showed less pronounced 'wings' in $p(\chi)$ for both conditions. The distributions of normalized increments seemed to fit the anticipated Gaussian shape (red line) for almost all increments. Nevertheless, some deviations are still observable for long increments. Note here that due to experimental constrains the statistics in the latter mentioned PDFs is less good. However, sufficient data was collected for meaningful assumptions to be made.

In summary, the PDFs of normalized increments in artificial fluids with anomaly exponent $\alpha \approx 1$ followed a Gaussian regardless of time lag δt, whereas quantum dots diffusing in the cytoplasm of untreated cells showed significant deviations from a Gaussian and pronounced over representation of longer increments χ for short time lags $\delta t < 3\Delta t$. The same holds true, when the integrity of the cytoskeleton was perturbed by disruption of actin filaments or microtubules – with CytD, LatA, or Noc – respectively. This hints towards heterogeneity in the underlying process. However, when using longer time lags $\delta t = 5\Delta t$, the increment statistics collapsed to the anticipated Gaussian due to CLT. Disruption of the ER on the other hand showed significantly different results. In contrast to the aforementioned, the PDFs of normalized increments followed a Gaussian shape for almost all χ when filipin or hypotonic pressure treatment was applied, hinting towards a more prominent role of the ER in regards to heterogeneous diffusion inside the cell.

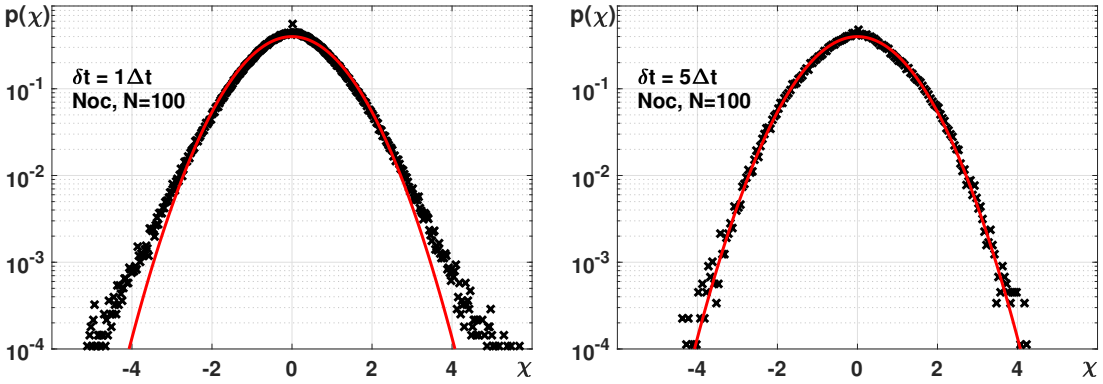

(a) Nocodazole ($\delta t = \Delta t$)

(b) Nocodazole ($\delta t = 5\Delta t$)

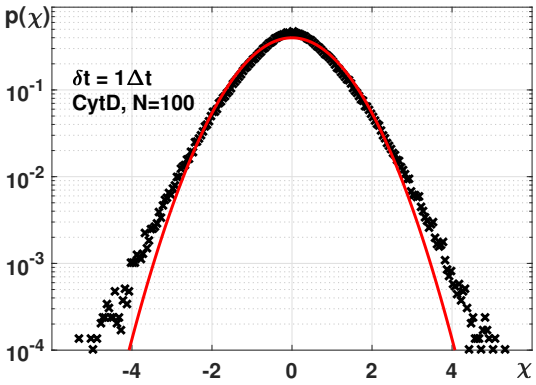

(c) Cytocalasin D ($\delta t = \Delta t$)

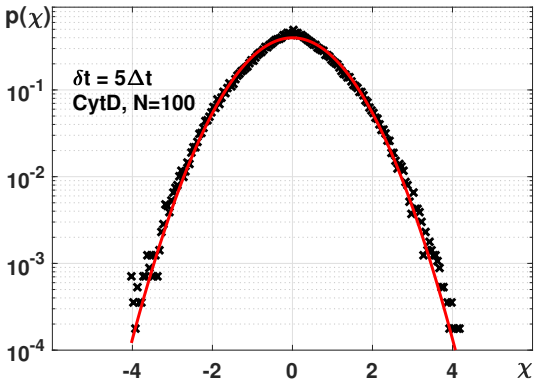

(d) Cytocalasin D ($\delta t = 5\Delta t$)

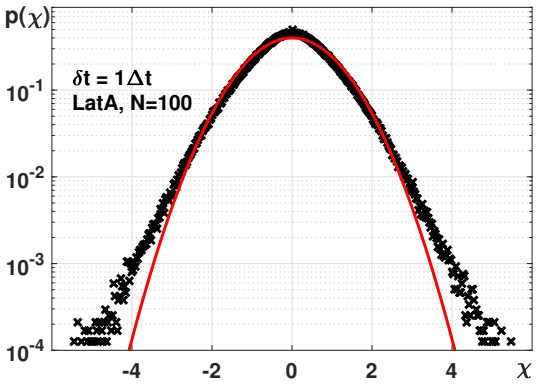

(e) Latrunculin A ($\delta t = \Delta t$)

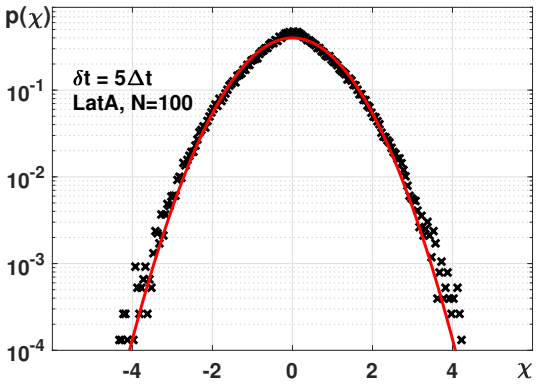

(f) Latrunculin A ($\delta t = 5\Delta t$)

Figure 4.15: The PDFs of normalized increments χ from quantum dot trajectories with $N = 100$ positions tracked in cells where the cytoskeletal integrity was perturbed with Noc (upper panels), CytD (middle panels) or LatA (lower panels). For small time lags $\delta t = \Delta t$ (left panels) all conditions followed the anticipated Gaussian (red line) for small χ but showed significant deviations for larger χ. Independent of condition, all $p(\chi)$ collapse to a Gaussian when examining longer time lags $\delta t = 5\Delta t$ (right panels).

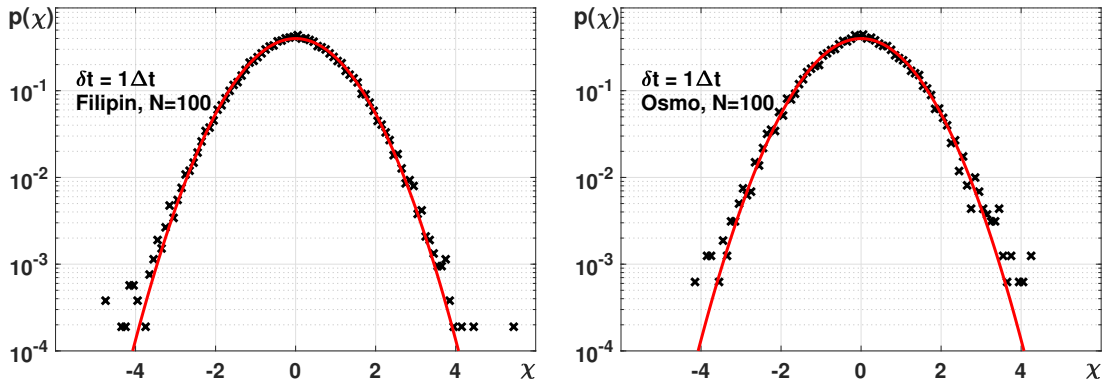

(a) Filipin ($\delta t = \Delta t$) **(b)** Hypotonic pressure ($\delta t = \Delta t$)

Figure 4.16: The PDFs of normalized increments χ from quantum dot trajectories with $N = 100$ positions tracked in cells where the ER was disrupted with **(a)** filipin or **(b)** hypotonic pressure. Data of $\approx$ 40k increments with time lag $\delta t = \Delta t$ is shown in black. The data are in both cases in good agreement with the anticipated Gaussian (red line) for a homogeneous process. Nevertheless, some deviations for long χ are observable.

4.5. The autocorrelation of fluctuations in squared increments

Since the previous results hinted towards heterogeneity in the random walk of individual trajectories, the autocorrelation of fluctuations in squared increments $G(\tau)$, as described in Sec.3.6, was employed to gain more insight. As a negative control, the ensemble-averaged autocorelation of squared increments calculated for quantum dots diffusing in pure glycerol (black) and 60% aqueous sucrose solution (red) is shown Fig.4.17. The standard deviations are depicted as a grey area. Both curves show no correlation for all lag times τ. In fact, the fluctuations around a slightly negative offset are only due to insufficient averaging. The increase in fluctuations for long lag times is due to poor statistics.

For short trajectories ($N = 100$) acquired in untreated cells, $G(\tau)$ showed a significant non-trivial decay (Fig.4.18, grey line) starting at positive values and eventually going beyond zero. This negative offset in short trajectories is due to statistical errors as explained earlier in Sec.3.6. For long trajectories ($N = 500$), the autocorrelation function of fluctuations in squared increments decayed to zero (see inset Fig.4.18**(a)**, dashed lines are $G(\tau) = 0$).

Perturbing the integrity of the cytoskeleton, as described before, did not lead to changes in $G(\tau)$ when comparing the treated conditions to untreated cells. The data for microtubule breakdown with nocodazole (red diamonds) for short ($N = 100$) and long ($N = 500$) trajectories, as well as data from cells where actin filaments were depolymerized using either cytocalasin D (black circles) or latrunculin A (yellow triangles) are shown in Fig.4.18**(a)**. Again, a permanent negative offset is present in the data for short trajectories, eventually leading to the exceedance of $G(\tau) = 0$.

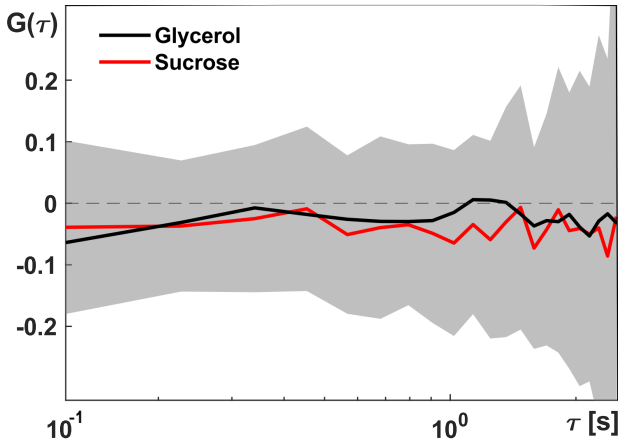

Figure 4.17: Ensemble-averaged autocorrelation of fluctuations in squared increments from trajectories with $N = 50$ positions of quantum dots diluted in pure glycerol (black) and 60% per weight aqueous sucrose solution. The standard deviation is shown in grey. Both curves show no significant correlation in their squared increments, only a slight negative offset due to insufficient averaging. Note that increased fluctuations and errors at longer lag times τ are due to poor statistics.

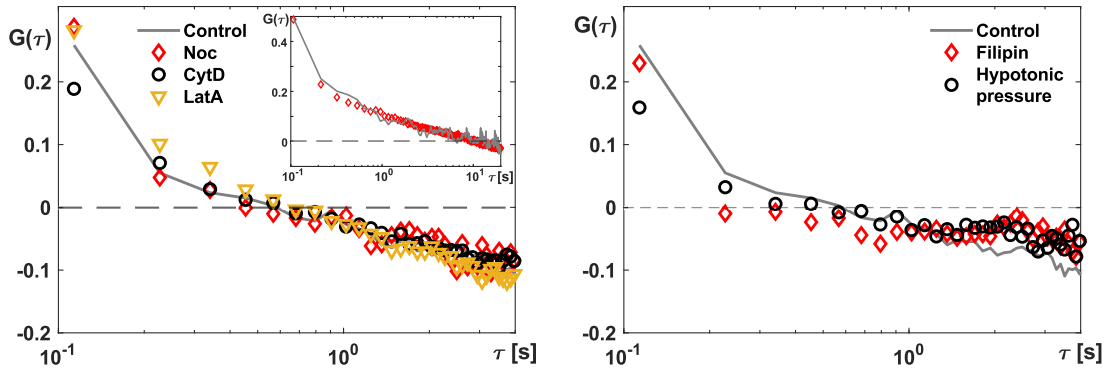

(a) Cytoskeleton breakdown **(b)** ER disruption

Figure 4.18: The ensemble-averaged autocorrelation of fluctuations in squared increments from short trajectories ($N = 100$) of quantum dots in untreated cells (grey line) and cells where **(a)** the cytoskeleton was depolymerized with nocodazole (red diamonds), cytocalasin D (black circles), or latrunculin A (yellow triangles); or **(b)** ER was disrupted using filipin (red diamonds) or hypotonic pressure (black circles), showed a non-trivial decay. Inset in **(a)** For long trajectories ($N = 500$) a long lasting non-trivial decay starting at positive values is observed as well. Dashed lines show no correlation as guide to the eye.

The autocorrelation function of fluctuations in the squared increments of trajectories ($N = 100$) acquired from cells where ER was disrupted using either filipin III (red diamonds) or hypotonic pressure (black circles) in comparison to the untreated cell data (grey line) is shown in Fig.4.17**(b)**. As seen with the data for cytoskeleton breakdown stated before, a non-trivial decay of the correlation function was observed for both treatments. However, the autocorrelations seemed to be slightly less pronounced, when the ER network was disrupted.

In summary, a non-trivial decay of the autocorrelation of fluctuations in squared increments was observed for SPT trajectories of quantum dots regardless of length from untreated cells that indicate traces of heterogeneity in the random walk process. When the integrity of cell organelles that are widespread across the cell, i.e. intermediate filament, microtubules, or the ER network, is perturbed, the previously observed correlations were still present. However, disrupting the ER seemed to reduce the effect of heterogeneity to some degree.

4.6. Insights from the local convex hull approach

Since previous analysis suggested some kind of heterogeneity in the underlying process, i.e. particles mobility changes within individual trajectories, the LCH was employed to directly probe for switching between different mobilities. To this end, trajectories were rescaled to the same length scale as described in Sec.3.5 and for each trajectory, the largest diameter $S_d(t)$ of the local convex hull for the five positions visited in the period $[t - 2\Delta t, t + 2\Delta t]$ was determined. This resulted in 96 individual, normalized LCHs for each trajectory with $N = 100$ positions. General stationarity of trajectories for individual experimental conditions was assumed, hence allowing the combination of all found diameters of LCHs into one single PDF $p(S_d)$ per condition.

In Fig.4.19 the PDFs of rescaled LCH diameters from trajectories with $N = 100$ positions are shown for **(a)** untreated cells and cells treated with nocodazole, and **(b)** cytocalasin D and latrunculin A-treated cells. All distributions have a non-symmetric shape around a marked peak ($S_d \approx 0.3$). No significant difference was observed between untreated cells and cells where the cytoskeleton was depolymerized. Using the mean value $\mu \approx 0.3$ and the standard deviation $\sigma \approx 0.1$ for a given PDF of S_d values, a threshold $\theta = \mu + k\sigma$ could be defined (dashed lines) that dissected the population into two distinct states. Particles were rated to be in a more mobile 'off'-state for $S_d \leq \theta$ whereas they were classified to be in the 'on'-state with lower mobility otherwise. As a result, frequent switching was observed in individual trajectories. Since the choice of threshold is somewhat arbitrary, analysis with a threshold where k was set to $k = [1, 2, 3, 4]$ was done. However, it was found that the fraction of trajectories that did not show any switching at all grew with increasing k and therefore, thresholds with $k = [1, 2]$ were preferentially used. With this in mind, calculating the area under $p(S_d)$ for untreated cells in the range $0 \leq S_d \leq \mu + 2\sigma$

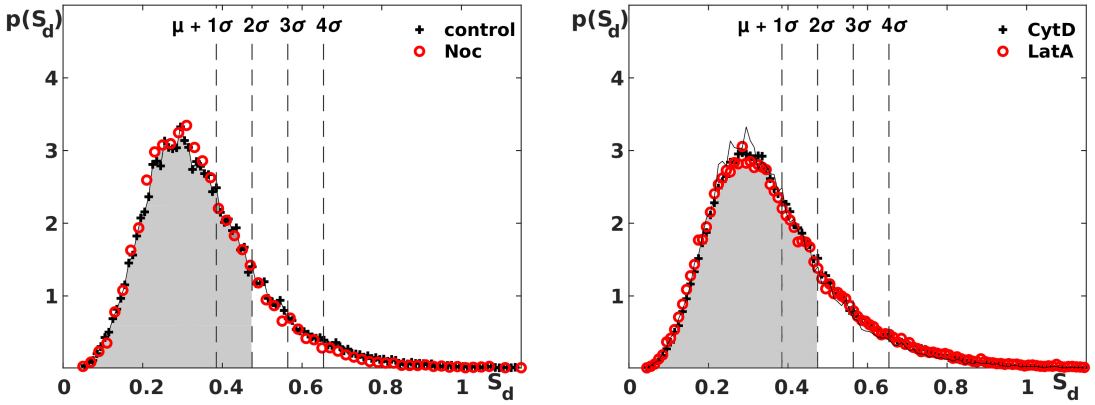

(a) MT breakdown **(b)** Actin filament break down

Figure 4.19: The PDF of rescaled S_d values obtained from trajectories with $N = 100$ positions for **(a)** untreated (black pluses) and nocodazole-treated cells (red circles), and **(b)** cells where actin filaments were depolymerized. All distributions show an overall non-symmetrical shape with a marked peak at ≈ 0.3. Vertical dashed lines indicate the threshold $\theta = \mu + k\sigma$ with $k = [1, 2, 3, 4]$ used to dissect individual trajectories into 'on'- and 'off'-states. When $k = 2$ was chosen, particles were seen to be in the less mobile state for approximately 80% of all time points (grey area).

(grey area) revealed that about 81% of all S_d values came from trajectory segments with presumably low mobility, since they had low S_d values. In turn, the remaining part of the PDF had to be due to at least one more state with higher mobility, hence giving rise to larger S_d values. Evaluating the same quantity for cells, where microtubules were depolymerized, 85% of time points were rated to be in the low mobility 'on'-state. When intermediate actin filaments were depolymerized, the low mobility fraction was estimated to be 78% for CytD- and LatA-treatment alike. Therefore, no significant differences were observed when breaking down microtubules or actin filaments.

Looking at individual, rescaled tracking data, the threshold defined by the mean value and standard deviation was used to dissect the trajectories into phases of high- and low mobility to which their respective residence times were assigned as described in Sec.3.5. The exponential PDFs of residence times (full lines) extracted from individual trajectories ($N = 100$) of untreated (black) and nocodazole-treated cells (red) are shown in Fig.4.20 for two different choices of threshold. A frequent switching with a markedly larger mean residence time in the low-mobility ('on'-) state was observed, irrespective of treatment. Increasing the threshold (Fig.4.20**(b)**) resulted in a smaller fraction of trajectories showing switching at all (see Fig.4.22), however, the mean residence times only changed mildly.

Next, the influence of the ubiquitous ER network on the supposedly switching behavior in individual trajectories was examined. To this end, the ER was disrupted as described before, quantum dots trajectories with $N = 100$ positions were acquired using SPT, and

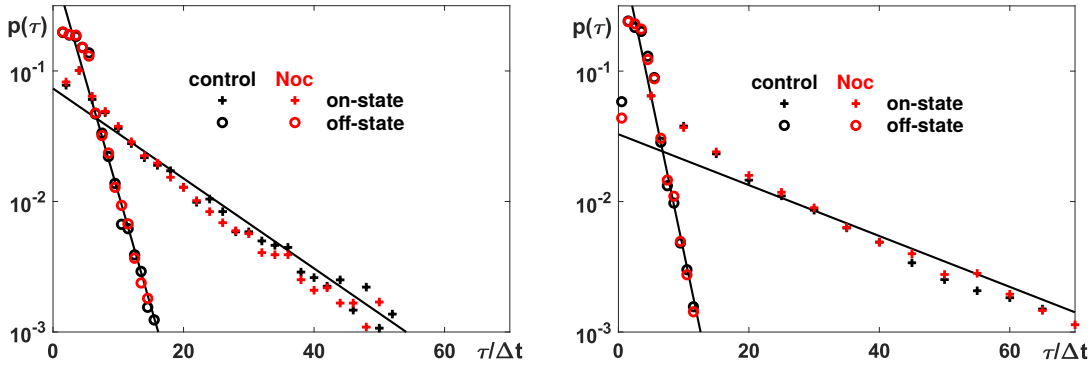

(a) Threshold: $\theta = \mu + \sigma$ **(b)** Threshold: $\theta = \mu + 2\sigma$

Figure 4.20: The residence times $\tau_{\text{on, off}}$ in the low mobility ('on'-) state (pluses) and higher mobility ('off'-) state (circles) extracted from individual trajectories ($N = 100$) from untreated (black) and nocodazole-treated cells (red) for threshold values **(a)** $\theta = \mu + \sigma$ and **(b)** $\theta = \mu + 2\sigma$ feature exponential PDFs (full black lines) with substantially longer mean residence times in the 'on'-state. No significant differences were seen for untreated and Noc-treated cells, nor when the threshold was increased.

the aforementioned approach was used to extract the PDF of largest diameters of LCH for positions visited in a $5\Delta t$ period from rescaled trajectories. These PDFs are shown in Fig.4.21**(a)** for filipin-treated cells (red pluses) and cells where hypotonic pressure was applied (black circles). As observed before, the distributions showed a non-symmetric shape with a marked peak. However, the PDFs seemed to be shifted to smaller S_d values as compared to the untreated condition (full black line). Calculating the fraction of time points in which particles were seen to be in the low mobility state with the threshold $\theta = \mu + 2\sigma$, resulted in 94% (filipin) and 88% (hypotonic pressure), further emphasizing the supposed overall shift to lower mobility. However, comparing the PDFs of residence times found with the analysis for untreated and filipin-treated cells (Fig.4.21**(b)**) revealed no substantial differences. As observed before, time spend in the low mobility state (τ_{on}) as well as $p(\tau_{\text{off}})$ follow an almost exponential shape for both conditions. A summary of the results regarding the fractions of lower mobility and mean residence times of the respective experimental condition is found in Table 5.

Additionally, the fraction of trajectories that did not show any intermittent switching when interfering with cell organelles was evaluated depending on the assumed threshold θ. The results for cells where MT breakdown was achieved using nocodazole (red diamonds) and ER disruption was done with filipin (blue circles) are shown in Fig.4.22. When using a rather low threshold $\theta = \mu + \sigma$, almost all trajectories ($f > 98.5\%$) of all conditions show at least one incidence of crossing the threshold, hence the low- and high- mobility state could at least be assigned one time each. Increasing the threshold naturally decreased the

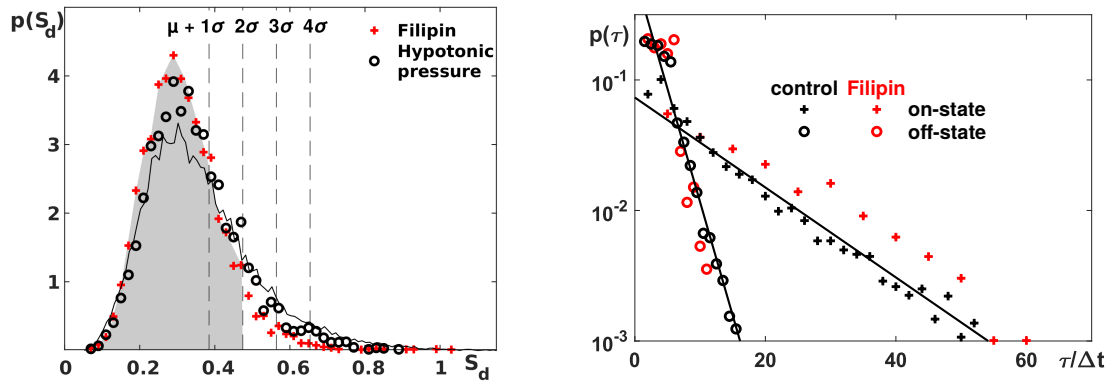

(a) PDF of LCH diameters

(b) PDF of residence times

Figure 4.21: **(a)** The PDF $p(S_d)$ obtained from rescaled trajectories ($N = 100$) of cells where the ER network was disrupted with filipin (red pluses) or using hypotonic pressure (black circles). Again a non-symmetric distribution around a marked peak describes the data well. The PDFs are shifted towards smaller LCH diameters compared to untreated cells (full black line). Using $k = 2$, particles are seen to be in the 'on'-state for about 94% (filipin, grey area) and 88% (hypotonic pressure) of all time points, respectively. **(b)** The PDF of residence times in the high- and low mobility states, extracted from individual trajectories with a threshold $\theta = \mu + \sigma$ for untreated (black) and filipin-treated cells (red) have exponential shapes. No significant differences in mean residence times were observed, when ER network was disrupted.

fraction of individual trajectories that crossed it for all conditions, meaning more trajectory segments were assigned to the 'on'-state. However, comparing the different conditions revealed that untreated (black crosses) and Noc-treated cells show no significant differences, whereas the 'non-switching'-fraction of trajectories where the ER was disrupted featured a much stronger increase. In fact, choosing $\theta = \mu + 3\sigma$ resulted in $\approx 50\%$ of trajectories showing no intermittent switching for untreated and nocodazole-treated cells alike, while more than three quarters of filipin-treated cells occupied the state with lower mobility.

Adding up, the LCH approach was used to find the PDF of largest diameters S_d of individual trajectory segments within a given time period $[t - 2\Delta t, t + 2\Delta t]$ (see for example Fig.4.19). Since stationarity was assumed, all PDFs of one condition were merged into one. Those distributions had a non-symmetric shape with one marked peak each. Calculating the mean value μ and standard deviation σ allowed for the definition of a threshold value $\theta = \mu + k\sigma$. This value was used to dissect the combined PDF into low- and high-mobility states on the one hand, and specify segments within individual trajectories where tracers occupied the respective states on the other hand. The latter was used to extract the respective residence times from experimental data as shown in Fig.4.20. Overall, mean residence times seemed to be independent of the assumed threshold and did not show significant deviations for treated cells when compared to the untreated condition. However,

	untreated	Noc	CytD	LatA	Filipin	Hypotonic pressure
low-mobility [%] $\theta = \mu + \sigma$	64	68	61	62	78	69
low-mobility [%] $\theta = \mu + 2\sigma$	81	85	78	78	94	88
$\langle \tau_{\text{on}} \rangle$ $[\Delta t]$	17	15	13	12	15	19
$\langle \tau_{\text{off}} \rangle$ $[\Delta t]$	2.7	2.8	3.0	3.0	3.3	2.2

Table 5: Fraction of trajectory segments where $S_d < \theta$ (in %) for two different thresholds and mean residence times $\langle \tau \rangle$ for untreated cells and cells, where either cytoskeleton was broken down (Noc, CytD, LatA) or ER was disrupted (filipin, hypotonic pressure). Mean residence times in the lower-mobility state are on average approximately 5 times longer.

calculating the area under $p(S_d)$ within different threshold limits (see Table 5) revealed an increase in low-mobility associated trajectory segments when the ER was disrupted. When increasing the threshold from $\theta = \mu + \sigma$ to $\theta = \mu + 4\sigma$, the fraction of trajectories without any intermittent switching behavior increased as well. No significant differences were observed for nocadazole-treated and untreated cells. In contrast, filipin-treated cells featured a much more significant increase as shown in Fig.4.22.

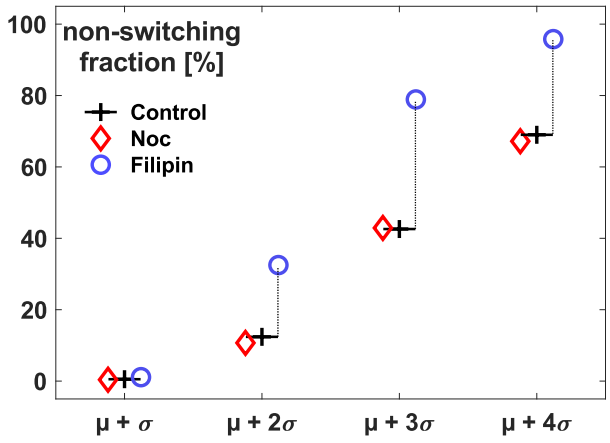

Figure 4.22: The fraction of trajectories without any switching rises with increasing threshold. No significant difference was observed for untreated cells (black cross) and nocodazole-treated cells (red diamond), whereas trajectories from cells where ER network was disrupted (blue circle) featured a much stronger increase in the non-switching fraction.

4.7. Simulation

4.7.1. Generation of fractional Brownian motion trajectories

To compare the experimentally obtained data to theoretical predictions, simulation of fBM trajectories was done using the `wfbm`[4] algorithm included in `MATLAB` proposed by Abry and Sellan [39] and developed further by Bardet et. al [40].

The basic idea of the algorithm is to build a biorthogonal wavelet depending on a given orthogonal one and adapting it to the Hurst parameter H chosen as input. At the beginning of the algorithm, the fBM process is expressed as a fractional integral of the white noise process. The generated sample path has to have some kind of memory kernel as well as Gaussian characteristics. To achieve this, it is obtained by a reconstruction using the new wavelet beginning with a wavelet decomposition. This reconstruction is designed to have independent random Gaussian realizations of details coefficients, whereas the approximation coefficients arise from a fractional autoregressive integrated moving average process.

The samples generated following this scheme showed sufficient characteristics, but exhibit too many high-frequency components. Bardet et.al [40] circumvented this problem by downsampling the obtained sample by a factor 10.

4.7.2. Simulation of intermittent fBM

To describe the experimental data gathered in measurements regarding SPT of quantum dots in the cytoplasm, an intermittent fBM model was constructed.

First, two-dimensional trajectories with fixed anomaly exponents $\alpha_0 = {}^{H}/_{2}$ were obtained via the `wfbm` `MATLAB` routine as described before. The trajectories were chosen to have N positions in each spatial dimension, of which $N-1$ successive step increments (Δx, Δy) were extracted and re-scaled to yield a TA-MSD with generalized transport coefficient K_α in the range of experimentally observed values. The time increments Δt between successive positions were set to 100 ms for compatibility with experimentally obtained data. For the implementation of heterogeneity – i.e. an intermittent fBM random walk – a stochastic switching between two modes of motion with rates k_{on} and k_{off} was used. In fact, while the previously obtained steps of the random walk were left unchanged in the 'on' (bound)-state, the steps were multiplied by a factor $s > 1$ in the 'off' (unbound)-state. This enabled modeling of enhanced mobility in the unbound state. Hence, the transport coefficient switched randomly with rate k_{on} and k_{on} from K_α to sK_α and back. Due to

[4] One has to be careful, when using the `wfbm` routine implemented in `MATLAB`. For some unknown reason values close to $H = 0.5$ but not quite 0.5 gave errors. Therefore, values in the range $0.475 < H < 0.525$ should be avoided or substituted with $H = 0.5$ to fix the bug.

this perturbation in fBM behavior, the individual, as well as ensemble-averaged TA-MSD of the trajectories showed a slight increase in scaling coefficients $\langle\alpha\rangle$ compared to the input values α_0. The influence of the intermittent switching on the resulting trajectory depends on the length of the trajectory, the factor s, and the rates k_{on} and k_{off}. If these switching rates are to low, or the trajectories are to short, one individual trajectory could be governed by one state only, since the time spend in one particular state might exceed the length of the trajectory. Hence, heterogeneities within individual tracks could no longer be detected. Nevertheless, the ensemble average should reveal the intermittent switching behavior. Hence, trajectory-to-trajectory variations and heterogeneities would be made observable.

5. Discussion

To explore the supposedly heterogeneous subdiffusion in the cytoplasm of living mammalian cells, extensive single particle tracking experiments were performed on carboxylated quantum dots that had been introduced into cultured HeLa cells by a technique called bead loading. In particular, the motion of tracer particles was quantified in artificial, highly viscous fluids, and in the cytoplasm of untreated cells and cells where the integrity of large ubiquitous organelles was perturbed. To implement the latter condition, the intermediate filaments of cells were disrupted using cytocalasin D or latrunculin A, microtubules were depolymerized with the aid of a nocodazole protocol, or the endoplasmic reticulum network was fragmented with filipin III, or by applying hypotonic pressure to the cells. From the data gathered in experiments and the results presented in the previous section, conclusion can be drawn which lead to the construction of a model that on the one hand reliably reproduces the features and characteristics of the marked diffusion observed, and on the other hand gives reasonable predictions on what the cause of the presumably underlying heterogeneity might be.

At first, the anomaly exponents α and generalized transport coefficients K_α were extracted from individual trajectories by fitting a simple power-law to their TA-MSDs. The probability density functions of anomaly exponents showed considerable trajectory-to-trajectory fluctuations around a distinct mean value, since measurements were done in living cells. One should always keep in mind that experiments on living cells are far from thermal equilibrium and hence, fluctuations should be considered at all times due cell-to-cell variations. Another cause of additional perturbation could be the applied treatments to the cells that might induce stress and slightly change their behavior. However, it was shown that culture cells, and in particular HeLA cells, survive treatments with e.g. nocodazole for several days. Therefore, following other protocols it was concluded that vital cellular functions were not disturbed on the experimental time scale and that extracted PDFs are reasonable.

To validate the significance of the extracted mean anomaly $\langle\alpha\rangle$ and probing for potential perturbations of the power-law scaling, a bootstrapping approach with geometrical averaging was implemented. Using this approach, the difference between the experimentally extracted TA-MSDs and their respective simple, offset-free fits $K_\alpha\tau^\alpha$ was calculated where the influence of localization errors should be strongest, i.e. at $\tau = \Delta t$. In all cases where data was acquired using non-scanning microscopy methods, only a small positive difference c was observed. This indicated a positive offset in the experimental MSDs, that was slightly lower than the diffusional contribution, i.e. $c/(K_\alpha \Delta t^\alpha) < 5\%$. When looking at individual time- and ensemble-averaged MSDs from the bootstrapping approach, no significant deviation from the linear scaling was observed for any data in the limit $\tau \to 0$, leading to the conclusion that positive and negative contributions to the offset, i.e. static

and dynamic localization errors, respectively, appear to cancel each other out. Therefore, fitting with a simple power-law gives meaningful results for anomaly exponents.

As a control, quantum dots were tracked in highly viscous, artificial fluids of pure glycerol and 60% per weight aqueous sucrose solution. The two solutions were chosen to validate the analysis routine, since they should show no subdiffusion and represent different viscous regimes due to their respective viscosity. Both experimental conditions revealed the anticipated vanishing anomaly exponent $\langle\alpha\rangle = 1$ expected for normal diffusion. The diffusion constant D for sucrose solution was found to be $D = 260{\times}10^{-3}\mu m^2/s$. Using the *Einstein-Smoluchovski* relation (Eq.1.8) with $\eta_{suc} \simeq 50\,\mathrm{mPa\,s}$ at $T = 25\,^{\circ}\mathrm{C}$ and assuming the quantum dots hydrodynamic radius to be $r = 15\,\mathrm{nm}$, the expected diffusion constant can be calculated to be $290{\times}10^{-3}\mu m^2/s$ which is in good agreement with the experimental results. Since small displacements in combination with limited spatial resolution could perturb the tracking, glycerol was used as a test environment, due to its viscosity being similar to values observed in the cytoplasm. However, no deviations from the anticipated normal diffusion was observed. Moreover, the rescaled velocity autocorrelation function for both artificial fluids was calculated. It was found that no anti-persistence related minimum at $\tau/\delta t = 1$ was observed, as expected for normal diffusion. Hence, these data confirm that high viscosity, small displacements or a particularly slow diffusion did not seem to affect the measurements outcome.

When quantifying the particles' motion in the cytoplasm of living cells, a distinct and heterogeneous subdiffusion was observed for all experimental conditions. However, the individual characteristics and features varied depending on the applied treatment. Untreated cells had a generalized transport coefficient of $K_\alpha = 10{\times}10^{-3}\mu m^2/s^\alpha$ and a mean anomaly of $\langle\alpha\rangle = 0.58$. This value is in excellent agreement with anomaly values observed in the cytoplasm of cells in previous studies [30, 33, 56] and it was confirmed by analyzing the TA-MSDs with the validated resampling approach [178] presented earlier.

Since DMSO was used as a universal solvent in most of the used protocols and its reported toxicity at higher concentrations could interfere with the measurements, control experiments with pure DMSO in respective concentration were done. It was found that the anomaly shifted to insignificantly higher values ($\langle\alpha\rangle = 0.65$) compared to untreated cells $\langle\alpha\rangle = 0.58$. Thus, if DMSO has any effect, it is rather slightly shifting motion behavior to more normal diffusion. Therefore, the presented results are not an artifact of the use of DMSO.

One of the main objectives of this thesis is to find potential causes of the distinct subdiffusion of tracers present in the cytoplasm of cells. Therefore, the effect of the cytoskeleton on the motion of presumably inert particles had to be studied. It was found that disrupting intermediate actin filaments did not affect the diffusion substantially. The extracted mean anomaly from trajectories where actin was depolymerized using *cytocalasin D* or

latrunculin A basically did not change compared to the values obtained from untreated cells. It seems that breaking down actin filaments only increased the generalized transport coefficients slightly, potentially due to less 'obstacles' and therefore decreased caging effects. However, the change seems insignificant compared to the width of $p(K_\alpha)$. Disrupting microtubules with the aid of *nocodazole* on the other hand decreased the diffusion anomaly noticeably, hinting towards a more prominent role of the microtubular network. Similar to previous reports on the dynamics of the ER [136], transport coefficients did not show significant changes when looking at short trajectories ($N = 100$). However, the effect of nocodazole increased when longer trajectories were taken into account. In this case, a marked shift to smaller K_α was observed when microtubules were disrupted. This could possibly hint towards longer trajectories only representing a distinct subset of the acquired data, e.g. a lower mobility facilitating longer tracking. In turn, it also indicates that microtubule-associated processes significantly affect the diffusion in untreated cells, beyond the change in scaling of TA-MSDs. Another possible interaction partner having an influence on the diffusion of quantum dots in the cytoplasm of living cells is the endoplasmic reticulum. Fragmentation of the ubiquitous ER tubules with *filipin III* or via *osmotic shock* did not result in any gross alteration of the scaling exponent, since $\langle\alpha\rangle \sim 0.6$ stayed the same. However, the generalized transport coefficients shifted to larger values, indicating a faster transport behavior in the absence of tubular ER network.

Analyzing the ensemble averaged VACF for the previously discussed conditions revealed an anti-persistence related minimum regardless of the integrity of the cytoskeleton. Moreover, the analytical prediction for a fractional Brownian motion VACF (Eq.3.11) is in excellent agreement with all the acquired data without any fitting parameter. This emphasizes the conclusion that the observed subdiffusion is due to an underlying fBM process, since CTRW or obstructed diffusion models for example lack the observed anti-correlation.

Going beyond mean values and averaging, the combined PDF of normalized increments χ in x- and y-direction in a given time lag δt was inspected. This distribution is expected to follow a Gaussian for homogeneous (fractional) Brownian motion at any δt as shown before for quantum dots diffusion in artificial fluids. Yet, significant deviations from the anticipated shape were found in the tails of the PDFs for untreated and cells and cells where the integrity of ubiquitous organelles was perturbed for small time lags $\delta t < 5\Delta t$. In fact, this suggests that particles mobility changes within individual trajectories, resulting in the $p(\chi)$ being constructed from at least two deviating step size distributions. Hence, individual trajectories and in turn the underlying diffusion process are likely to have an intrinsic heterogeneity. When inspecting longer time lags $\delta t \geq 5\Delta t$, the heterogeneity subsides and the PDFs collapse to the anticipated Gaussian again. Interestingly, the effective heterogeneity seems to be smaller when the ER was disrupted, since $p(\chi)$ showed less pronounced, but evident tails when using filipin or hypotonic pressure treatment, compared

to untreated cells or cytoskeletal breakdown of any kind. This hints towards the ER being a potent candidate when trying to find cues to intracellular heterogeneity.

Previous results suggest that particles diffusing in the cytoplasm undergo some kind of switching of their effective mobility within individual trajectories. The simplest process that comes to mind fulfilling this criterion is an intermittent dichotomous process, i.e. switching between two states of mobility with rate k_{on} and k_{off}. For such a process, the ensemble-averaged autocorrelation function of fluctuations in the squared increments for sufficiently long trajectories should decay according to Eq.3.22. In fact, a long-lasting decay of $G(\tau)$ was observed for all experimental conditions in live cell experiments, independent of the applied treatment. Comparing the decay, one notices that the breakdown of the cytoskeleton had no visible effect on $G(\tau)$, whereas the disruption of the ER showed an insignificantly larger effect, resulting in the autocorreletions being slightly less pronounced at similar lag times, again adding to the conclusion that the ER might play on important role in creating heterogeneity in intracellular diffusion.

Based on the previous observations, a direct switching between different states within individual trajectories was probed using the LCH approach. It was found that trajectory segments can be split into two distinct pools of high and low mobility with a threshold of $\theta = \mu + \sigma$ chosen for all experimental conditions, regardless of the applied treatment. However, the occupied fractions change when different treatments were used. Untreated cells and cells where the cytoskeletal integrity was perturbed occupied the low mobility fraction approximately 80% of all times, whereas the high mobility fraction percentage decreased, if the ER network was disrupted. Assuming an intermittent two state fBM model with Markovian switching, the ratio of weights for high- and low-mobility pools of $p(S_d)$ propose a substantially longer mean residence time in the low-mobility state. In fact, actually extracting the PDFs of mean residence times from the data revealed that particles mean residence times in the low-mobility state were about fivefold longer compared to the the high-mobility state, regardless of treatment or threshold value. In turn, estimating the occupied fraction in the low-mobility state with the mean residence times revealed $\langle\tau_{\mathrm{on}}\rangle/(\langle\tau_{\mathrm{on}}\rangle + \langle\tau_{\mathrm{off}}\rangle) \approx 80\%$, which is in excellent agreement with the results presented above. The fraction of trajectories that did not show any switching was found to be dependent on the assumed threshold, as expected. However, in contrast to untreated or Noc-treated cells, trajectories from filipin-treated cells that showed any switching behavior at all become rapidly diminished when the threshold value was increased. This indicated that association to and dissociation from the ER structures are at least involved in creating the mobility switching.

Taken all the findings into account one question arises: How can the apparently heterogeneous, intermittent, cytoskeleton- and ER-dependent subdiffusion of supposedly inert tracer particles in the cytoplasm of living cells be explained in a simple way?

To answer it, a theoretical model has to be found, that predicts the following main features observed in the experimental data with sufficient accuracy:

(i) a strong subdiffusive scaling of individual TA-MSDs and their ensemble average, that show no ergodicity breaking

(ii) the integrity of the microtubular network having a non-negligible impact on the mean anomaly

(iii) a time- and ensemble-averaged rescaled VACF with a significant anti-correlation that fits the analytical prediction of fBM very well

(iv) a PDF of normalized increments $p(\chi)$ that deviates from Gaussian shape for longer χ at short time lags $\delta t < 5\Delta t$, but collapses to the anticipated Gaussian for longer time lags

(v) a non-trivial decay of the autocorrelation of fluctuations in squared increments, indicating a dichotomous process with at least two different mobility states

(vi) single trajectories showing a clear signature for an intermittent switching between higher and lower mobility states when analyzed with the LCH approach

(vii) the fraction of trajectories with switching mobility decreases rapidly upon ER network fragmentation

Taken all observed constraints into account, Occam's razor was used to formulate the simplest model that captures the essence of the experimental data. With this in mind, the dynamics of individual particles was modeled as fractional Brownian motion with a fixed anomaly exponent α_0 and a transport coefficient that randomly switches within each trajectory as presented in Sec.4.7. Fractional Brownian motion was chosen, since other models, e.g. continous time random walk or obstructed diffusion lack the distinct anti-correlation in the VACF. Moreover, CTRW processes show weak ergodicity breaking, thus making it highly unlikly that this type of random process is capable of explaining the experimental data. Scaled diffusion on the other hand shows the required anti-correlation in the VACF, but also features significant weak ergodicity breaking, thus fBM remains. Since two distinct states of mobility were observed in experiments, the particles were assumed to exist in a transient (ER-tubule associated) 'on'-state and a free motion 'off'-state with respective transport coefficients $K_\alpha^{\text{on}} < K_\alpha^{\text{off}}$. Intermittent switching between this states with transition rates k_{on} and k_{off} was modeled as a Markovian process. These rates and the ratio $s = {K_\alpha^{\text{off}}}/{K_\alpha^{\text{on}}}$ were kept fixed in the simulation and the generalized transport coefficients were chosen to be in the range of experimentally observed values. The anomaly values were set to be $\alpha_0 = 0.5$ for untreated cells and $\alpha_0 = 0.3$ for nocodozole-treated cells consistent with previously reported anomaly exponents for ER-junctions [136], since these structures described the fluctuating ER-network with reasonable significance.

This model shows surprisingly good overlap with the experimentally acquired data when choosing $s = 3.5$, $k_{\text{on}} \approx 0.27\,\text{s}^{-1}$ and $k_{\text{off}} \approx 0.01\,\text{s}^{-1}$. Since experimental data revealed an increase in generalized transport coefficients by a factor 2.5 to 6 upon fragmentation of the ER network, assuming the ratio of K_α to be $s = 3.5$ is justified. Moreover, the order of magnitude of the assumed transition rates seems reasonable, since they compare sufficiently well with residence times extracted from experiments.

Despite the simplicity of the model it was found that:

(i) Mean anomalies of simulated realizations extracted from TA-MSDs were $\langle\alpha\rangle \approx 0.55$ and $\langle\alpha\rangle \approx 0.37$ for untreated and nocodazole-treated cells, respectively. These results are in good agreement with the experimental observations (Table 1 and Table 2). Slightly larger anomaly exponent values as the imposed values are consequences of the dichotomous switching that perturbs the pure fBM behavior.

(ii) Anomaly values from previous studies [136] on the effect of microtubule depolymerization on the ER-network (chosen as inputs) showed the experimentally observed effect in the simulated model.

(iii) The VACF (Fig.5.1**(a)**) was in excellent agreement with the analytical prediction (Eq.3.11) when the mean anomaly values according to (i) were chosen.

(iv) The non-Gaussian shape of the PDF of normalized increments of modeled data for $\delta t = \Delta t$ and a more Gaussian shape for longer time lags are in good agreement with the experimental data (Fig.5.2).

(v) The autocorrelation of squared increments had a non-trivial decay and its shape overlapped to a reasonable degree with the experimental data as shown in Fig.5.1**(b)**.

(vi) PDFs of residence times in the 'on'- and 'off'-state (Fig.5.3) were in favorable agreement with the experimentally extracted distributions from the LCH approach.

As a future perspective, it is worth noting that while the experimental core features were already implemented in this simple model, more elaborate models that describe the changing mobility in a more sophisticated way might be helpful when trying to gain deeper insight in intracellular diffusion. However, a simple model describing complex processes appears to be seductive to begin with.

In summary, a heterogeneous, intermittent switching subdiffusion of quantum dots in the cytoplasm of living cells was observed that could be altered upon perturbation of intracellular organelles' integrity, i.e. microtubular disruption or ER fragmentation. A simple intermittent fractional Brownian motion model was capable of capturing the experimental results well. In the model, the anomaly exponents have been set to values observed for the motion of ER junctions in untreated and nocodazole-treated cells. Combining the experimental findings with the insights obtained from the model and its parameters, the

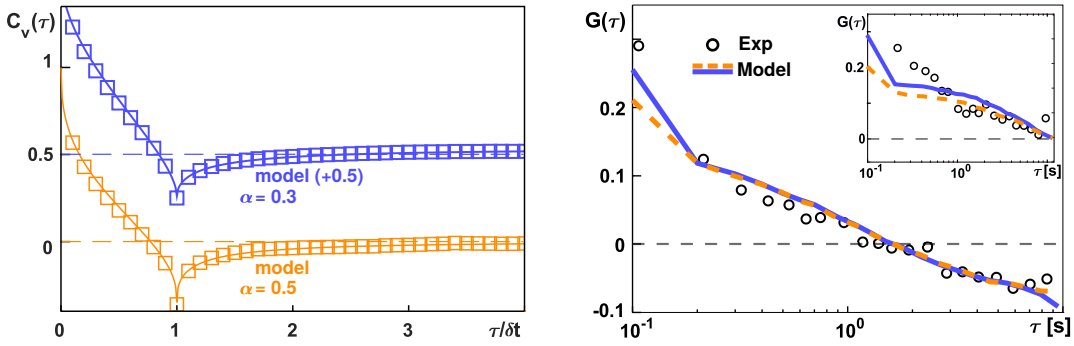

(a) **(b)**

Figure 5.1: **(a)** The VACFs of simulated intermittent fBM trajectories agree with the analytical prediction. **(b)** The autocorrelation function of fluctuations in the squared increments $G(\tau)$ showed a non-trivial decay for intermittent fBM simulation data ($\alpha_0 = 0.5$, dashed orange & $\alpha_0 = 0.3$, full blue lines) which matched with the experimental results (black circles) for short trajectories ($N = 100$) and long trajectories ($N = 500$, inset).

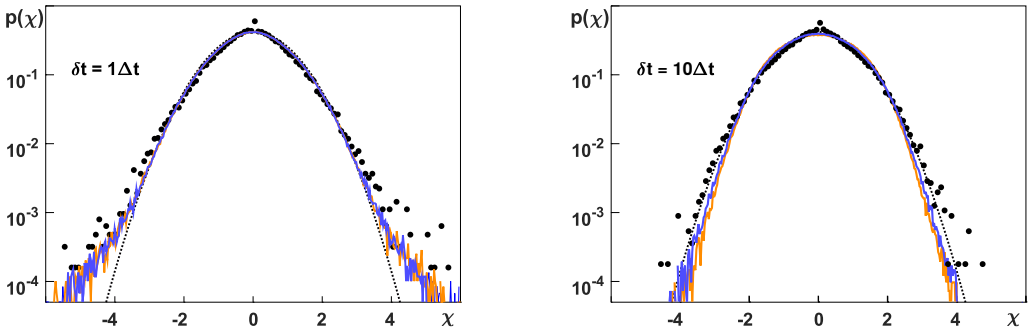

(a) Intermittent fBM model ($\delta t = \Delta t$) **(b)** Intermittent fBM model ($\delta t = 10\Delta t$)

Figure 5.2: The PDFs of normalized increments χ from simulations with $\alpha_0 = 0.5$ (orange) and $\alpha_0 = 0.3$ (blue) coincide with the experimentally observed results (black dots). Deviations from the anticipated Gaussian (dashed black line) are observed for **(a)** small time lags $\delta t = \Delta t$. **(b)** Deviations subsided for longer time lags $\delta t = 10\Delta t$.

conclusion was drawn that particles' free diffusion in the cytoplasm of mammalian cells is hampered by transient association with ER membranes. This effect seems to facilitate a particular low anomaly exponents α compared to artificial, crowded environments. The transient association in turn leads to an intermittent diffusion process that causes heterogeneity in individual trajectories. A simple two state model with distinct generalized transport coefficients and switching rates is sufficient to depict the observed experimental

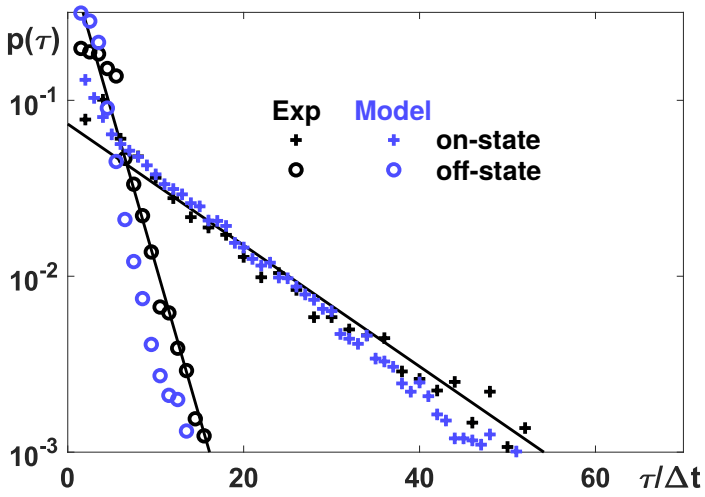

Figure 5.3: The PDFs of residence times in the 'on'- and 'off'-state obtained for simulated trajectories from the LCH approach (blue) were in favorable agreement with the results obtained from experiments (black).

heterogeneity. Thus, apparently there is no need for a continuous distribution of 'diffusing diffusivities'. The diffusion itself is best described by fractional Brownian motion, presumably due to the crowded environment. Since microtubular and ER network are intertwined inside the cell, active MT-based processes could couple to the ER which in turn lead to a presumably indirect active motion contribution to the particles' dichotomous diffusion process, if the integrity of the microtubular network is not perturbed. Lower α values when nocodazole is used support this hypothesis. Yet, not all results could be explained in full depth. The persisting, strong subdiffusion of particles after fragmentation of the ER hints towards additional structures with which tracers might interact. These structures could possibly be the network of intermediate filaments [180] or the vesiculated ER membrane that mimics a microemulsion [181]. Hence, the subdiffusion of tracer particles in the cytoplasm of mammalian cells is indeed considerably more complex than anomalous diffusion in artificially crowded fluids.

PART III

On the importance of microtubule polyglutamylation for the regulation of cytoskeletal architecture and motility in *Trypanosoma brucei*

6. Results

SPT experiments are a powerful tool, when examining small inactive tracers in an active environment. However, the motion behavior and motility of active tracers can be studied using similar experiments. In the following section, insights from SPT experiments on kinetoplastea (T. brucei) motility in unaltered individuals and in parasites, where the tubulin polyglutamylation was reduced using RNA interference are presented. Parts of the these results have been published in Journal of Cell Science, ***133*** *(2020) [182].*

6.1. Problem definition

The highly ordered and stable subpellicular microtubule cytoskeleton of kinetoplastid cells is one of the defining features of *T. brucei* shape during all stages of its life cycle. However, more dynamic behavior has to transiently be allowed during the transition between cell cycle stages to enable morphological rearrangements. The actual regulation of these activities is poorly understood at this point in time. Two possible levels of regulation exist which might shed light on the topic: activities of cytoskeleton-associated proteins and posttranslational modifications (PTMs) of microtubules as stated earlier in Sec.1.4. These regulations have to be finely tuned, since deviations from the nominal might lead to potential changes in the structure of the kinetoplastid and in turn influences its motion behavior and potential chances of survival. Here, the knockdown of two presumable tubulin polyglutamylases in *T. brucei*, called *TTLL6A* and *TTLL12B*, was investigated using SPT methods and a quantitative motility analysis in order to find hints to the importance of microtubule polyglutamylation on the dynamics of the parasite.

6.2. The swimming behavior of *T. brucei*

As a basis for analysis, 187 trajectories with a minimum length of $N = 100$ from untreated individual cells (parental 29-13 procyclic form) were used. Examples of these trajectories can be found in Fig.6.1**(a)**. Freely moving individuals showed an expected run-and-tumble like motion pattern. Parasites moved more or less in straight lines for a certain time, until they stopped the persistent motion and started tumbling. The superimposed wave-like pattern is due to the corkscrew-like motion induced by the beating flagellum. Since the detailed analysis of wild type *trypanosoma* motion was not topic of this thesis, more in depth studies can be found in [163, 164, 183]. In contrast, 12 representative trajectories of a total of 417 cells where motion was inhibited by poly-L-lysine-coating of coverslips used as a control population are shown in Fig.6.1**(b)**. Individuals were no longer able to explore their environment on a length scale longer than their own, resulting in an overall more compact shape of the trajectory (note that the scale bar is only 20 µm). No run-and-tumble motion was observed, as expected.

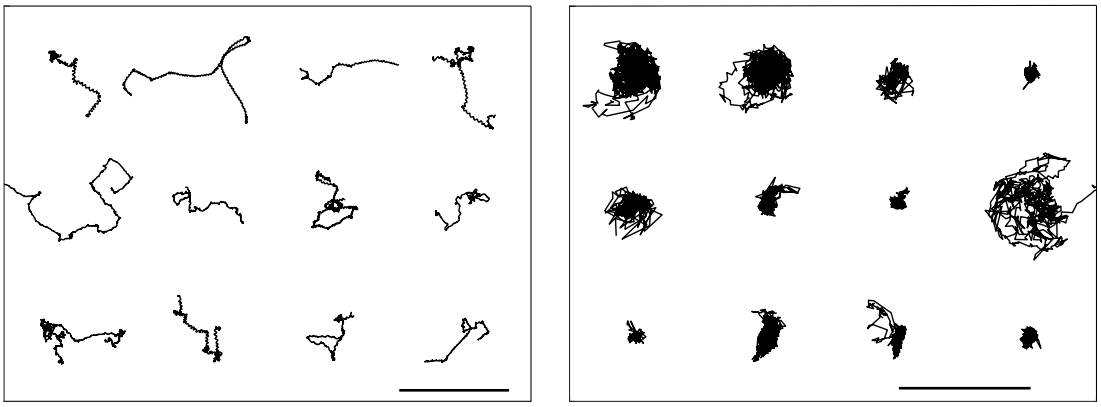

(a) Parental 29-13 procyclic. Scale bar: 200 µm **(b)** Wild type lysine-coating. Scale bar: 20 µm

Figure 6.1: Exemplary trajectories ($N \geq 200$) of wild type parasites on **(a)** uncoated and **(b)** poly-L-lysine-coated dishes to prevent motion. Parasites on uncoated dishes showed run-and-tumble like behavior, whereas individuals on lysine-coated dishes were in most cases bound to a spot and only showed trembling motion. Note the difference in scale bars.

Analyzing the trajectories and computing the time-averaged MSD for each individual one revealed $p(\alpha)$ without any bootstrapping. The PDFs of anomaly exponents for parental 29-13 procyclic cells placed on coverslips without (black) and with lysine-coating (red) are shown in Fig.6.2. The data sets were tested for significant differences with a two-sample Kolmogorov-Smirnov test via the `kstest2` function implemented in `MATLAB`. Three asterisks $(***)$ indicate a highly significant deviation of the two sample distributions ($p < 0.001$). A fairly narrow PDF around a mean value $\langle\alpha\rangle \approx 1.5$ was observed for wild type cells placed on uncoated coverslips. These findings indicate a clear superdiffusive mode of motion, in good agreement with the expectations for microscopic swimmers. In contrast, *trypanosomes* that had been attached to the coverslip showed a highly significant shift to smaller mean values $\langle\alpha\rangle \approx 0.5$ with a slightly broader distribution.

As a second observable, the instantaneous velocity for each position in all trajectories was extracted, since *tryponosomes* showed active motion, in contrast to the diffusion discussed in prior sections. It was calculated by taking the ratio of the displacement Δr within five frames, i.e. $\delta t = 5\Delta t = 0.5\,\mathrm{s}$. All values were combined into one PDF $p(v)$ for each distinct experimental condition, since stationarity was assumed. The PDFs for wild-type cells are found in Fig.6.3**(a)**. Both untreated (black histogram) and lysine-coated (red histogram) data showed broad distributions with maximum velocities up to $\approx 20\,\mu\mathrm{m/s}$. Yet, a drastic shift to smaller velocity values was observed, when coverslips were coated with lysine and thus motion of parasites was hindered. In fact, the average velocity (dashed lines) decreased about fourfold from $\approx 6\,\mu\mathrm{m/s}$ to $\approx 1.4\,\mu\mathrm{m/s}$. However, it seems plausible that not all individuals have been immobilized, since the PDF showed a second, less pronounced maximum at higher velocities.

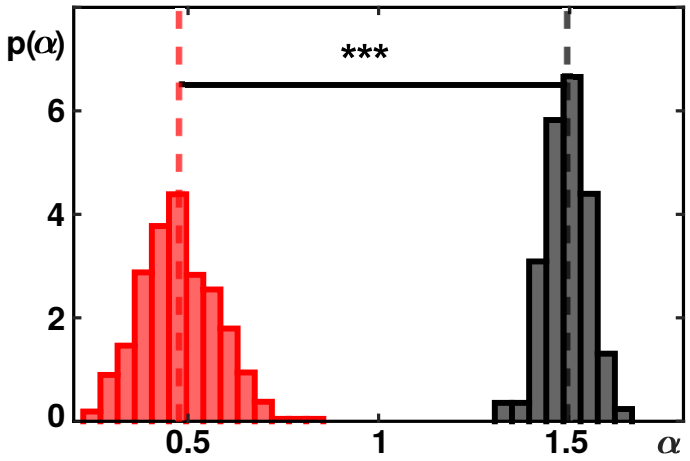

Figure 6.2: The PDF of anomaly exponents α obtained from individual TA-MSDs ($N = 100$) from parental 29-13 procyclic form placed on coverslips without (black) and with lysine-coating (red). Freely moving individuals showed a narrow PDF around $\langle\alpha\rangle \approx 1.5$, whereas motion-inhibited cells showed a highly significant shift to smaller values $\langle\alpha\rangle \approx 0.5$ (indicated by $***$). Significance levels were tested using a two-sample Kolmogorov-Smirnov test.

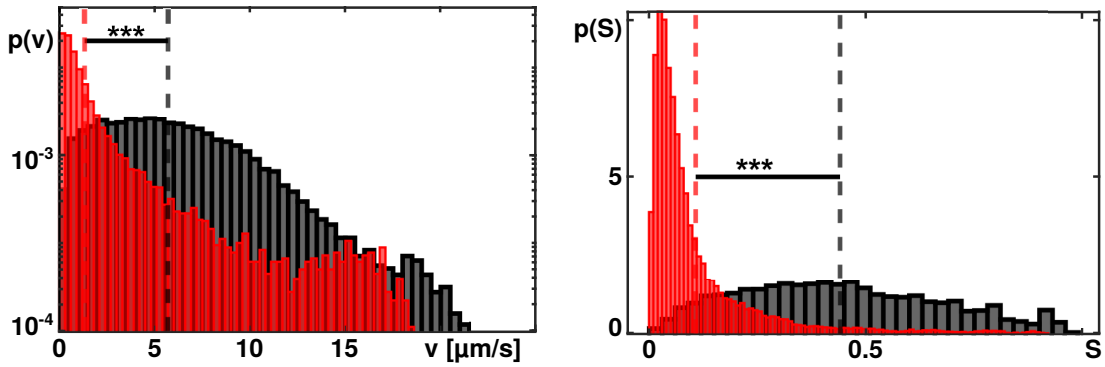

(a) Instantaneous velocity $p(v)$

(b) Straightness $p(S)$

Figure 6.3: **(a)** The PDFs of instantaneous velocity showed a broad distribution for parental 29-13 procyclic cells on untreated coverslips (black) around a mean value $\langle v\rangle \approx 6\,\mu m/s$. An expected significant shift to lower values was observed, when parasites were attached to the coverslips (red) and the respective mean velocity was found to be $\langle v\rangle \approx 1.4\,\mu m/s$. Note the semilogarithmic scaling. **(b)** The straightness of *trypanosomes* showed large variation around a mean value $\langle S\rangle = 0.44$ for free motion (black), whereas $p(S)$ shifted significantly to lower values $\langle S\rangle = 0.11$ for trajectories, where the motion was hindered using lysine-coating (red).

As a third indicator of possible changes in motion behavior, *tryponosomes'* directionality over time was tested using the straightness with a sliding window approach and a window size of $k = 15$. As stated before, stationarity was assumed and thus straightness' were extracted from individual trajectories and combined into one PDF for a certain experimental condition. Straightness values from parental 29-13 procyclic data on untreated coverslips (Fig.6.3**(b)**, black histogram) featured large, but generally symmetrical variations around a mean value $\langle S \rangle = 0.44$. Thus, indicating a variety of different motion patterns, presumably due to differences in the observed run- and tumble phases of individuals. As expected, the straightness decreased significantly, when parasites were attached to the coverslip (red histogram). All presented results are summarized in Table 6.

6.3. The influence of microtubule polyglutamylation deficiencies on cell motility

In order to probe for the macroscopic impact of comprised posttranslational modifications, i.e. depletion of either TTLL6A or TTLL12B, two mutant subpopulations generated as described in Sec.2.4 were evaluated in a quantitative manner without $(-)$ and with induction by doxycycline $(+)$. Image acquisition and subsequent SPT of parasites yielded 352 (15) trajectories for TTLL6A- (TTLL12B-) in the non-induced case, while 28 (61) tracks of induced *trypanosoma* were considered for analysis, respectively. To distinguish between aberrant swimming due to gross morphological distortions, like multiple or non-functional flagella, only cells with a presumably normal phenotype were selected for motion analysis. Representative trajectories with a minimum length of $N \geq 200$ frames for each condition can be found in Fig.6.4. Upper panels show TTLL6A conditions, while TTLL12B tracks are depicted in the lower panels. Left and right panels show individuals without induction by doxycyclin and after RNAi depletion, respectively. Upon superficial visual inspection of cells, altered swimming behavior was noticed, after RNAi depletion of either polyglutamylase (right panels), whereas non-induced mutant subpopulations did not show significant visual changes when compared to the parental population shown in Fig.6.1**(a)**.

The anomaly exponents were extracted from individual TA-MSDs as described before by power-law fitting in the range $\Delta t < \tau \leq 10\Delta t$ and combined into one PDF for each condition, yielding the distributions shown in Fig.6.5. Examining RNAi constructs without induction (blue histograms) resulted in insignificant changes for TTLL6A and mild changes for TTLL12B when compared to the parental population (full black line). In fact, TTLL6A- showed a slight shift to lower values around $\langle \alpha \rangle = 1.45$ with a standard deviation comparable to the wild-type results. TTLL12B- showed more pronounced changes, even without induction. In particular, a broader PDF around a mean anomaly ≈ 1.42 was found. However, both mutant subpopulations showed clear superdiffusive motion behavior for short lag times. On the other hand, highly significant shifts of the PDFs

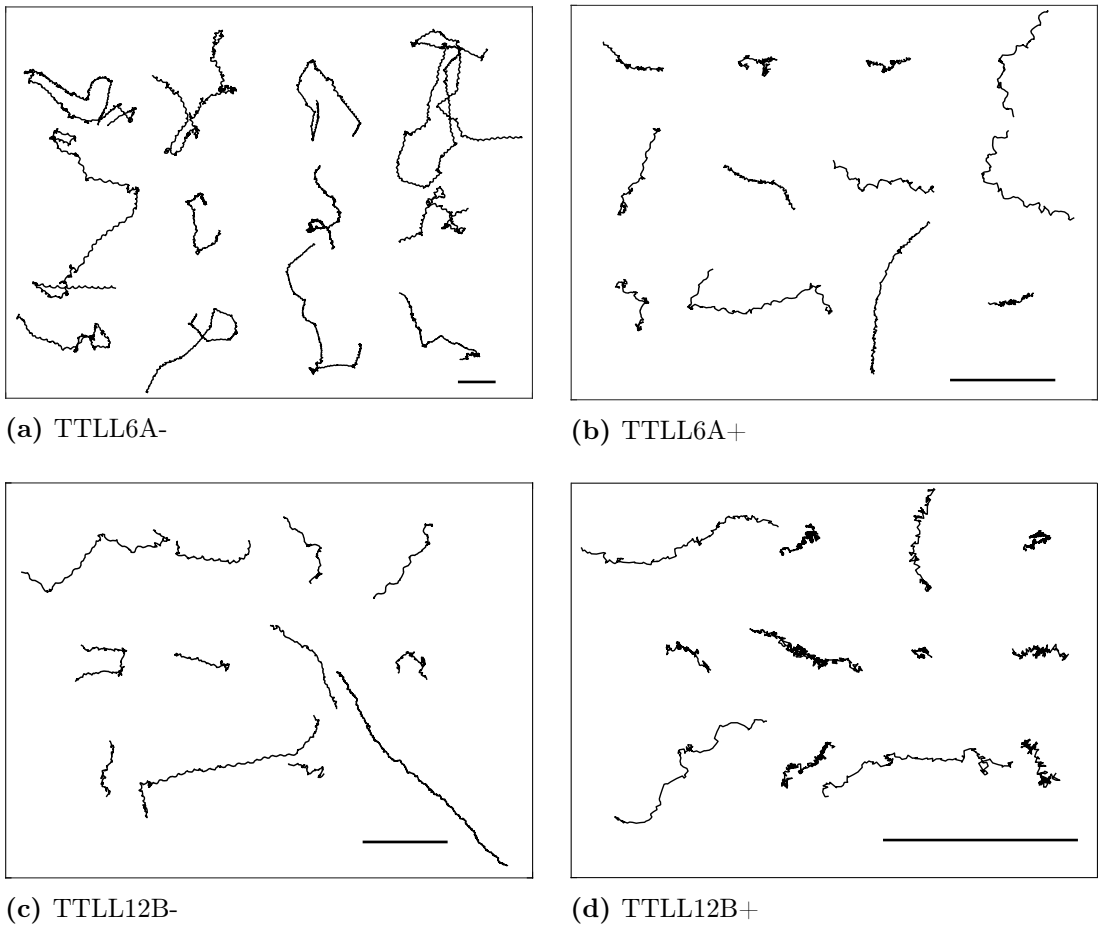

(a) TTLL6A- **(b)** TTLL6A+

(c) TTLL12B- **(d)** TTLL12B+

Figure 6.4: Representative trajectories ($N \geq 200$) for TTLL6A (upper panels) and TTLL12B (lower panels) extracted from non-induced (left) and induced (right) subpopulations. Only individuals with an apparent 'normal' phenotype were selected for motion analysis. Scale bar: 50 µm

towards smaller mean anomaly values were observed upon induction with doxycycline (red histograms). Depletion of polyglutamylase using the TTLL6A pathway showed an overall more normal diffusive motion behavior with variations around $\langle\alpha\rangle \approx 1$, whereas RNAi against TTLL12B even resulted in presumably subdiffusive features, with a mean anomaly of $\langle\alpha\rangle \approx 0.8$ and a standard deviation comparable to non-induced data. The subdiffusive behavior might seem contradictory to the trajectories shown in 6.4**(d)**, since they show signs of persistent motion, however, extraction of anomalies from TA-MSDs was done in the first decade only, thus indicating more erratic movement in the short term limit.

Next, the instantaneous velocities for the RNAi constructs were extracted and compared to the results gained from the parental population. The respective PDFs are shown in Fig.6.6. Similar to the findings from $p(\alpha)$, the velocities only showed mild changes compared to the wild-type data (full black line), when uninduced (blue histogram) TTLL6A cells were studied. Yet, again a significant shift to lower velocities took place upon depletion of

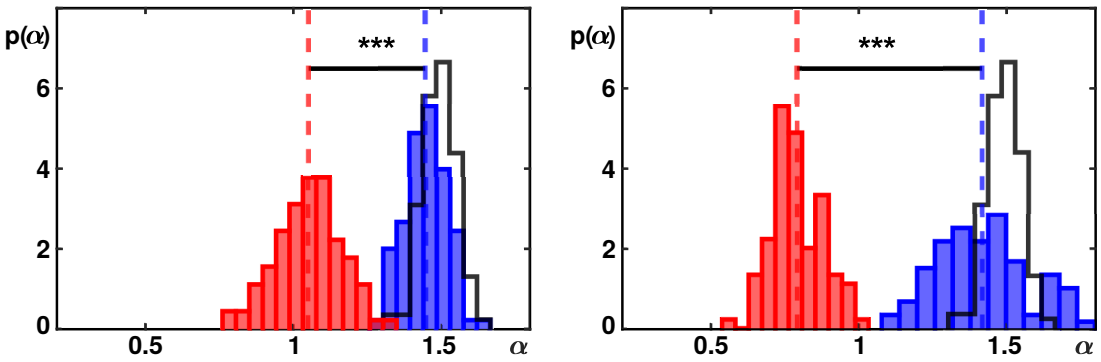

(a) TTLL6A± **(b)** TTLL12B±

Figure 6.5: The PDFs of anomaly exponents for RNAi constructs **(a)** TTLL6A and **(b)** TTLL12B. Non-induced data (blue) shows only small deviation from the wild-type (full black line). A significant shift to smaller anomalies was observed after depletion (red), indicating changes in the motility.

TTLL6A (red histogram). In fact, the mean velocity was reduced by approximately a factor two, indicating a drastic change in motility. Despite a shift to lower velocity values already being noticeable for the uninduced TTLL12B subpopulations (Fig.6.6**(b)**, blue), a significant further decrease in average velocity to approximately 30% of its initial uninduced value was observed for individuals where polyglutamylase was depleted (red).

The straightness extracted from individuals where RNAi treatment was applied, but not yet induced (blue histograms) showed no significant deviation from the parental data (full black line) as shown in Fig.6.7, regardless of which TTLL protein was targeted. Inducing the polyglutamylation depletion, resulted in a significant shift to lower straightness values. As before, the effect of RNA interference was higher for the TTLL12B population. However, mean straightness values did not exceed levels found in attached cells for either condition. Fluctuations in straightness' seemed presumably persistent and independent of treatment, since standard deviation were comparable for all free motion conditions.

As a final indicator of changes in motion patterns and motility, the helical frequency along the predominant direction of motion was quantified for trajectories with at least $N = 200$ positions and a window size of $w_s = 50$. It is worth noting that the helical frequency was only extracted from individuals which showed somewhat persistent motion, since otherwise no significant statements can be made. Thus, no evaluation was done for *trypanosomes* on lysine-coated coverslips. The PDFs $p(\nu_\mathrm{h})$ are shown in Fig.6.8. Helical frequencies of both uninduced RNAi conditions (blue histograms) showed distributions similar to the wild type data (full black line), with tendencies to slightly higher and lower median values, respectively. Upon induction of polyglutamylase depletion (red histograms), the helical frequency seemed to be consistently shifted to overall higher values for both conditions. In fact, the TTLL6A strain experienced a +14% increase in median values ($\tilde{\nu_\mathrm{h}} = 1.50\,\mathrm{Hz}$),

while the shift to higher frequencies observed for the TTLL12B condition was even more pronounced (+47%, $\tilde{\nu_h} = 1.59\,\mathrm{Hz}$). This again emphasizes a presumable shift to more erratic motion upon induction of polyglutamylase depletion.

In summary, the two studied RNAi conditions showed overall similar motion behavior when compared to each other and to the parental condition in the uninduced cases. On the other hand, when inducing polyglutamylase depletion, a shift to lower anomaly exponents, instantaneous velocities, as well as straightness' accompanied by higher helical frequencies was observed. *Trypanosomes* placed on coverslips coated with *poly-L-lysine* used as a control population, showed the anticipated hindered motion.

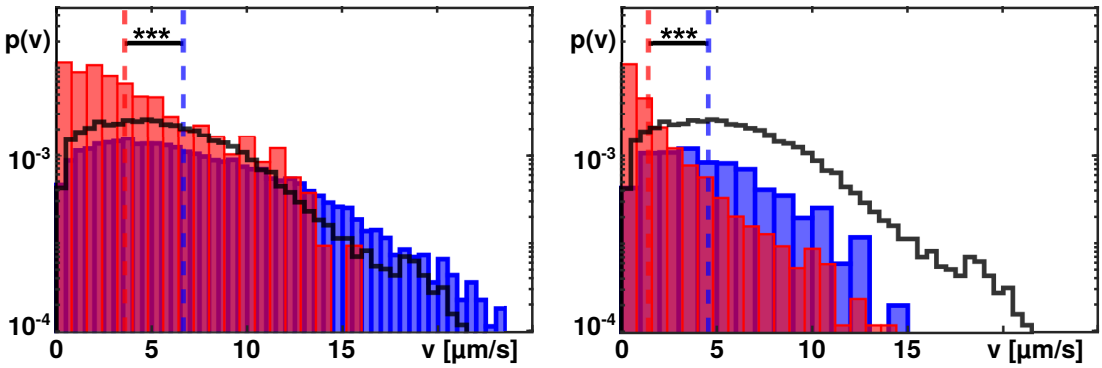

(a) TTLL6A± (b) TTLL12B±

Figure 6.6: The instantaneous velocities obtained from uninduced (blue) *trypanosomes* subpopulations show a significant shift to lower velocities upon induction with doxycycline (red) for both constructs (TTLL6A and TTLL12B). Mean velocities are reduced to about 50% and 30% of their respective uninduced value. Note the semilogarithmic plotting.

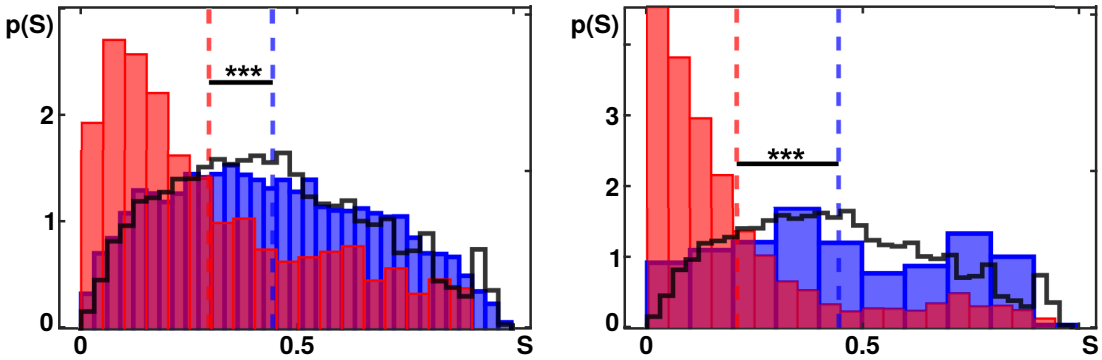

(a) TTLL6A± (b) TTLL12B±

Figure 6.7: The PDFs of straightness' for uninduced RNAi cells (blue) are in good agreement with the parental population (full black line). Both conditions show broad variation around a mean $\langle S \rangle = 0.44$. Depletion of either TTLL protein resulted in a drastic shift to smaller values.

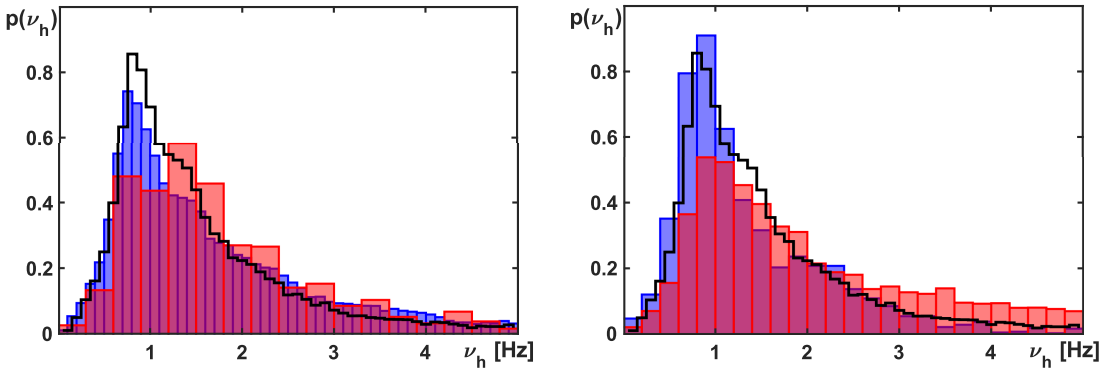

(a) TTLL6A± **(b)** TTLL12B±

Figure 6.8: The PDF of helical frequency obtained from individual trajectories ($N \geq 200$) with a sliding window approach ($w_s = 50$) of parental cells (full black line) shows a non-symmetrical distribution with $\tilde{\nu_h} = 1.2$ Hz. The PDFs of uninduced polyglutamylase depletion (blue histograms) are in good agreement with the parental population for both conditions. A significant shift to higher frequencies is observed upon induction (red histograms). The increase is more pronounced for the TTLL12B subpopulation.

		$\langle\alpha\rangle \pm \sigma_\alpha$	$\langle v\rangle \pm \sigma_v$ [µm/s]	$\langle S\rangle \pm \sigma_S$	$\tilde{\nu_h}$ [Hz]
wild type	free	1.49 ± 0.06	5.70 ± 3.46	0.44 ± 0.23	1.19
	lysine-coated	0.48 ± 0.10	1.32 ± 2.18	0.11 ± 0.13	/
TTLL6A	non-induced	1.45 ± 0.07	6.66 ± 4.40	0.44 ± 0.24	1.32
	induced	1.05 ± 0.11	3.59 ± 3.04	0.29 ± 0.23	1.50
TTLL12B	non-induced	1.42 ± 0.15	4.55 ± 2.85	0.45 ± 0.25	1.08
	induced	0.79 ± 0.09	1.41 ± 1.79	0.21 ± 0.22	1.59

Table 6: Results of statistical motility analysis on *T. brucei's* parental procyclic (wild type) form, and RNAi constructs with and without induction, including mean values of: anomaly exponents α, instantaneous velocities v and straightness S; and median values of helical frequency ν_h. Note that helical frequencies could only be calculated for conditions with at least a fraction of persistent motion, hence excluding lysine-coating data from the analysis.

7. Discussion

The motion of unaltered *trypanosomes* showed a clear run- and tumble-like signature with persistent movement in a specific direction followed by a reorientation phase, where parasites seemed to test their local environment before starting to 'run' again. The anomaly exponents extracted from individual SPT trajectories ($\langle\alpha\rangle \approx 1.5$) were expected for the observed type of motion, since they represent a crossover of directed motion with diffusive phases. These results are in excelent agreement with previous findings [163]. Superficial visual inspection of non-induced cells of the RNAi subpopulations (TTLL6A- and TTLL12B-) did not reveal any gross changes in motion pattern compared to the wild-type parasites. In fact, diffusion anomalies and straightness' for all three conditions have been found to be in excellent agreement. The PDFs of straightness values extracted from individual trajectories showed expected large variations around a mean $\langle S\rangle \approx 0.44$, due to the heterogeneity of individual tracks. Almost all acquired trajectories showed an alternating motion with distinct run- and tumble-phases. Extracted instantaneous velocities were found to be in good agreement with previous results $\langle v\rangle = 10\,\mu\mathrm{m/s}$ presented by Engstler and Pfohl [163, 164] for wild-type and non-induced conditions. In general, individuals of the TTLL6A- population showed a tendency to slightly higher velocities with broader variation, whereas TTLL12B- individuals seemed to have overall lower velocities. However, the three conditions did not show significant differences. Therefore non-induced individuals seemed to behave like the wild-type parasites to a reasonable degree of scientific certainty. The helical frequency showed broad trajectory-to-trajectory variations in a non-symmetrical distribution with a marked peak and a median value of $\tilde{\nu_\mathrm{h}} \approx 1.2\,\mathrm{Hz}$ for the wild-type and non-induced RNAi conditions alike. In contrast to the presented result, a similar study by Heddergott et. al found the projection of parasites motion to be a wave pattern with a frequency of approximately 2...3 Hz [183]. However, they mainly looked into the beating of the flagellum which indeed is slightly faster than the motion of the center of mass of parasites. Therefore, observed helical frequencies appear reasonable. Strong variations in the data can be explained, since analyzed trajectory segments could have slight curvatures even in presumable persistent run-phases. Moreover, the crossover from persistent to more diffusive motion cannot be fully neglected from the analysis, hence making larger deviations more reasonable. However, the general shape of the PDFs of non-induced data sets were in good agreement with the parental data.

Upon inducing polyglutamylase depletion, all observables changed drastically. First, a significant shift of anomaly exponents to values $\langle\alpha\rangle \approx 1$ was observed for the TTLL6A+ subpopulation. Depletion of TTLL12B led to an even more pronounced decrease to $\langle\alpha\rangle \approx 0.8$. These findings might seem curious, since the trajectories from individuals of both induced populations show presumably persistent motion on a longer timescale (representative tra-

jectories shown in Fig.6.4 are at least 20 s long). However, the anomaly exponents were extracted in the range $0.1\,\mathrm{s} \leq \tau \leq 1\,\mathrm{s}$, and thus motion behavior was analyzed on shorter timescales. The second indicator of changes in the mode of motion, $p(v)$, revealed similar results. Knocking down TTLL6A (TTLL12B) decreased the instantaneous velocity by a factor two (three). A decreasing velocity can only be reasoned by either a smaller mean step size or less directed motion, both of which indicates highly significant changes in the motility. The directionality of *trypanosomes'* motion was probed using the straightness. It was found that depletion of TTLL6A or TTLL12B led to a significant reduction of S, i.e. the treatment seemed to enhance the fraction of tumbling motion phases. Again, depletion of TTLL12B showed a stronger effect. The helical frequency was employed to directly probe the intrinsic corkscrew like motion pattern during more persistent motion. It was found that polyglutamylation deficiencies promote higher helical frequencies, i.e. tracks of individual *trypanosomes* have on average smaller wavelength. This phenomenon implicates a change in the beating flagellum. However, it is not clearly know at this point, whether the flagellum itself is presumably shortened or if changes in the subpellicular cortex promote a possible increase of frequency in another way. Having that said, TTLL depletion led to presumably less stiff cortex' of the parasites, which in turn seemed to influence the bending and turning in the corkscrew-like motion during run phases, i.e. probably promoting higher curvatures of *trypanosomes*. However, more in depth analysis is necessary to gain more insights and to eventually confirm this assumption.

Adding up, it was found that despite no apparent change in the phenotype, significant changes in motility were observed, when either TTLL6A or TTLL12B were depleted. The anomaly exponents and straightness values indicated a shift towards presumably more erratic or diffusion like motion, i.e. the fraction of persistent run phases seemed to decrease. A decrease in instantaneous velocity combined with the findings for the helical frequency and superficial visual inspection of representative trajectories hint towards on average smaller step increments of individual parasites. Since the motility of *trypanosomes* is mediated by the flagellum, these results could be induced by changes in flagellar biology. Changes in axonemal polyglutamylation in the flagellum after depletion of either TTLL construct were quantified by immunofluorescence in cooperation with the group of molecular parasitology (Prof. Ehrsfeld, UBT). It was found that TTLL6A depletion led to a significant decrease ($\approx -30\%$) in flagellar fluorescence, while TTLL12B depletion again showed an even stronger effect. The latter treatment reduced the fluorescent intensity by approximately 70%. Therefore, it was shown that a knockdown of either putative tubulin polyglutamylase in *T. brucei* – TTLL6A and TTLL12B – resulted in significant changes in the cells motility. These changes are presumably due to a lower fraction of persistent run phases combined with smaller average step increments. Despite the observed more erratic diffusive motion of individuals on short timescales ($\langle\alpha\rangle \lessapprox 1$ for $\tau \leq 1\,\mathrm{s}$), an apparent crossover to presumably more 'normal' persistent motion was observed for some indi-

viduals for longer times by superficial visual inspection of trajectories. This behavior was more pronounced for the TTLL6A+ subpopulation. However, the physical and biological properties promoting such a crossover still stay illusive.

In summary, the presented data showed that microtubule posttranslational polyglutamylation is very likely a key parameter in the regulation of cytoskeletal architecture, and thus influencing motility in *tryponosomes*.

Summary & outlook

Generally recapitulating the results achieved during the course of this thesis: new insights on the motion behavior and the underlying mechanisms that cause the emergence of spatiotemporal heterogeneity in individual and ensemble data acquired with single particle tracking of (i) fluctuation-driven nanoparticles in the cytoplasm of HeLa cells, and (ii) actively self-propelled *T. brucei* parasites, were revealed.

Beginning with the quantum dots analysis, heterogeneous and intermittent subdiffusion in the cytoplasm of living cells was observed that was altered upon disrupting the cytoskeleton or fragmenting the ER network. At first, the motion was characterized by established estimators like the anomaly exponent α, the generalized transport coefficient K_α, and the velocity autocorrelation function $C_v(\tau)$. It was found that trajectories on average showed a marked subdiffusion with anomalies and generalized transport coefficients comparable to previous observations [6, 30, 136]. A strong dependency on the integrity of microtubules and the ER network was observed, whereas depolymerization of actin filaments merely showed any effect on the PDFs of α and K_α. Evaluation of the rescaled VACF showed exceptional agreement of the experimental data with the analytical prediction for fBM without any fitting parameter. This led to the conclusion that the underlying transport process is of fractional Brownian motion type, presumably due to the crowded viscoelastic environment found in the cytoplasm. In an attempt to gain more insight in the underlying mechanism, new estimators were established in the context of anomalous diffusion that showed clear signatures of heterogeneity in individual trajectories. These estimators are: The distribution of normalized increments $p(\chi)$, the local convex hull and specifically its largest diameter S_d, and the correlation function of squared increments $G(\tau)$. A non-trivial decay in $G(\tau)$ and the deviation from the anticipated Gaussian shape of $p(\chi)$ for small time lags δt suggest that individual trajectories are heterogeneous, i.e. the particles mobility changes within the trajectory. To probe this directly, the LCH was employed and its largest diameter was calculated for individual trajectories over time. Indeed, the analysis confirmed the existence of at least two mobility states for untreated and nocodazole-treated cells. Again, this indicates heterogeneities in the ensemble and in individual trajectories. The causes of the heterogeneity were traced to transient interactions of the quantum dots to the ubiquitous ER membranes, which hamper free diffusion in a crowded environment and in turn enforce a particularly low anomaly exponent. In the case of an intact ER, association to the network leads to an intermittent diffusion process in which the motion of the tracer particles is indirectly coupled to active microtubule-based processes. To test this hypothesis, an intermittent fractional Brownian motion model, in which the anomaly exponents were set to values found for motion of ER junctions in untreated cells and cells where microtubules network integrity was perturbed using nocodazole, was derived.

Despite the simplicity of the model, it described the experimentally obtained data very well. This is remarkable, since most models describing intracellular subdiffusion rely on a distribution of 'diffusing diffusivities', while the model presented in this work only requires two fixed inputs. However, not all mysteries of intracellular transport could be lifted. The cause of the persisting strongly subdiffusive type of motion after fragmentation of the ER network stays illusive. Additional structures, like the intermediate filament network, or the membrane vesicles mimicing a microemulsion, are potential candidates for further unspecific interaction or sterical obstruction. Hence, focusing on these structures and their interactions with other organelles in the cell would presumably yield new insights for future studies. Since mainly interphase cells were analyzed in this study, observation of quantum dots motion in other cell cycle phases – like metaphase – could lead to a higher understanding of fluctuation-driven and directed processes during proliferation. Moreover, could the newly established estimators be studied in more detail and eventually be applied to a plethora of transport and diffusion related scientific questions, not only in biological specimen.

In a second part, the effects of microtubule polyglutamylation deficiencies on the motility of *T. brucei* individuals was studied. Using RNA interference, two subpopulations of the parental 29-13 procyclic form were generated, which show depletion of polyglutamylase using either the TTLL6A or TTLL12B pathway upon induction with doxycycline. Individuals were observed using bright field microscopy with subsequent SPT. To analyze the movement, a motility assay was established, that included the anomaly exponents α extracted from TA-MSDs, the instantaneous velocities v, an estimator of directionality called the straightness S, and the helical frequency along the predominant direction of motion ν_{h}. Non-induced individuals of either mutant population did not show significant deviations from the wildtypes run-and-tumble-like motion behavior. However, upon induction, significant changes to more diffusive motion (TTLL6A) or even signatures of subdiffusion (TTLL12B) were found. Knocking down either protein not only reduced the average velocities by a great margin but also led to less straight trajectories and a shift to higher helical frequencies. These findings indicate that treatment enhances the tumbling motion over *trypanosomes'* running phases, supposedly reflecting changes in cell stiffness due to perturbations of the subpellicular cortex, or action of the flagellum, or both. Hence, microtubule posttranslational polyglutamylation is in fact a key parameter in the regulation of cytoskeletal architecture, cell shape and motility. However, it is not fully understood, in what extent the deviations form wildtype motion behavior are promoted by microtubule structures in the cortex or in the flagellum. Moreover, the crossover from super- to normal diffusion as well as the changes in center-of-mass motion, i.e. the corkscrew-like motion, have to be studied in more depth to fully reveal all facets of the underlying mechanism. Nevertheless, *trypanosomes* have been proven to be a relatively easy to handle specimen for observations on active transport processes and motion, with interesting scientific questions.

Adding up, single particle tracking methods combined with statistical motion analysis was shown to be a powerful tool to extract the features of distinct transport and motion behavior of biological specimen on a multitude of length scales; from the nanometer sized quantum dots to the exploration paths of a blood stream parasites of up to 100 µm extent.

List of abbreviations

ATP	Adenosine triphosphate
BF	Bright field
BSA	Bovine serum albumin
BCS	Bovine calf serum
cLSM	Confocal laser scanning microscope
CLT	Central limit theorem
CNX	Calnexin
CRT	Calreticulin
CTRW	Continuous time random walk
CytD	Cytochalasin D
D10	Cell culture medium
DIC	Differential interference contrast
DMEM	Dulbecco's minimal essential medium
DMSO	Dimethyl sulfoxide
EMCCD	Electron multiplying charged coupled device
ER	Endoplasmic reticulum
fBM	Fractional Brownian motion
FCS	Fluorescence correlation spectroscopy
FLIM	Fluorescence lifetime imaging microscopy
FRAP	Fluorescence recovery after photobleaching
FRET	Förster (fluorescence) resonance energy transfer
FWHM	Full width at half maximum
GFP	Green fluorescent protein
HeLa	Immortal cervical cancer cell line taken from Henrietta Lacks
Hoechst	BisBenzimide H 33342 trihydrochloride
LAP	Linear assignment problem
LatA	Latrunculin A
LCH	Local convex hull
MAP	Microtubule associated protein
mRNA	Messenger ribonucleic acid
MSD	Mean squared displacement
MT	Microtubule
NA	Numerical aperture
ND	Neutral density
Noc	Nocodazole
O-U	Ohrnstein-Uhlenbeck
PBS	Phosphate-buffered saline
PDF	Probability density function
PTM	Post-translational modification
Qdot	Quantum dot
RISC	RNA-induced silencing complex
RNA	Ribonucleic acid
RNAi	RNA interference
SEM	Scanning electron microscopy
siRNA	Small interfering RNA
SNR	Signal-to-noise ratio
SPT	Single particle tracking
TA-MSD	Time-averaged MSD
TEM	Transmission electron microscopy
TIRF	Total internal reflection
TTLL	Tubulin-tyrosine ligase like
T. brucei	Tryponosoma brucei
VACF	Velocity autocorrelation function
WT	Wild type (parental 29-13 procyclic form) of *T. brucei*

Appendix

A.1. Other methods of determining principles of diffusion

Accessing the dynamics in living cells with non-invasive techniques capable of visualizing processes with high spatiotemporal resolution and sensitivity is central during the course of this work. As mentioned in Sec.3.1, SPT is one of the key methods used in biophysics for gathering information on the dynamics of intracellular tracers, but there are other techniques that show insights into the dynamics of living cells as well, some of which are reported on in the following paragraphs.

Fluorescence correlation spectroscopy Another powerful technique to determine the dynamics of small tracers like molecules in living cells is fluorescence correlation spectroscopy (**FCS**). In contrast to SPT, this method is a bulk measurement, i.e. it analyzes the fluctuations $\delta F(t)$ of the fluorescence intensity $F(t)$ that arises from the passage of a dilute number of labeled molecules N with concentration $\langle C \rangle$ over a distinct focal illumination volume $V_{\text{eff}} = \pi^{3/2} r_0^2 z_0$. When ergodicity is assumed, the normalized temporal averaged autocorrelation of these fluctuations for certain lag times τ in three dimensions gives insight into the bulk diffusion behavior via Eq.A.2.

$$G(\tau) = \frac{\langle \delta F(t) \cdot \delta F(t+\tau) \rangle}{\langle F(t) \rangle^2} \tag{A.1}$$

$$= \frac{1}{V_{\text{eff}} \langle C \rangle} \frac{1}{(1 + (\tau/\tau_D)^{\alpha})} \frac{1}{\sqrt{1 + (r_0/z_0)^2 \cdot (\tau/\tau_D)^{\alpha}}}, \text{ for } 0 < \alpha \leq 1 \tag{A.2}$$

Hence, the analysis provides average particle numbers of molecules $(V_{\text{eff}} \langle C \rangle)^{-1}$ and average residence time of the fluorophore in the observation volume, i.e. diffusion times τ_D. In general, the diffusion coefficient of the molecules can be determined via $D = r_0^2/4\tau_D$.
For more detailed insights in the FCS measurement technique and further applications see [13, 184–187].

Fluorescence recovery after photobleaching One of the most widespread techniques used in biology for uncovering intracellular dynamics is fluorescent recovery after photobleaching (**FRAP**). This technique was popularized in the late 1970s as a means to characterize the mobility of individual lipid molecules within a cell membrane [188]. In recent years FRAP is used to quantify diffusion-reaction dynamics in the cyto- and nucleoplasm of cells as well [189]. During FRAP experiments, the fluorescently labeled molecules of a specific region of interest in the cell are switched-off by a photo physical process called photobleaching. Afterwards, the mobility of the molecules is measured by the recovery of intensity in this specific region. The recovery curve is determined by the rate of diffusion

of new molecules into the bleached area (diffusion limited), or the rate bleached proteins unbind from their respective site and are replaced by still fluorescent proteins (reaction limited). In the diffusion limit scenario, where molecules with diffusion coefficient D are much faster than reaction kinetics takes place, and assuming an instantaneous circular bleach spot with radius ω, the temporal evolution of the fluorescence is described as [190]:

$$F(t) \propto e^{-\frac{2\tau_D}{t}}, \text{ with } \tau_D = {}^{\omega^2}/_{4D}. \tag{A.3}$$

On the other hand, if the number of proteins that bind to a small volume is large and hence the fluorescent signal in the bleached region is dominated by the bound proteins' signal which have a constant unbinding rate k_{off}, the time dependent fluorescent recovery can be estimated to be:

$$F(t) \propto 1 - e^{-k_{\text{off}}(t-t_0)}. \tag{A.4}$$

Note here that even if equation Eq.A.4 only dependents on the unbinding rate, some other assumptions have to be made: the binding rate has to be sufficiently large, the sites do not move, and the transport mechanism has to be instantaneous, i.e. in this limit the bound lifetime is $k_{\text{off}}^{-1} \gg {}^{\omega^2}/_{D}$.

In general, the recovered fluorescence intensity will not only be determined by one or the other mechanism, but a combination of both processes - simple isotropic diffusion and reaction kinetics - play an important role. Since this thesis' main objectives were not measured using FRAP, the reader is adviced to consult the following publications for more detailed information [186, 189, 191].

Fluorescence lifetime imaging microscopy In typical fluorescent microscopy applications, the localization is done via the intensity of the emitted photon, but that is not the only quantity that can be extracted from experiments. Fluorophores have typical differences in the decay rate of their respective fluorescence k_{f}, thus resulting in a specific fluorescent lifetime of the molecules that can be mapped. Fluorescent lifetime imaging microscopy (**FLIM**), uses this typical time a molecule remains in the excited state rather than its intensity, hence minimizing the effects of photon scattering especially in thick layered specimen. The actual intensity of each pixel of the image $I(t) = I_0 \cdot \exp\{-{}^{t}/_{\tau}\}$ is determined by the the lifetime $\tau = (\sum k_i)^{-1}$, where k_i are the rates of each individual decay pathway of which at least one must be fluorescent with k_{f}. Note that τ is independent of the initial intensity I_0 and hence allowing to view contrast in materials in the images only dependent on the different decay rates. In fact, these acquisition method produces images which show changes in other pathways as well. One of these is Förster (fluorescent) resonance energy transfer (**FRET**) which will be only mentioned here. For more information on these topics see [192–195].

A.2. Cell culture protocols

HeLa cell line maintenance: splitting

- aspirate the old medium with the vacuum pump and glass pipettes
- wash the dish 1× with prewarmed PBS
- add 4 ml trypsine (at 0.25%)
- incubate 2 minutes at 37 °C
- loosen the attached cells by shaking the dish and add 6 ml D10
- transfer the cells in 10 ml solution to an appropriate centrifuge tube
- centrifuge the cells in solution for 2 min at 200 × g
- aspirate the supernatant and dilute the palette in 2.5 ml D10
- prepare a cell culture flask with 8 ml D10 and add an appropriate amount of diluted cells (e.g. 1 ml)

Cell cycle synchronization

- plate cells to be 80% confluent
- aspirate the old medium with the vacuum pump and glass pipettes
- wash the dish 1× with prewarmed PBS
- dilute 5 µl Noc ($c = 3\,\mu g/ml$) in 1 ml D10 to create medium with 0.5% nocodazole concentration
- add a sufficient amount of the dilution to the the plated dish
- incubate the dish with nocodazole for 12 to 18 hours (overnight) at 37 °C in 5% CO_2 atmosphere
- since cells might not be fully adherent, gently wash the dish 3× with PBS
- add a sufficient amount of imaging medium and let cells recover for 30 min at 37 °C in 5% CO_2 atmosphere before imaging

Lipofectamine transfection

- plate 50,000 cells in each ibidi four well plate chamber the day before transfection
- dilute 2.25 µl lipofectamine 3000 reagent in 75 µl Opti-MEM and mixed well
- dilute 3 µg of DNA (CRT-GFP stored at a $c = 0.92\,\mu g/\mu l$, CNX-GFP stored at $c = 0.43\,\mu g/\mu l$, measured with the nanodrop method using a *Genesys UV/Vis Spectrophotometer*, ThermoFisher) in another 75 µl Opti-MEM
- mix DNA dilution with 1 µl P3000™ per 1 µg DNA
- add the diluted DNA in P3000™ to the Lipofectamine™ 3000 reagent in a (1:1) ratio
- incubate the mixed dilutions for $10 - 15$ min

Best transfection efficiencies are achieved, when cells are analyzed after a $2 - 4$ days period of incubation at 37 °C in 5% CO_2 atmosphere [145].

Bead loading

- plate cells to be 80% confluent on round 35 mm glass bottom dishes
- aspirate the old medium with the vacuum pump and glass pipettes
- wash the dish 1× with prewarmed PBS
- aspirate all liquid from the cells surface
- add 8 µl quantum dots working solution on top of the cells
- gently place a monolayer of monodisperse glass beads with a diameter of 100 µm on the specimen
- hold the dish between index finger and thumb and tap it approximately 8 times with force from ≈ 4 cm height onto the working bench without breaking the glass bottom
- add 800 µl prewarmed D10 and let cells recover for $30 - 45$ min at 37 °C in 5% CO_2 atmosphere
- gently wash of glass beads $(1 - 3)\times$ with PBS without washing off cells
- add a sufficient amount of imaging medium (at least 800 µl) before imaging

List of publications

Published

1. Adal Sabri, Xinran Xu, Diego Krapf, and Matthias Weiss
   Elucidating the Origin of Heterogeneous Anomalous Diffusion in the Cytoplasm of Mammalian Cells
   Phys. Rev. Lett., **125**, 058101 (2020)

2. Jana Jentzsch, Adal Sabri, Konstatin Speckner, Gertrud Lallinger-Kube, Matthias Weiss, and Klaus Ersfeld
   Microtubule polyglutamylation is important for regulating cytoskeletal architecture and motility in Trypanosoma brucei
   J. Cell Sci., **133**, jcs248047 (2020)

In preparation

1. Christine Selhuber-Unkel, Matthias Weiss, Shane Scott, Younes Barooji, Adal Sabri, Janine Erler, Ralf Metzler, and Lene Oddershede
   Systematically extracting, quantifying and comparing dynamical and biomechanical properties of living matter
   Review Article

References

1. Brown, R. Mikroskopische Beobachtungen über die im Pollen der Pflanzen enthaltenen Partikeln, und über das allgemeine Vorkommen activer Molecüle in organischen und unorganischen Körpern. *Annalen der Physik* **90,** 294–313 (1828).
2. Brockmann, D. & Geisel, T. The ecology of gaze shifts. *Neurocomputing* **32-33,** 643 –650 (2000).
3. Dingle, H. & Drake, V. A. What is migration? *Bioscience* **57,** 113–121 (2007).
4. Merritt, D. *Dynamics and evolution of galactic nuclei* (Princeton University Press, 2013).
5. Reid, M. J. & Brunthaler, A. The proper motion of Sagittarius A*. II. The mass of Sagittarius A. *The Astrophysical Journal* **616,** 872 (2004).
6. Höfling, F. & Franosch, T. Anomalous transport in the crowded world of biological cells. *Reports on Progress in Physics* **76,** 046602 (2013).
7. Einstein, A. On the theory of the Brownian movement. *Annalen der Physik* **19,** 371–381 (1906).
8. Von Smoluchowski, M. Zur kinetischen Theorie der Brownschen Molekularbewegung und der Suspensionen. *Annalen der Physik* **326,** 756–780 (1906).
9. Fick, A. Über Diffusion. *Annalen der Physik* **170,** 59–86 (1855).
10. Vale, R. D. The molecular motor toolbox for intracellular transport. *Cell* **112,** 467–480 (2003).
11. Weiss, M., Elsner, M., Kartberg, F. & Nilsson, T. Anomalous subdiffusion is a measure for cytoplasmic crowding in living cells. *Biophysical Journal* **87,** 3518–3524 (2004).
12. Metzler, R., Jeon, J.-H., Cherstvy, A. G. & Barkai, E. Anomalous diffusion models and their properties: non-stationarity, non-ergodicity, and ageing at the centenary of single particle tracking. *Physical Chemistry Chemical Physics* **16,** 24128–24164 (2014).
13. Malchus, N. & Weiss, M. Elucidating anomalous protein diffusion in living cells with fluorescence correlation spectroscopy—facts and pitfalls. *Journal of Fluorescence* **20,** 19–26 (2010).
14. Pawar, N., Donth, C. & Weiss, M. Anisotropic diffusion of macromolecules in the contiguous nucleocytoplasmic fluid during eukaryotic cell division. *Current Biology* **24,** 1905–1908 (2014).
15. Weiss, M. in *International review of cell and molecular biology* 383–417 (Elsevier, 2014).

16. Metzler, R. & Klafter, J. The random walk's guide to anomalous diffusion: a fractional dynamics approach. *Physics reports* **339,** 1–77 (2000).

17. Metzler, R. & Klafter, J. Subdiffusive transport close to thermal equilibrium: from the Langevin equation to fractional diffusion. *Physical Review E* **61,** 6308 (2000).

18. Burov, S., Jeon, J.-H., Metzler, R. & Barkai, E. Single particle tracking in systems showing anomalous diffusion: the role of weak ergodicity breaking. *Physical Chemistry Chemical Physics* **13,** 1800–1812 (2011).

19. Cherstvy, A. G., Chechkin, A. V. & Metzler, R. Anomalous diffusion and ergodicity breaking in heterogeneous diffusion processes. *New Journal of Physics* **15,** 083039 (2013).

20. Pöschke, P., Sokolov, I. M., Nepomnyashchy, A. A. & Zaks, M. A. Anomalous transport in cellular flows: The role of initial conditions and aging. *Physical Review E* **94,** 032128 (2016).

21. Chechkin, A. V., Seno, F., Metzler, R. & Sokolov, I. M. Brownian yet non-Gaussian diffusion: from superstatistics to subordination of diffusing diffusivities. *Physical Review X* **7,** 021002 (2017).

22. Wong, I. *et al.* Anomalous diffusion probes microstructure dynamics of entangled F-actin networks. *Physical Review Letters* **92,** 178101 (2004).

23. Weigel, A. V., Simon, B., Tamkun, M. M. & Krapf, D. Ergodic and nonergodic processes coexist in the plasma membrane as observed by single-molecule tracking. *Proceedings of the National Academy of Sciences* **108,** 6438–6443 (2011).

24. Ernst, D., Hellmann, M., Köhler, J. & Weiss, M. Fractional Brownian motion in crowded fluids. *Soft Matter* **8,** 4886–4889 (18 2012).

25. Ernst, D., Köhler, J. & Weiss, M. Probing the type of anomalous diffusion with single-particle tracking. *Physical Chemistry Chemical Physics* **16,** 7686–7691 (2014).

26. Xue, C., Zheng, X., Chen, K., Tian, Y. & Hu, G. Probing Non-Gaussianity in Confined Diffusion of Nanoparticles. *The Journal of Physical Chemistry Letters* **7,** 514–519 (2016).

27. Sadoon, A. A. & Wang, Y. Anomalous, non-Gaussian, viscoelastic, and age-dependent dynamics of histonelike nucleoid-structuring proteins in live Escherichia coli. *Physical Review E* **98,** 042411 (2018).

28. Zhou, H.-X., Rivas, G. & Minton, A. P. Macromolecular crowding and confinement: biochemical, biophysical, and potential physiological consequences. *Annu. Rev. Biophys.* **37,** 375–397 (2008).

29. Donth, C. & Weiss, M. Quantitative assessment of the spatial crowding heterogeneity in cellular fluids. *Physical Review E* **99,** 052415 (2019).

30. Etoc, F. *et al.* Non-specific interactions govern cytosolic diffusion of nanosized objects in mammalian cells. *Nature materials* **17,** 740–746 (2018).

31. Buttinoni, I., Volpe, G., Kümmel, F., Volpe, G. & Bechinger, C. Active Brownian motion tunable by light. *Journal of Physics: Condensed Matter* **24,** 284129 (2012).

32. Volpe, G., Volpe, G. & Gigan, S. Brownian motion in a speckle light field: tunable anomalous diffusion and selective optical manipulation. *Scientific reports* **4,** 3936 (2014).

33. Regner, B. M. *et al.* Anomalous diffusion of single particles in cytoplasm. *Biophysical Journal* **104,** 1652–1660 (2013).

34. Tolić-Nørrelykke, I. M., Munteanu, E.-L., Thon, G., Oddershede, L. & Berg-Sørensen, K. Anomalous diffusion in living yeast cells. *Physical Review Letters* **93,** 078102 (2004).

35. Einstein, A. *Investigations on the Theory of the Brownian Movement* (Courier Corporation, 1956).

36. Langevin, P. Sur la théorie du mouvement brownien. *Compt. Rendus* **146,** 530–533 (1908).

37. Walters, P. *An introduction to ergodic theory* (Springer Science & Business Media, 2000).

38. Fließbach, T. *Statistische Physik* (Springer, 1993).

39. Abry, P. & Sellan, F. *The wavelet-based synthesis for fractional Brownian motion proposed by F. Sellan and Y. Meyer: Remarks and fast implementation* 1996.

40. Bardet, J.-M., Lang, G., Oppenheim, G., Philippe, A. & Taqqu, M. S. Generators of long-range dependent processes: a survey. *Theory and applications of long-range dependence,* 579–623 (2003).

41. He, Y, Burov, S, Metzler, R. & Barkai, E. Random time-scale invariant diffusion and transport coefficients. *Physical Review Letters* **101,** 058101 (2008).

42. Montroll, E. W. Random Walks on Lattices. III. Calculation of First-Passage Times with Application to Exciton Trapping on Photosynthetic Units. *Journal of Mathematical Physics* **10,** 753–765 (1969).

43. Kramers, H. Brownian motion in a field of force and the diffusion model of chemical reactions. *Physica* **7,** 284 –304 (1940).

44. Bel, G. & Barkai, E. Weak Ergodicity Breaking in the Continuous-Time Random Walk. *Physical Review Letter* **94,** 240602 (24 2005).

45. Ben-Avraham, D & Havlin, S. Diffusion on percolation clusters at criticality. *Journal of Physics A: Mathematical and General* **15,** L691–L697 (1982).

46. Havlin, S., Ben-Avraham, D. & Sompolinsky, H. Scaling behavior of diffusion on percolation clusters. *Physica Review A* **27,** 1730–1733 (1983).

47. Jan, N. Large lattice random site percolation. *Physica A: Statistical Mechanics and its Applications* **266,** 72 –75 (1999).

48. Jacobsen, J. L. High-precision percolation thresholds and Potts-model critical manifolds from graph polynomials. *Journal of Physics A: Mathematical and Theoretical* **47,** 135001 (2014).

49. Nienhuis, B. Critical behavior of two-dimensional spin models and charge asymmetry in the Coulomb gas. *Journal of Statistical Physics* **34,** 731–761 (1984).

50. Lorenz, C. D. & Ziff, R. M. Precise determination of the critical percolation threshold for the three-dimensional "Swiss cheese" model using a growth algorithm. *The Journal of Chemical Physics* **114,** 3659–3661 (2001).

51. Alexander, S. & Orbach, R. Density of states on fractals : " fractons ". *J. Physique Lett.* **43,** 625–631 (1982).

52. Klemm, A., Metzler, R. & Kimmich, R. Diffusion on random-site percolation clusters: Theory and NMR microscopy experiments with model objects. *Physical Review E* **65,** 021112 (2002).

53. Saxton, M. Lateral diffusion in an archipelago. Dependence on tracer size. *Biophysical Journal* **64,** 1053 –1062 (1993).

54. Mandelbrot, B. B. & Mandelbrot, B. B. *The fractal geometry of nature* Updated and augmented [ed.] English, 468, C16 p. : ISBN: 0716711869 (W.H. Freeman New York, 1983).

55. Minton, A. P. Join the crowd. *Nature* **425,** 27–28 (2003).

56. Guigas, G., Kalla, C. & Weiss, M. Probing the nanoscale viscoelasticity of intracellular fluids in living cells. *Biophysical Journal* **93,** 316–323 (2007).

57. Krapf, D. in *Current topics in membranes* 167–207 (Elsevier, 2015).

58. Sokolov, I. M. Models of anomalous diffusion in crowded environments. *Soft Matter* **8,** 9043–9052 (2012).

59. Szymanski, J. & Weiss, M. Elucidating the origin of anomalous diffusion in crowded fluids. *Physical Review Letters* **103,** 038102 (2009).

60. Weber, S. C., Spakowitz, A. J. & Theriot, J. A. Bacterial chromosomal loci move subdiffusively through a viscoelastic cytoplasm. *Physical Review Letters* **104,** 238102 (2010).

61. Mason, T. G. & Weitz, D. A. Optical Measurements of Frequency-Dependent Linear Viscoelastic Moduli of Complex Fluids. *Physical Review Letter* **74,** 1250–1253 (1995).

62. Weiss, M. A tale about square dancers and maze runners. *Nature materials* **17,** 655–656 (2018).

63. Sims, D. W. *et al.* Scaling laws of marine predator search behaviour. *Nature* **451,** 1098–1102 (2008).

64. Jamil, M. & Zepernick, H.-J. in *Swarm Intelligence and Bio-Inspired Computation* 49 –72 (Elsevier, Oxford, 2013). ISBN: 978-0-12-405163-8.

65. Campos, D., Méndez, V. & Llopis, I. Persistent random motion: Uncovering cell migration dynamics. *Journal of theoretical Biology* **267,** 526–534 (2010).

66. Uhlenbeck, G. E. & Ornstein, L. S. On the theory of the Brownian motion. *Physical Review* **36,** 823 (1930).

67. Fürth, R. Die Brownsche Bewegung bei Berücksichtigung einer Persistenz der Bewegungsrichtung mit Anwendungen auf die Bewegung lebender Infusorien. *Zeitschrift für Physik* **2,** 244–256 (1920).

68. Skloot, R. *The Immortal Life of Henrietta Lacks* ISBN: 0307888444 (Crown Pub, 2011).

69. Alberts, B. *Essential Cell Biology* ISBN: 081534130X (Kyobo Book Co., 2020).

70. Kelvinsong. *Wikimedia Commons* Dec. 2010. `https://upload.wikimedia.org/wikipedia/commons/1/11/Animal_Cell.svg`.

71. Wiley. *Encyclopedia of Life Sciences, 20 Volume Set* ISBN: 0470016175 (Wiley, 2005).

72. Nixon-Abell, J. *et al.* Increased spatiotemporal resolution reveals highly dynamic dense tubular matrices in the peripheral ER. *Science* **354** (2016).

73. Ledbetter, M. C. & Porter, K. R. A "microtubule" in plant cell fine structure. *Journal of Cell Biology* **19,** 239–250 (1963).

74. Cooper, G. *The Cell: A Molecular Approach* ISBN: 9780878931064 (Sinauer Associates Inc, 2000).

75. Footer, M. J., Kerssemakers, J. W. J., Theriot, J. A. & Dogterom, M. Direct measurement of force generation by actin filament polymerization using an optical trap. *Proceedings of the National Academy of Sciences* **104,** 2181–2186 (2007).

76. Pelham, R. J. & Chang, F. Actin dynamics in the contractile ring during cytokinesis in fission yeast. *Nature* **419,** 82–86 (2002).

77. Cooper, J. The role of actin polymerization in cell motility. *Annual Review of Physiology* **53,** 585–605 (1991).

78. Yarar, D., Waterman-Storer, C. M. & Schmid, S. L. A Dynamic Actin Cytoskeleton Functions at Multiple Stages of Clathrin-mediated Endocytosis. *Molecular Biology of the Cell* **16,** 964–975 (2005).

79. Yamazaki, M., Furuike, S. & Ito, T. in *Mechanics of Elastic Biomolecules* 525–534 (Springer Netherlands, 2003).

80. Edde, B *et al.* Posttranslational glutamylation of alpha-tubulin. *Science* **247,** 83–85 (1990).

81. Siekevitz, P. Powerhouse of the Cell. *Scientific American* **197,** 131–144 (1957).

82. Wiemerslage, L. & Lee, D. Quantification of mitochondrial morphology in neurites of dopaminergic neurons using multiple parameters. *Journal of Neuroscience Methods* **262,** 56–65 (2016).

83. McBride, H. M., Neuspiel, M. & Wasiak, S. Mitochondria: More Than Just a Powerhouse. *Current Biology* **16,** R551–R560 (2006).

84. Andersson, S. G. E. *et al.* The genome sequence of Rickettsia prowazekii and the origin of mitochondria. *Nature* **396,** 133–140 (1998).

85. Andersson, G. E., Karlberg, O., Canbäck, B. & Kurland, C. G. On the origin of mitochondria: a genomics perspective. *Philosophical Transactions of the Royal Society of London. Series B: Biological Sciences* **358** (eds Allen, J. F. & Raven, J. A.) 165–179 (2003).

86. Shepherd, V. The Cytomatrix as a Cooperative System of Macromolecular and Water Networks. *Current Topics in Developmental Biology* **75,** 171 –223 (2006).

87. Ellis, R. J. Macromolecular crowding: obvious but underappreciated. *Trends in Biochemical Sciences* **26,** 597–604 (2001).

88. Fulton, A. B. How crowded is the cytoplasm? *Cell* **30,** 345–347 (1982).

89. Lampo, T. J., Stylianidou, S., Backlund, M. P., Wiggins, P. A. & Spakowitz, A. J. Cytoplasmic RNA-protein particles exhibit non-Gaussian subdiffusive behavior. *Biophysical Journal* **112,** 532–542 (2017).

90. Metzler, R. Gaussianity fair: the riddle of anomalous yet non-Gaussian diffusion. *Biophysical Journal* **112,** 413 (2017).

91. Kultys, M. *Wikimedia Commons* July 2008. `https://commons.wikimedia.org/w/index.php?curid=33362276`.

92. Parry, D. H., Hickson, G. R. & O'Farrell, P. H. Cyclin B Destruction Triggers Changes in Kinetochore Behavior Essential for Successful Anaphase. *Current Biology* **13,** 647 –653 (2003).

93. Stoker, M. G. P. & Rubin, H. Density Dependent Inhibition of Cell Growth in Culture. *Nature* **215,** 171–172 (1967).

94. Costello, G., Rodgers, L. & Beach, D. Fission yeast enters the stationary phase G0 state from either mitotic G1 or G2. *Current Genetics* **11,** 119–125 (1986).

95. Gray, J. V. *et al.* "Sleeping Beauty": Quiescence in Saccharomyces cerevisiae. *Microbiology and Molecular Biology Reviews* **68,** 187–206 (2004).

96. Laporte, D. & Sagot, I. Microtubules move the nucleus to quiescence. *Nucleus* **5,** 113–118 (2014).

97. Joubert, J., Schutte, C., Irons, D. & Fripp, P. Ubombo and the site of David Bruce's discovery of Trypanosoma brucei. *Transactions of the Royal Society of Tropical Medicine and Hygiene* **87,** 494–495 (1993).

98. Baker, J. The subspecific taxonomy ofTrypanosoma brucei. *Parasite* **2,** 3–12 (1995).

99. Berman, J. J. *Taxonomic Guide to Infectious Diseases: Understanding the Biologic Classes of Pathogenic Organisms* ISBN: 9780124158955 (Academic Press, 2012).

100. Berriman, M. The Genome of the African Trypanosome Trypanosoma brucei. *Science* **309,** 416–422 (2005).

101. Brun, R. & Balmer, O. New developments in human African trypanosomiasis. *Current Opinion in Infectious Diseases* **19,** 415–420 (Oct. 2006).

102. Sinclair, A. N. & de Graffenried, C. L. More than Microtubules: The Structure and Function of the Subpellicular Array in Trypanosomatids. *Trends in Parasitology* **35,** 760–777 (2019).

103. Stephens, N. A., Kieft, R., MacLeod, A. & Hajduk, S. L. Trypanosome resistance to human innate immunity: targeting Achilles' heel. *Trends in Parasitology* **28,** 539–545 (2012).

104. Matthews, K., Sherwin, T. & Gull, K. Mitochondrial genome repositioning during the differentiation of the African trypanosome between life cycle forms is microtubule mediated. *Journal of Cell Science* **108,** 2231–2239 (1995).

105. Robinson, D. R., Sherwin, T, Ploubidou, A, Byard, E. H. & Gull, K. Microtubule polarity and dynamics in the control of organelle positioning, segregation, and cytokinesis in the trypanosome cell cycle. *The Journal of Cell Biology* **128,** 1163–1172 (1995).

106. Westermann, S. & Weber, K. Post-translational modifications regulate microtubule function. *Nature Reviews Molecular Cell Biology* **4,** 938–948 (2003).

107. Janke, C. Tubulin Polyglutamylase Enzymes Are Members of the TTL Domain Protein Family. *Science* **308,** 1758–1762 (2005).

108. Zephyris. *CC BY-SA 3.0* June 2010. `https://commons.wikimedia.org/w/index.php?curid=10769382`.

109. Lane, N. The unseen world: reflections on Leeuwenhoek (1677) 'Concerning little animals'. *Philosophical Transactions of the Royal Society B: Biological Sciences* **370,** 20140344 (2015).

110. Lichtman, J. W. & Conchello, J.-A. Fluorescence microscopy. *Nature Methods* **2,** 910–919 (2005).

111. Jablonski, A. Efficiency of Anti-Stokes Fluorescence in Dyes. *Nature* **131,** 839–840 (1933).

112. Stockert, J. C. *Fluorescence Microscopy In Life Sciences* ISBN: 1681085194 (Bentham Science Publishers, 2017).

113. Shimomura, O., Johnson, F. H. & Saiga, Y. Extraction, Purification and Properties of Aequorin, a Bioluminescent Protein from the Luminous Hydromedusan, Aequorea. *Journal of Cellular and Comparative Physiology* **59,** 223–239 (1962).

114. Tsien, R. Y. The Green Fluorescent Protein. *Annual Review of Biochemistry* **67,** 509–544 (1998).

115. Heim, R., Cubitt, A. B. & Tsien, R. Y. Improved green fluorescence. *Nature* **373,** 663–664 (1995).

116. Cormack, B. P., Valdivia, R. H. & Falkow, S. FACS-optimized mutants of the green fluorescent protein (GFP). *Gene* **173,** 33–38 (1996).

117. Probes®, M. *Qdot® ITK™ Carboxyl Quantum Dots* 1st ed. ThermoFisher scientific (29851 Willow Creek RoadEugene, OR 97402, USA, 2007).

118. Lane, L. A., Smith, A. M., Lian, T. & Nie, S. Compact and Blinking-Suppressed Quantum Dots for Single-Particle Tracking in Live Cells. *The Journal of Physical Chemistry B* **118,** 14140–14147 (2014).

119. Webb, D. J. & Brown, C. M. in *Methods in Molecular Biology* 29–59 (Humana Press, 2012).

120. *Handbook of Biological Confocal Microscopy* ISBN: 038725921X (Springer, 2006).

121. Hynds, R. E., Vladimirou, E. & Janes, S. M. *The secret lives of cancer cell lines* 2018.

122. Moch, M. *et al.* Effects of plectin depletion on keratin network dynamics and organization. *PloS one* **11** (2016).

123. Candeloro, P. *et al.* Nanoparticle microinjection and Raman spectroscopy as tools for nanotoxicology studies. *The Analyst* **136,** 4402 (2011).

124. Zhang, Y. & Yu, L.-C. Single-cell microinjection technology in cell biology. *BioEssays* **30,** 606–610 (2008).

125. Ehrenberg, M. & McGrath, J. L. Binding between particles and proteins in extracts: implications for microrheology and toxicity. *Acta Biomaterialia* **1,** 305–315 (2005).

126. McNeil, P. & Warder, E. Glass beads load macromolecules into living cells. *Journal of Cell Science* **88,** 669–678 (1987).

127. Wakatsuki, T., Kolodney, M. S., Zahalak, G. I. & Elson, E. L. Cell mechanics studied by a reconstituted model tissue. *Biophysical Journal* **79,** 2353–2368 (2000).

128. Lang, F. *et al.* Functional significance of cell volume regulatory mechanisms. *Physiological Reviews* **78,** 247–306 (1998).

129. Brayton, C. F. Dimethyl sulfoxide (DMSO): a review. *The Cornell Veterinarian* **76,** 61–90 (1986).

130. Rotsch, C. & Radmacher, M. Drug-induced changes of cytoskeletal structure and mechanics in fibroblasts: an atomic force microscopy study. *Biophysical Journal* **78,** 520–535 (2000).

131. Wakatsuki, T., Schwab, B., Thompson, N. C. & Elson, E. L. Effects of cytochalasin D and latrunculin B on mechanical properties of cells. *Journal of Cell Science* **114,** 1025–1036 (2001).

132. Yarmola, E. G., Somasundaram, T., Boring, T. A., Spector, I. & Bubb, M. R. Actin-latrunculin A structure and function differential modulation of actin-binding protein function by latrunculin A. *Journal of Biological Chemistry* **275,** 28120–28127 (2000).

133. Mailfert, S, Hamon, Y, Bertaux, N, He, H.-T. & Marguet, D. in *Methods in Cell Biology* 1–22 (Elsevier, 2017).

134. Stadler, L., Speckner, K. & Weiss, M. Diffusion of Exit Sites on the Endoplasmic Reticulum: A Random Walk on a Shivering Backbone. *Biophysical Journal* **115,** 1552–1560 (2018).

135. Stadler, L. & Weiss, M. Non-equilibrium forces drive the anomalous diffusion of telomeres in the nucleus of mammalian cells. *New Journal of Physics* **19,** 113048 (2017).

136. Speckner, K., Stadler, L. & Weiss, M. Anomalous dynamics of the endoplasmic reticulum network. *Physical Review E* **98,** 012406 (2018).

137. Lee, J. C., Field, D. J. & Lee, L. L. Effects of nocodazole on structures of calf brain tubulin. *Biochemistry* **19,** 6209–6215 (1980).

138. Axelsson, M. A. & Warren, G. Rapid, endoplasmic reticulum-independent diffusion of the mitotic Golgi haze. *Molecular Biology of the Cell* **15,** 1843–1852 (2004).

139. McEwen, B. F., Telford, J. N., Handelman, C. T. & Arion, W. J. A critical evaluation of the use of filipin-permeabilized rat hepatocytes to study functions of the endoplasmic reticulum in situ. *Cell Biochemistry and Function: Cellular biochemistry and its modulation by active agents or disease* **5,** 263–272 (1987).

140. King, C., Sengupta, P., Seo, A. Y. & Lippincott-Schwartz, J. ER membranes exhibit phase behavior at sites of organelle contact. *Proceedings of the National Academy of Sciences* (2020).

141. Banfalvi, G. in *Cell Cycle Synchronization* 1–23 (Springer, 2011).

142. Zieve, G. W., Turnbull, D., Mullins, J. M. & McIntosh, J. R. Production of large numbers of mitotic mammalian cells by use of the reversible microtubule inhibitor Nocodazole: Nocodazole accumulated mitotic cells. *Experimental cell research* **126,** 397–405 (1980).

143. Armstrong, J. K., Wenby, R. B., Meiselman, H. J. & Fisher, T. C. The hydrodynamic radii of macromolecules and their effect on red blood cell aggregation. *Biophysical Journal* **87,** 4259–4270 (2004).

144. ThermoFisher. *Product Information Sheet: Hoechst 33342* 1st ed. Nr.62249. Pierce Biotechnology (3747 N. Meridian Road Rockford IL 61105 USA, Jan. 2010).

145. ThermoFisher. *Lipofectamine™ 3000 Reagent Protocol* 1st ed. Publ. No.MAN0009872. Pierce Biotechnology (3747 N. Meridian Road Rockford IL 61105 USA, Feb. 2016).

146. Kim, T. K. & Eberwine, J. H. Mammalian cell transfection: the present and the future. *Analytical and Bioanalytical Chemistry* **397,** 3173–3178 (2010).

147. Glover, D. J., Lipps, H. J. & Jans, D. A. Towards safe, non-viral therapeutic gene expression in humans. *Nature Reviews Genetics* **6,** 299–310 (2005).

148. Ramamoorth, M. & Narvekar, A. Non viral vectors in gene therapy – an overview. *Journal of Clinical and Diagnostic Research* **9,** GE01 (2015).

149. Karasawa, T., Wang, Q., David, L. L. & Steyger, P. S. Calreticulin binds to gentamicin and reduces drug-induced ototoxicity. *Toxicological Sciences* **124,** 378–387 (2011).

150. Chenlo, F, Moreira, R, Pereira, G & Ampudia, A. Viscosities of aqueous solutions of sucrose and sodium chloride of interest in osmotic dehydration processes. *Journal of food Engineering* **54,** 347–352 (2002).

151. Galvao, J. *et al.* Unexpected low-dose toxicity of the universal solvent DMSO. *The FASEB Journal* **28,** 1317–1330 (2014).

152. Cross, G. *Product Information Sheet: Trypanosoma brucei subsp. brucei, Strain Lister 427 29-13 (TetR T7RNAP) (procyclic form)* 1st ed. Nr.42012. BEI Resources (10801 University Boulevard ,Manassas VA 20110-2209, USA, Jan. 2014).

153. Bochud-Allemann, N. & Schneider, A. Mitochondrial substrate level phosphorylation is essential for growth of procyclic Trypanosoma brucei. *Journal of Biological Chemistry* **277,** 32849–32854 (2002).

154. Redmond, S., Vadivelu, J. & Field, M. C. RNAit: an automated web-based tool for the selection of RNAi targets in Trypanosoma brucei. *Molecular and Biochemical Parasitology* **128,** 115–118 (2003).

155. Burkard, G., Fragoso, C. & Roditi, I. Highly efficient stable transformation of bloodstream forms of Trypanosoma brucei. *Molecular and Biochemical Parasitology* **153,** 220–223 (2007).

156. Campagnola, G., Nepal, K., Schroder, B. W., Peersen, O. B. & Krapf, D. Superdiffusive motion of membrane-targeting C2 domains. *Scientific Reports* **5,** 1–10 (2015).

157. Gervasi, M. G. *et al.* The actin cytoskeleton of the mouse sperm flagellum is organized in a helical structure. *Journal of Cell Science* **131** (2018).

158. Manzo, C. & Garcia-Parajo, M. F. A review of progress in single particle tracking: from methods to biophysical insights. *Reports on Progress in Physics* **78,** 124601 (2015).

159. Saxton, M. J. & Jacobson, K. Single-particle tracking: applications to membrane dynamics. *Annual Review of Biophysics and Biomolecular Structure* **26,** 373–399 (1997).

160. Boltyanskiy, R., Merrill, J. W. & Dufresne, E. R. Tracking particles with large displacements using energy minimization. *Soft Matter* **13,** 2201–2206 (2017).

161. Jaqaman, K. *et al.* Robust single-particle tracking in live-cell time-lapse sequences. *Nature methods* **5,** 695 (2008).

162. Tinevez, J.-Y. *et al.* TrackMate: An open and extensible platform for single-particle tracking. *Methods* **115,** 80–90 (2017).

163. Uppaluri, S. *et al.* Impact of microscopic motility on the swimming behavior of parasites: straighter trypanosomes are more directional. *PLoS Computational Biology* **7** (2011).

164. Hochstetter, A. *et al.* Microfluidics-based single cell analysis reveals drug-dependent motility changes in trypanosomes. *Lab on a Chip* **15,** 1961–1968 (2015).

165. Ernst, D. & Köhler, J. How the number of fitting points for the slope of the mean-square displacement influences the experimentally determined particle size distribution from single-particle tracking. *Physical Chemistry Chemical Physics* **15,** 3429–3432 (2013).

166. Backlund, M. P., Joyner, R. & Moerner, W. Chromosomal locus tracking with proper accounting of static and dynamic errors. *Physical Review E* **91,** 062716 (2015).

167. Efron, B. in *Breakthroughs in statistics* 569–593 (Springer, 1992).

168. Efron, B. & Tibshirani, R. J. *An introduction to the bootstrap* (CRC press, 1994).

169. Kepten, E., Bronshtein, I. & Garini, Y. Improved estimation of anomalous diffusion exponents in single-particle tracking experiments. *Physical Review E* **87,** 052713 (2013).

170. Jain, R. & Sebastian, K. L. Diffusion in a crowded, rearranging environment. *The Journal of Physical Chemistry B* **120,** 3988–3992 (2016).

171. Lanoiselée, Y. & Grebenkov, D. S. Unraveling intermittent features in single-particle trajectories by a local convex hull method. *Physical Review E* **96,** 022144 (2017).

172. Grebenkov, D. S., Lanoiselée, Y. & Majumdar, S. N. Mean perimeter and mean area of the convex hull over planar random walks. *Journal of Statistical Mechanics: Theory and Experiment* **2017,** 103203 (2017).

173. Barber, C. B., Dobkin, D. P. & Huhdanpaa, H. The quickhull algorithm for convex hulls. *ACM Transactions on Mathematical Software* **22,** 469–483 (1996).

174. Cao, J. Single molecule tracking of heterogeneous diffusion. *Physical Review E* **63,** 041101 (2001).

175. Wagner, T., Kroll, A., Haramagatti, C. R., Lipinski, H.-G. & Wiemann, M. Classification and segmentation of nanoparticle diffusion trajectories in cellular micro environments. *PloS one* **12** (2017).

176. Rudnick, J. & Gaspari, G. The shapes of random walks. *Science* **237,** 384–389 (1987).

177. Sabri, A., Xu, X., Krapf, D. & Weiss, M. Elucidating the origin of heterogeneous anomalous diffusion in the cytoplasm of mammalian cells. *Physical Review Letters* **125,** 058101 (2020).

178. Weiss, M. Resampling single-particle tracking data eliminates localization errors and reveals proper diffusion anomalies. *Physical Review E* **100,** 042125 (2019).

179. Ernst, D. & Köhler, J. Measuring a diffusion coefficient by single-particle tracking: statistical analysis of experimental mean squared displacement curves. *Physical Chemistry Chemical Physics* **15,** 845–849 (2013).

180. Etienne-Manneville, S. Cytoplasmic intermediate filaments in cell biology. *Annual Review of Cell and Developmental Biology* **34,** 1–28 (2018).

181. Neubauer, R. *et al.* Protein diffusion in a bicontinuous microemulsion: inducing subdiffusion by tuning the water domain size. *Soft Matter* **13,** 1998–2003 (2017).

182. Jentzsch, J. *et al.* Microtubule polyglutamylation is important for regulating cytoskeletal architecture and motility in Trypanosoma brucei. *Journal of Cell Science* **133** (2020).

183. Heddergott, N. *et al.* Trypanosome motion represents an adaptation to the crowded environment of the vertebrate bloodstream. *PLoS Pathogens* **8** (2012).

184. Magde, D., Elson, E. & Webb, W. W. Thermodynamic fluctuations in a reacting system—measurement by fluorescence correlation spectroscopy. *Physical Review Letters* **29,** 705 (1972).

185. Elson, E. L. Fluorescence correlation spectroscopy measures molecular transport in cells. *Traffic* **2,** 789–796 (2001).

186. Lippincott-Schwartz, J., Snapp, E. & Kenworthy, A. Studying protein dynamics in living cells. *Nature Reviews Molecular Cell Biology* **2,** 444–456 (2001).

187. Ries, J. & Schwille, P. Fluorescence correlation spectroscopy. *BioEssays* **34,** 361–368 (2012).

188. Axelrod, D., Koppel, D., Schlessinger, J, Elson, E. & Webb, W. W. Mobility measurement by analysis of fluorescence photobleaching recovery kinetics. *Biophysical Journal* **16,** 1055 (1976).

189. Sprague, B. L. & McNally, J. G. FRAP analysis of binding: proper and fitting. *Trends in Cell Biology* **15,** 84–91 (2005).

190. Soumpasis, D. Theoretical analysis of fluorescence photobleaching recovery experiments. *Biophysical Journal* **41,** 95–97 (1983).

191. Reits, E. A. & Neefjes, J. J. From fixed to FRAP: measuring protein mobility and activity in living cells. *Nature Cell Biology* **3,** E145–E147 (2001).

192. Bugiel, I, König, K & Wabnitz, H. Investigation of cells by fluorescence laser scanning microscopy with subnanosecond time resolution. *Lasers Life Science* **3,** 47–53 (1989).

193. Stiehl, O., Veres, A. & Weiss, M. Monitoring Subcellular Stress Response via a Cell-permeant Rotor Dye. *Journal of Fluorescence* **28,** 605–613 (2018).

194. Förster, T. Zwischenmolekulare Energiewanderung und Fluoreszenz. *Annalen der Physik* **437,** 55–75 (1948).

195. Clegg, R. M. Förster resonance energy transfer – FRET what is it, why do it, and how it's done. *Laboratory Techniques in Biochemistry and Molecular Biology* **33,** 1–57 (2009).

List of Figures

List of Tables

Eidesstattliche Versicherung

Hiermit versichere ich an Eides statt, dass ich die vorliegende Arbeit selbstständig verfasst und keine anderen als die von mir angegebenen Quellen und Hilfsmittel verwendet habe.

Weiterhin erkläre ich, dass ich die Hilfe von gewerblichen Promotionsberatern beziehungsweise -vermittlern oder ähnlichen Dienstleistern weder bisher in Anspruch genommen habe, noch künftig in Anspruch nehmen werde.

Zusätzlich erkläre ich hiermit, dass ich keinerlei frühere Promotionsversuche unternommen habe.

Bayreuth, den .....

.....
Adal Sabri